DEVELOPMENT AND CHARACTERIZATION OF BEAMFORMING ANTENNA SYSTEMS

A DISSERTATION
SUBMITTED TO THE FACULTY OF THE GRADUATE SCHOOL OF
THE UNIVERSITY OF MINNESOTA
BY

CHANJOON LEE

IN PARTIAL FULFILLMENT OF THE REQUIREMENTS
FOR THE DEGREE OF
DOCTOR OF PHILOSOPHY

ADVISOR: RHONDA FRANKLIN
CO-ADVISOR: ROBERT SAINATI

DECEMBER 2017

Acknowledgement

I would like to first thank God for studying Ph.D in University of Minnesota and working with my advisor, Professor Rhonda Franklin. When I was a sophomore, I just had a dream that I would pursue graduate study in the United States but I did not even imagine that I could do. Looking back, God has provided me with everything to meet all my needs. Whenever I encounter difficulties, he has given me ideas, strength, and courage to persistently pursue my study.

I would like to thank Professor Rhonda Franklin for her countless hours of mentoring and guidance throughout my graduate studies. She has not only encouraged me to solve challenging problems but also helped me have a better and deep understanding of my work. She also has been willing to spend hours on discussing any topic with me. She has been warm-hearted and trying to take care of me as family like mom as well as advisor. I would also like to thank Professor Robert Sainati for his numerous hours of mentoring and guidance. He has encouraged me to do research with conscious reasoning as well as intuition. I would also like to thank Prof. Anand Gopinath, Prof. Ramesh Harjani, and Prof. Michael Garwood for their time and effort serving as my committee members.

I would also like to thank MPACT group members: Glenston Miranda, Alex Nelson, Wen Zhou and Yali Zhang for supporting my work. Glenston Miranda helped me a lot in training to familiarize myself with the lab software and equipment.

Lastly, I would like to thank my family for their love and support. My parents, Hyeon-Geun Lee and Mi-Ok Jeong, always have been encouraging and praying for me to

successfully complete my graduate study. My wife, Yujin Oh, and son, Si-Yoon Lee, have provided truly love and support so that I can finish my study.

This dissertation is dedicated to my Lord, God
my loving parents, Hyeon-Geun Lee and Mi-Ok Jeong,
my loving wife and son, Yujin Oh and Si-Yoon Lee,
my loving brother, Chanhyeok Lee

Abstract

This dissertation discusses the development of the beamforming antenna systems as a scaled model for customized RFID systems. In this work, an Fabry-Perot Cavity (FPC) antenna system consisting of a single source and frequency selective surface (FSS) is proposed (chapter 2) and investigated. Since the FPC antenna system removes complicated feedline mechanism in array antenna system, it gains high interest to provide higher directivity/gain. Different FSS unit cell geometry and sources are combined in the FPC system and corresponding effect on the FPC system performance is parametrically and comparatively studied and discussed (chapter 3). The CPW feedline behavior and energy leakage of the FPC system are characterized and technique to mitigate them is presented (chapter 4). Microfluids are integrated into the FPC system to offer either tuning/switching capability of the antenna or near-field beam-splitting with FSS (chapter 5). Lastly, efficiency enhancement of the FPC antenna system using FSS subarray is studied.

Table of Contents

List of Tables

Chapter 3

Chapter 4

Chapter 6

Appendix A

List of Figures

Chapter 1

Chapter 2

Chapter 3

Chapter 4

Chapter 5

Chapter 6

Appendix A

Appendix B

CHAPTER 1

Introduction

1.1. Motivation

Wireless technologies have been widely and commonly used in communication and healthcare systems in that they improve design flexibility and profitability. Radio Frequency Identification (RFID) is a technology that uses electromagnetic waves to wirelessly identify, track and trace objects. This technology has been used for a variety of applications such as healthcare, supply chain management, inventory control, public transportation and animal tracking [1-5]. As global market in healthcare industry has been exceptionally increasing in the last decade, various research groups have explored the use of RFID technologies for healthcare. For example, a wearable RFID epidermal device consisting of a flexible open loop antenna is designed, which enables an easy adhesion on the user's skin and coupled with a graphene oxide-based sensor sensitive to the water vapor [6]. A square millimeter RFID tag booster antenna with an on-chip-coil is designed and fabricated in a low cost 130 nm CMOS process to significantly increase the reading distance of small RFID tags [7]. A simple structure of a folded dipole antenna at 924 MHz is designed to aim at wireless patient monitoring applications and achieve enough gain for more than 10 m range communication [8]. A wirelessly powered implantable electrochemical sensor RFID tag consisting of a winding ferrite antenna provides real-time blood glucose monitoring by remotely powering the system with 13.56

MHz inductive link [9]. Electro-textile RFID loop antennas is designed as wearable sensors to power a state-of-the-art neural recording microsystem by combining stretchable and non-stretchable electro-textiles [10]. Miniaturized helix antennas are integrated with drug reservoirs to function as RFID wireless tag sensors for real-time drug dosage monitoring [11]. Subwavelength electromagnetic bandgap (EBF) isolator is designed as a biomedical repeater device to amplify the attenuated RF signal sent from reader antenna and retransmit it to a miniature implant sensor [12].

The operating frequencies for RFID are classified as four bands: 120 – 150 kHz (Low Frequency), 13.56 MHz (High Frequency), 433 MHz and 902 – 928 MHz (Ultra-High Frequency), and 2450 – 5800 MHz (Microwave). The RFID systems consist of reader and tag. A reader transmits RF signal to a tag attached to an object to be identified and communicates with the tag. In wireless power transfer systems like RFID, the parameters such as transmit frequency, power received by tag, distance between reader and tag, and tag size need to be carefully considered to maximize energy transmission and reception as shown in Appendix A.

The federal communication commission (FCC) has restricted power transmission depending on operating frequency and distance for safety. The electric field strength vs. distance for different frequencies is shown in Fig. 1.1. It indicates that 60 GHz is the most conducive for power transmission. Also, since the wavelength (= 5 mm) of 60 GHz is much shorter than that of the conventional RFID operating bands, 60 GHz RFID systems can provide much smaller and more compact form of wireless monitoring.

Based on discussions above, customized RFID systems at 60 GHz can be possible

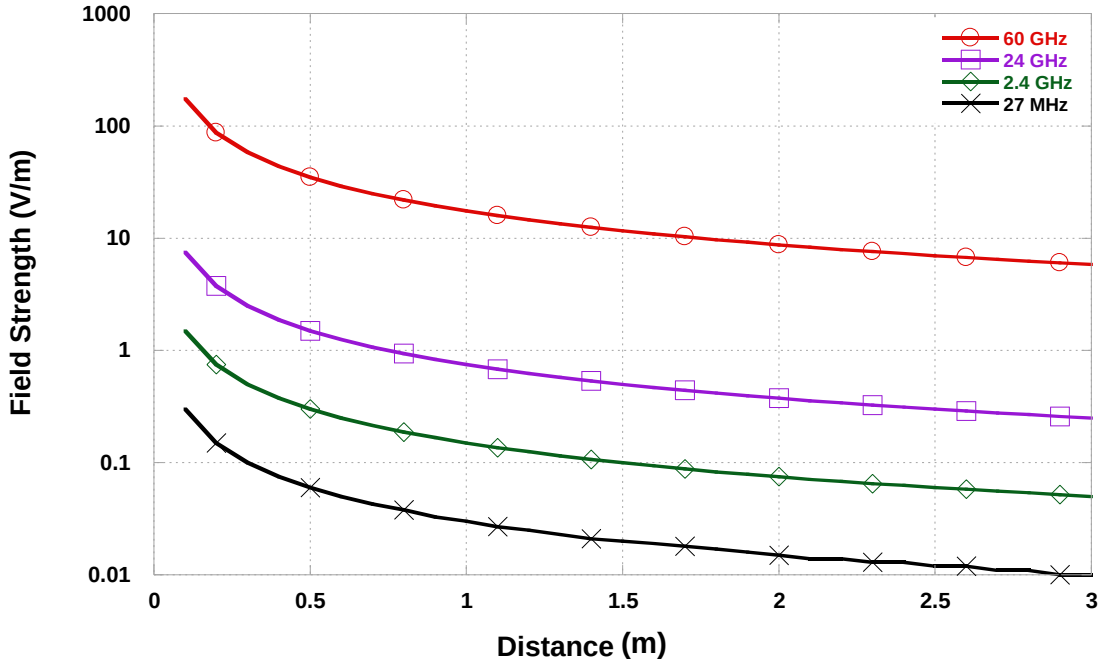

Fig. 1.1. Electric field strength (V/m) vs. distance (m)

solutions for blood monitoring system as emerging technology. Since a tag is attached to a small size of blood bag in the system, a highly directive antenna is required to transmit/receive maximum power under low energy conditions. In this work, the scaled model of beamforming antenna systems is developed and investigated to maximize transmit/receive power. An Fabry-Perot Cavity (FPC) antenna as beamforming system is studied and analyzed to improve performance. Further, to provide design flexibility and reconfigurability in beamforming antenna systems, a microfluidic approach has been investigated and discussed.

1.2. Thesis overview

Chapter 2 discusses an Fabry-Perot Cavity (FPC) antenna system as a scaled model of beamforming antenna systems. The FPC antenna system combines a single source with frequency selective surface (FSS) to enhance the directivity/gain of the antenna.

Based on the principle of the FPC antenna system, chapter 3 details parametric and comparative study of the FPC system. Different FSS unit cell geometry is evaluated to compare the leakage and FSS geometry/source effect on near- and far-field performance is discussed.

Chapter 4 discusses challenges existing in FPC antenna system and techniques to resolve them. A coplanar waveguide (CPW) feedline effect on the FPC antenna system is studied and a technique to alleviate feedline behavior is discussed. Also, leakage-controlled FPC antenna systems are characterized to prevent lateral and back radiation.

Chapter 5 investigates reconfigurable FPC antenna systems using microfluids. Introduction of microfluidic channel achieves simultaneous tuning and switching of the FPC system. Also, a novel technique to split the near-field beam using the augmented FSS or microfluidic FSS design is discussed.

Chapter 6 studies high efficiency FPC antenna system using FSS subarrays. High efficiency and compact FSS subarray is developed to improve the aperture efficiency of the FPC system.

Lastly, chapter 7 summarizes work discussed in this dissertation and proposes future work.

CHAPTER 2

Scaled Model of Beamforming Antenna Systems

2.1. Introduction

Beamforming antenna systems are attractive for spatial selectivity and high directivity and are used for numerous applications such as radar, wireless communication, and biomedicine [13]. Array antenna systems create higher directivity by exciting multiple radiating elements and combining multiple beams in a constructive way towards desired direction. These array antenna systems are appropriate for developing RFID blood monitoring systems discussed in the previous chapter. They suffer, however, from losses and interference due to complex feedline network thus leading to performance degradation. Fabry-Perot Cavity (FPC) antenna systems, which are leaky wave antennas, replace multi-radiating elements [14-20]. It also reduces complexity by a single source and removes the complicated feedline network in array systems by using a single source and frequency selective surface (FSS) or partially reflective surface (PRS). Additional antenna performance metrics are controlled in the FPC antenna system. For example, to enhance efficiency, adding a PEC shield at a distance of $\lambda_o/4$ below the ground plane suppresses the side and back lobe [21] or highly reflective compact metamaterial surface is used [22]. To enhance bandwidth, two-layer periodic structures [23] or successively tapered meandering loops [24] are used. Also, multilayer partially reflective surfaces consisting of metallic patches are used [25]. To improve gain, sparse

arrays are used under a partially reflective superstrate made of high permittivity layers [26] or laminated conductors to form conducting patches are used [27].

Based on the discussions above, the work presented herein studies the FPC antenna systems consisting of microstrip or coplanar waveguide (CPW)-fed antenna and different FSS designs to characterize, improve antenna performance and provide novel techniques using microfluids as a means of design flexibility and reconfigurability.

To best estimate antenna performance in the real world, the antenna measurement should be performed in a place that closely imitates the antenna's real world operating environment [28]. However, antenna measurement system for radiation patterns can be performed up to 18 GHz in our research lab environment. Therefore, the intentional antenna design will be investigated at a scaled model frequency of 12 GHz. Once the desired performance is achieved, these designs can be scaled to 60 GHz by reducing the size by a factor of 5. In this chapter, the basic of FPC antenna systems will be discussed. Based on that, the design approach for scaled model of FPC antenna systems will be presented and the results will be followed.

2.2. Basic of Fabry-Perot Cavity (FPC) Antenna Systems

FPC antenna systems consist of a single source and FSS. A patch, slot or waveguide have been used as the source [29-31]. An FSS is a thin and repetitive surface designed to reflect, transmit or absorb electromagnetic fields based at the desired operating frequency of the field [32]. The first concept of an FSS, referred to as Partially Reflecting Sheet

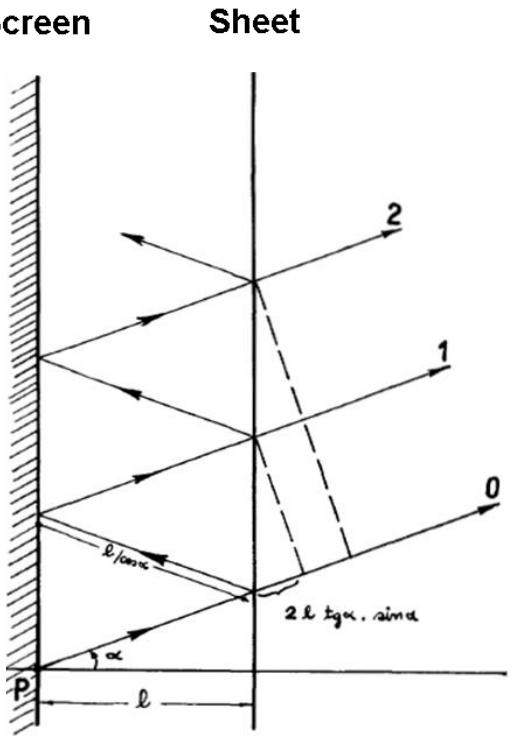

Fig. 2.1. Multiple reflections between screen and sheet

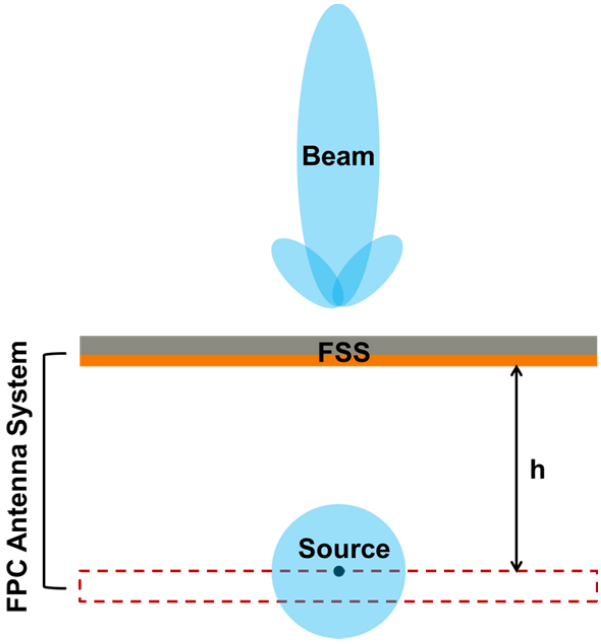

Fig. 2.2. Beamforming of Fabry-Perot Cavity (FPC) antenna system

Arrays, was introduced in [33]. The conducting screen is placed behind the antenna and partially reflecting sheet is located at a distance “l” from the screen as shown in Fig. 2.1 [33]. Multiple reflections are introduced inside the cavity formed between screen and sheet. The partial rays (0 to 2), with decreasing amplitude, are projected through the sheet and have equal phase in normal direction. As a result, the rays are combined to create a highly directive beam in the FPC system as shown in Fig. 2.2. For this purpose, the separation between screen and sheet (h) in Fig. 2.2 must be chosen to provide equal phase of the partial rays through the sheet.

2.3. Design Approach

All antenna and FSS designs are modeled and simulated using ANSYS HFSS (High Frequency Structural Simulator) [34], a software that is widely used in the industry and the academy that offers state-of-the-art technologies to solve a wide range of microwave, RF and high-speed digital applications. Since the FPC antenna system is a complex and high-frequency structure, the HFSS is a good CAD tool to simulate the three-dimensional structure.

2.3.1. Source Design

The slot antenna used as a source in the FPC system is shown in Fig. 2.3. The slot antenna is designed to operate at 12 GHz and inductively fed by a coplanar waveguide (CPW) line. The slot length and width are 22.88 mm and 1.88 mm, respectively. The CPW signal line width and gap spacing of the feedline is 4.83 mm and 0.2 mm, respecti-

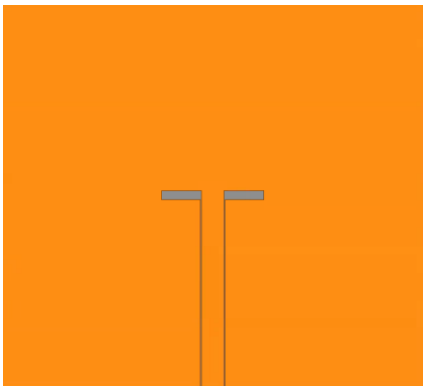

Fig. 2.3. CPW-fed slot antenna

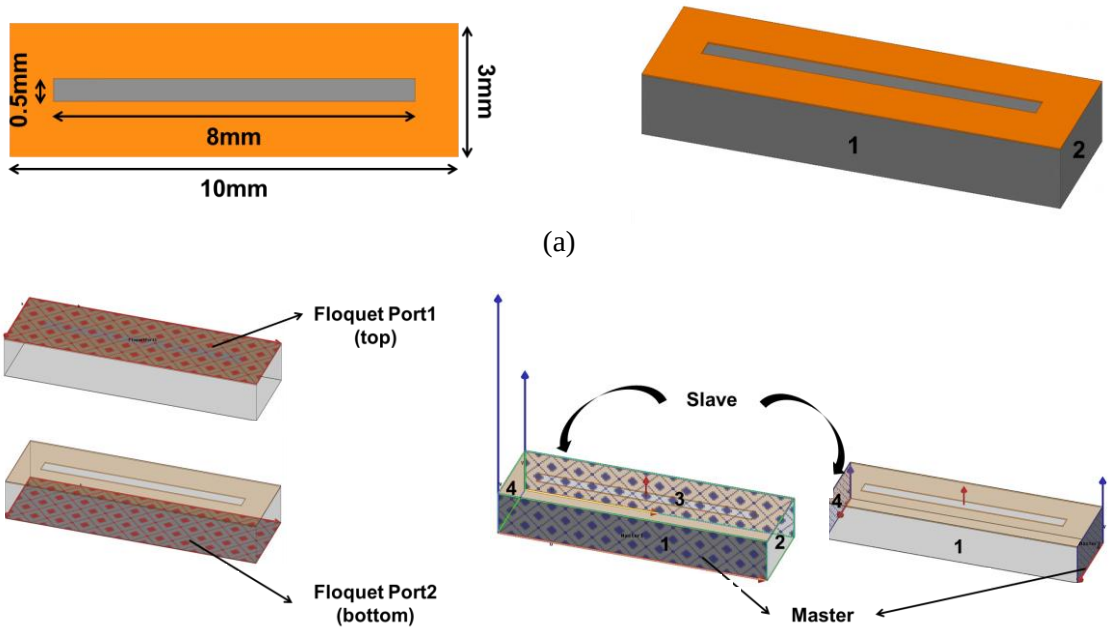

(a)

(b) (c)

Fig. 2.4. FSS rectangular unit cell: (a) top (left) and trimetric (right) view (b) Floquet port excitation (c) Master and Slave boundary assignment

vely. The antenna is printed on Rogers Duroid5880 (ε_r = 2.2, substrate height = 1.57 mm, metal thickness = 35 μm, tan δ = 0.0009).

2.3.2. FSS Design

The rectangular unit cell used in the FSS structure is shown in Fig. 2.4 and is printed on Rogers Duroid5880. The reflection coefficient is the most critical parameter for the unit cell design and it controls leakage through FSS that affects gain of the FPC antenna system. A parametric analysis is performed in HFSS to determine the dimension of the unit cell. A unit cell of 10 mm by 3 mm with a rectangular aperture of 8 mm by 0.5 mm in the center is chosen to provide the reflection coefficient of -0.28 dB at 12 GHz. The radiation boundary encloses the unit cell and is located 2 μm away from the surrounding surfaces (1-4) and 16.05 μm from the top and bottom surfaces of the cell, respectively. To excite the unit cell, the Floquet port in HFSS is used and assigned to the top and bottom surface of the radiation boundary. The Floquet modes are employed exclusively for periodic planar structure and assume the planar structures are idealized as infinitely large. Two pairs of Master and Slave boundaries are assigned to the four surfaces (1 to 4) of the radiation boundary as shown in Fig. 2.4. Master and Slave boundaries are enabled to model planes of periodicity where the electric field on one surface matches the electric field on another to within a phase difference [35]. Using de-embedding function, the reference planes (RP) are shifted to the aperture surface of the unit cell.

Based on the unit cell design, the dimension of the FSS structure needs to be determined. HFSS simulation provides the response of the infinite array. Considering simulation-running time and actual design, however, it is more practical to design and simulate finite FSS structure. Simulations are performed numerically and 9 by 27 unit

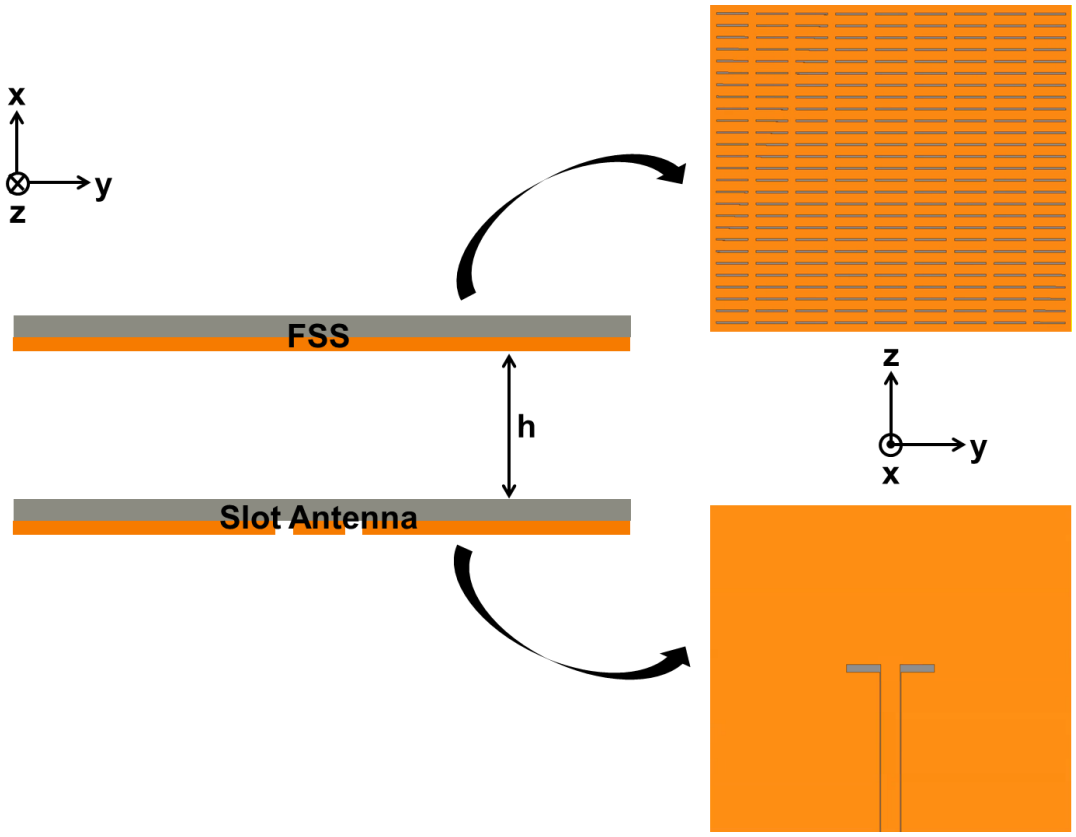

Fig. 2.5. Side view of FPC antenna system with CPW-fed slot antenna and FSS

cells are selected to be the dimension of the FSS array. Details for the simulation setup of an FSS unit cell design are described in Appendix B.

2.3.3. FPC Antenna System

The FPC antenna system with the combined CPW feedline, slot antenna and FSS, discussed in the previous sections 2.3.1 and 2.3.2, is shown in Fig. 2.5. The metal surface of slot antenna points downward and the air cavity is formed between the FSS and slot antenna. The cavity height (h) is the critical parameter to make phase of the partial rays through the FSS equal, resulting in a highly directive beam. The transmission line model

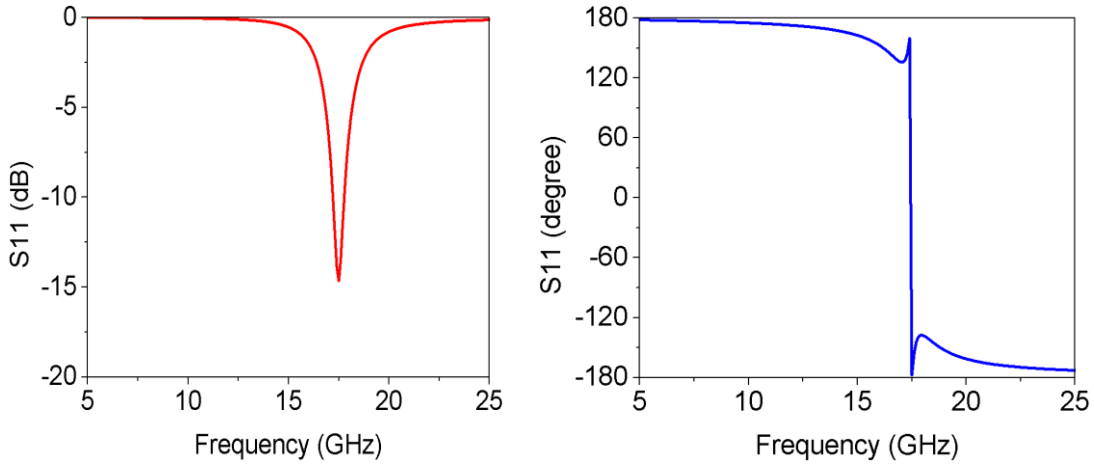

(a) (b)

Fig. 2.6. Reflection response (S11) of FSS rectangular unit cell: (a) magnitude (dB) (b) phase (degree)

of the FPC system and transverse resonance condition in [36] are used to find the cavity height of 10.81 mm. The radiation boundary encloses the whole structure and wave port is used to excite the slot antenna and thus illuminate the FSS in the FPC system.

2.4. Results

The reflection response (S11) of the unit cell is shown in Fig. 2.6. The magnitude is -14.65 dB and the phase changes abruptly at the resonant frequency of 17.5 GHz. The cell is electrically invisible at resonance while most of energy does not pass through the cell at other frequencies. The magnitude curve has very narrow bandwidth and can be considered high Q bandpass filter. The magnitude of the S11 is -0.082 dB and the phase is 172.74˚ at the FPC antenna system design frequency of 12 GHz. As the FSS is more reflective, it leads to more energy inside the cavity, generating more partial rays through

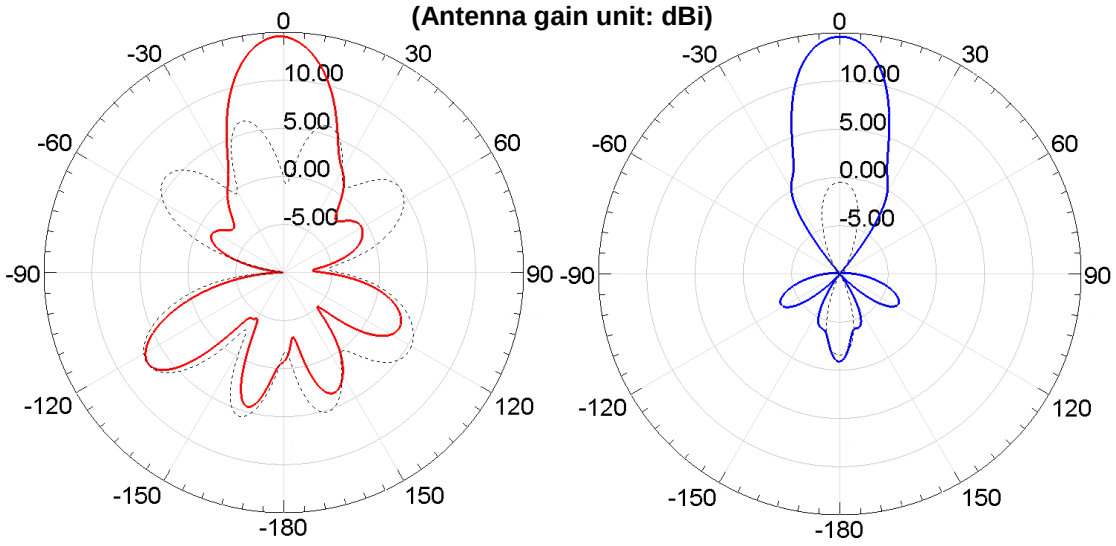

Fig. 2.7. Simulated far-field radiation patterns of slot antenna only (dashed) and FPC system (solid): (a) E-plane (b) H-plane

FSS. Those in-phase rays are combined to create higher gain in the far-field region.

The simulated far-field radiation patterns for slot antenna only and FPC system are shown in Fig. 2.7. The E-plane is defined as xz-plane and H-plane as xy-plane as shown in Fig. 2.5. For slot antenna, the peak gain in E-plane is 6.34 dBi and in H-plane is -0.47 dBi at 12 GHz. When the slot antenna is combined with FSS, the beamforming is achieved as shown in Fig. 2.2. The peak gain in E- and H-plane is 13.03 dBi at 11.2 GHz. While the design was 12 GHz, the optimum patterns are observed at 11.2 GHz. As expected, the rays through FSS with equal phase make a contribution to creating directive beam above FSS. Due to inherent nature of bi-directional source radiation and open air-cavity, the side and back lobes are observed. These lobes can be suppressed by using metallic sidewalls and reflector enclosure and will be discussed in the subsequent chapter.

2.5. Summary

In this chapter, a scaled model of beamforming antenna systems at 12 GHz is introduced and developed to provide feasible solutions for customized RFID systems at 60 GHz discussed in the previous chapter. It demonstrates that an Fabry-Perot Cavity (FPC) antenna system consisting of a single source antenna and FSS array removes complex feedline network present in array antenna systems and creates a sharper and directive pencil beam, which increases ~ 7 dB in E-plane and ~ 13 dB in H-plane compared to a single source antenna.

CHAPTER 3

Parametric and Comparative Study of FPC Antenna Systems

3.1. Introduction

An FPC antenna system replaces multi-radiating elements and complex feedline network with a single source and FSS. FPC systems performance depends on the radiation of source and energy leakage through FSS, which is determined by FSS unit cell geometry. In this chapter, the effect of an FSS unit cell geometry on leakage is investigated. Based on that, the performance of FPC antenna system with rectangular FSS is evaluated by parametric study. Also, the role of FSS design with a given source antenna type or vice versa is studied in beamforming capability. Two source antenna types – slot or patch – are considered with FSS designs of either a rectangular or circular aperture.

3.2. Parametric Study of FSS Unit Cell Geometry and Leakage

3.2.1. Design

The beamforming of FPC antenna system is controlled by energy leakage through FSS and cavity height. The leakage is dependent on FSS unit cell geometry. Various unit cell geometries have been designed and discussed [37-39]; however, lacking is an understanding of correlation between unit cell geometry and leakage. In this section, the

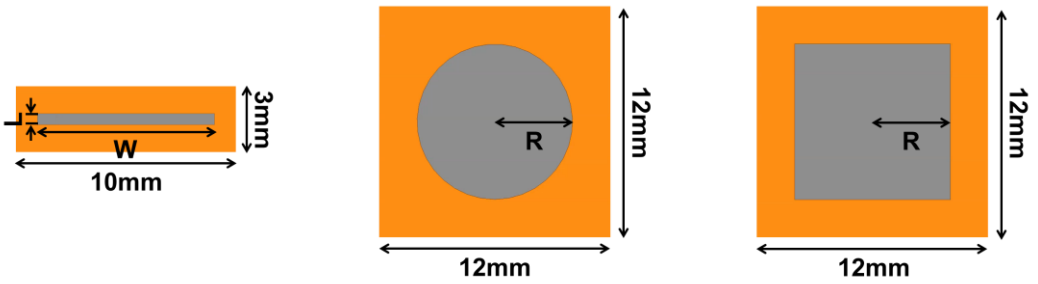

(a) (b) (c)

Fig. 3.1. FSS unit cells: (a) rectangle (b) circle (c) square

effect of FSS unit cell geometry on leakage is studied (cavity height effect will be discussed in the section 3.3). Since each unit cell has a self-resonant frequency ($f_{self\text{-}res}$), design frequency (f_{design}) is chosen away from $f_{self\text{-}res}$. The farther the f_{design} gets from the $f_{self\text{-}res}$, the higher reflection occurs at the f_{design}.

Three types of an FSS unit cell are proposed in this study; rectangle, circle and square as shown in Fig. 3.1. Each unit cell is defined based on the aperture type of the unit cell and designed to operate at the design frequency, f_{design} of 12 GHz. A rectangular unit cell of 10 mm by 3 mm has a rectangular aperture of 'W' by 'L' as shown in Fig. 3.1(a). A circular unit cell of 12 mm by 12 mm has a circular aperture of radius 'R' as shown in Fig. 3.1(b) and a square unit cell of 12 mm by 12 mm has a square aperture of side length of '2R' as shown in Fig. 3.1(c). All boundary conditions are specified as mentioned in section 2.3.2. All apertures are centered in each unit cell.

In this unit cell study, three parameters are considered: (1) aperture dimension of unit cell (2) aperture ratio, defined as ratio of aperture area to total unit cell area. (3) self-resonant frequency ($f_{self\text{-}res}$). The results will be discussed in the following section.

3.2.2. Results

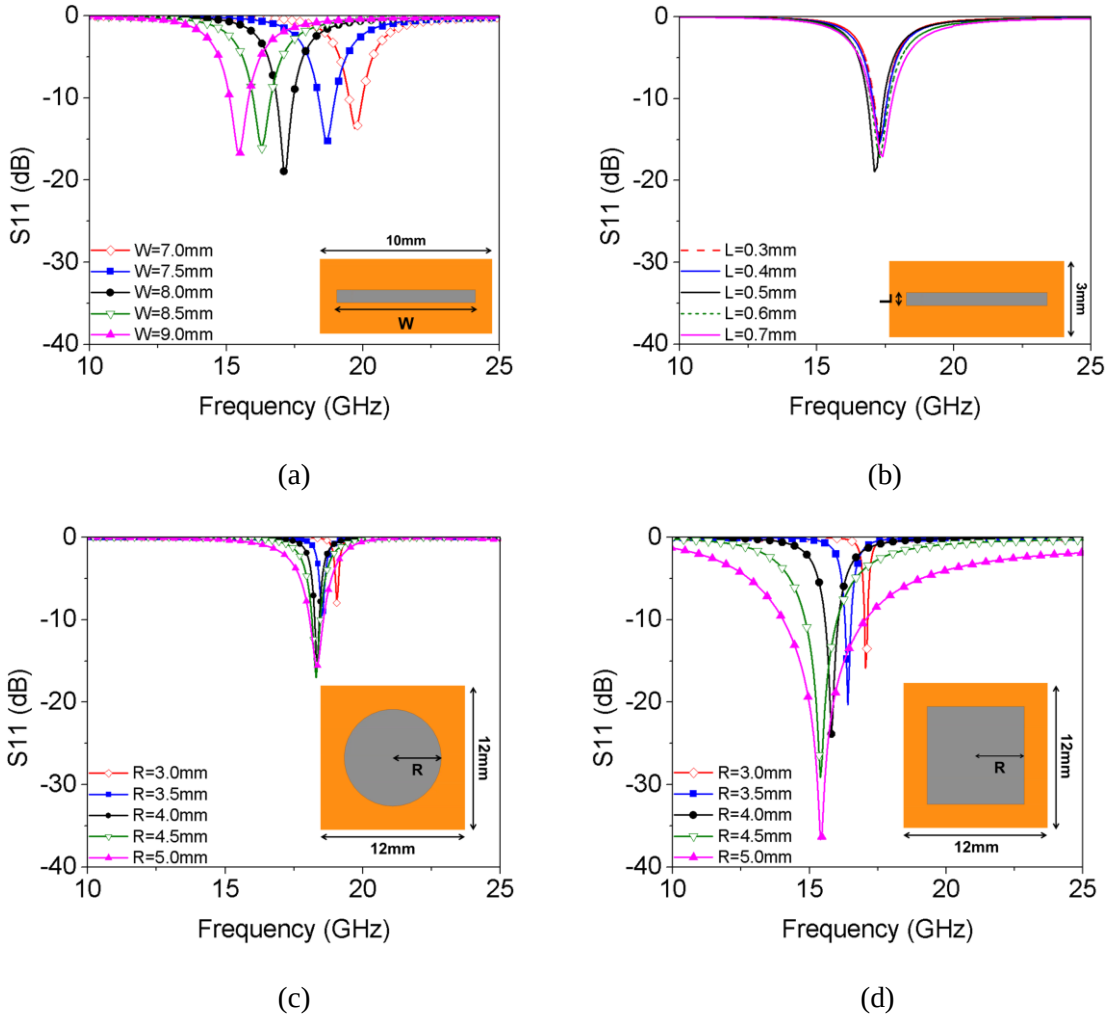

Fig. 3.2. S11 (dB) vs. frequency of FSS unit cells (letter in parentheses is a parameter): (a) rectangle (L) (b) rectangle (W) (c) circle (R) (d) square (R)

Table 3.1. Rectangular unit cell with variation of 'W'

	Aperture ratio (%)	Self-resonant frequency (GHz)	S11 (dB) @ f_{design}
7.0	11.67	19.7	-0.028
7.5	12.5	18.7	-0.055
8.0	13.33	17.1	-0.082
8.5	14.17	16.3	-0.185
9.0	15	15.5	-0.315

Table 3.2. Rectangular unit cell with variation of 'L'

	Aperture ratio (%)	Self-resonant frequency (GHz)	S11 (dB) @ f_{design}
0.3	8	17.3	-0.067
0.4	10.67	17.3	-0.081
0.5	13.33	17.1	-0.082
0.6	16	17.3	-0.109
0.7	18.67	17.4	-0.132

Table 3.3. Circular unit cell with variation of 'R'

	Aperture ratio (%)	Self-resonant frequency (GHz)	S11 (dB) @ f_{design}
3.0	19.63	19.05	-0.0005
3.5	26.72	18.5	-0.0018
4.0	34.91	18.35	-0.0061
4.5	44.18	18.3	-0.0205
5.0	55.54	18.3	-0.0594

Table 3.4. Square unit cell with variation of 'R'

	Aperture ratio (%)	Self-resonant frequency (GHz)	S11 (dB) @ f_{design}
3.0	6.25	17.05	-0.0039
3.5	8.51	16.4	-0.0195
4.0	11.11	15.8	-0.1126
4.5	14.06	15.4	-0.7322
5.0	17.36	15.4	-3.3550

The plot of reflection response (S11) versus frequency for each unit cell is shown in Fig. 3.2 and the results are summarized in Table 3.1 to Table 3.4. For rectangular unit cell, the two parameters, 'W' and 'L' are evaluated. The aperture width 'W' is varied by increments ± 0.5 mm (6.25 %) relative to the baseline (8.0 mm) as shown in Fig. 3.2(a).

At baseline, the rectangular unit cell S11 value is -18.9 dB and observed to have a self-resonance frequency ($f_{self\text{-}res}$) of 17.1 GHz. The S11 at $f_{self\text{-}res}$ is between -14 and -19 dB. As the width decreases from 9 mm to 7 mm, the aperture ratio decreases from 15 % to 11.67 %, causing $f_{self\text{-}res}$ to increase from 15.5 GHz to 19.7 GHz. At the design frequency, when the self-resonant frequency increases, the S11 value increases (i.e. -0.315 dB to -0.028 dB). It indicates that small variation of aperture ratio (~ 3 %) for aperture width 'W' increases the S11 value at the f_{design} by ~ an order of 10.

For the same structure, when the aperture length 'L' is varied by increments ±0.1 mm (20 %) relative to the baseline (0.5 mm), the $f_{self\text{-}res}$ and corresponding S11 are nearly the same as shown in Fig. 3.2(b). Also, the S11 at the f_{design} is between -0.067 and -0.132 dB. As the length decreases from 0.7 mm to 0.3 mm, the aperture ratio reduces from 18.67 % to 8 %. It reveals variation of aperture ratio (~ 10 %) for aperture length 'L' has a negligible impact on the reflection response.

For circular unit cell, the radius 'R' is varied by increments ±0.5 mm (12.5 %) relative to the baseline (4 mm). As the radius decreases from 5 mm to 3 mm, the aperture ratio varies from 55.54 % to 19.63 %. The self-resonant frequency, $f_{self\text{-}res}$ is nearly the same and the S11 range is -17 dB to -8 dB. At the f_{design} of 12 GHz, the S11 increases to from -0.0594 dB to -0.0005 dB. It demonstrates that the large variation of aperture ratio (~ 35 %) increases the S11 (dB) at the f_{design} by an order of ~ 10^2. It demonstrates that large aperture ratio for the radius 'R' (~ 35 %) affects the reflection response slightly.

For square unit cell, the aperture width 'R' is varied by increments ±0.5 mm (12.5 %) relative to the baseline (4 mm). As the width decreases from 5 mm to 3 mm, the

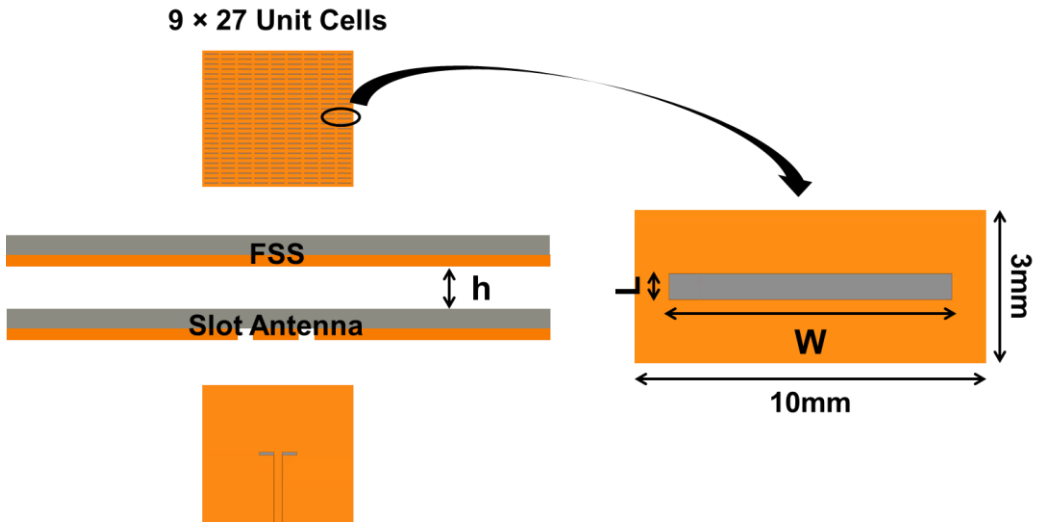

Fig. 3.3. FPC antenna system with rectangular unit cells. Three parameters are shown: cavity height (h), unit cell length (L) and unit cell width (W)

aperture ratio decreases from 17.36 % to 6.25 % creating an $f_{self\text{-}res}$ that increases from 15.4 to 17.05 GHz. The corresponding S11, however, also increases significantly from -36.68 to -15.84 dB. At the design frequency, f_{design}, S11 increases from -3.3550 to -0.0039 dB by an order of ~ 10^3. Thus, small variation of square aperture ratio (~ 10 %) has a significant impact on S11 at the f_{design}.

3.3. Parametric Study of Near- and Far-Field Performance of FPC Antenna Systems

3.3.1. Design

In this section, an FPC antenna system with rectangular FSS unit cells discussed in section 2.3 and 3.2 is presented for parametric study [13]. A CPW-fed slot antenna is

used as a source to excite the FPC system. Details about this FPC antenna system were discussed in the section 2.3. Since the far-field performance of the antenna systems is closely associated with near-field behavior, three main parameters are considered for this study: (1) cavity height (h) (2) aperture width (W) (3) aperture length (L). The baseline for parametric study is the cavity height (h) of 10.81 mm, aperture width (W) of 8 mm and aperture length (L) of 0.5 mm. In aperture array antenna theory, if the aperture array is uniformly illuminated, the peak gain will increase and beamwidth will decrease, like shaper pencil beams, while side lobes increase. When the array illumination becomes more tapered, the peak gain decreases, beamwidth increases and side lobes reduce. Near-field and far-field performance will be discussed in the following section.

3.3.2. Results

The near-field distribution of each variation to the FPC antenna system design at 11.2 GHz is shown in Fig. 3.4 to Fig. 3.6. The feedline is located along the S-N line and the slot antenna is located along the W-E line. The 2D near-field distribution at 5 mm above FSS is shown on the left side and 1D near-field along the W-E line is shown on the right side in each figure. The E- and H-plane cut are defined as the direction along the S-N line and W-E line, respectively.

First, cavity height (h) is parametrized by increments ±5 % of the baseline height (10.81 mm) as shown in Fig. 3.4. For the baseline, electric field with a small tail above the feedline is focused around the center of the slot antenna and the maximum field intensity is 601 V/m. As the height decreases to 10.27 mm, the distribution becomes

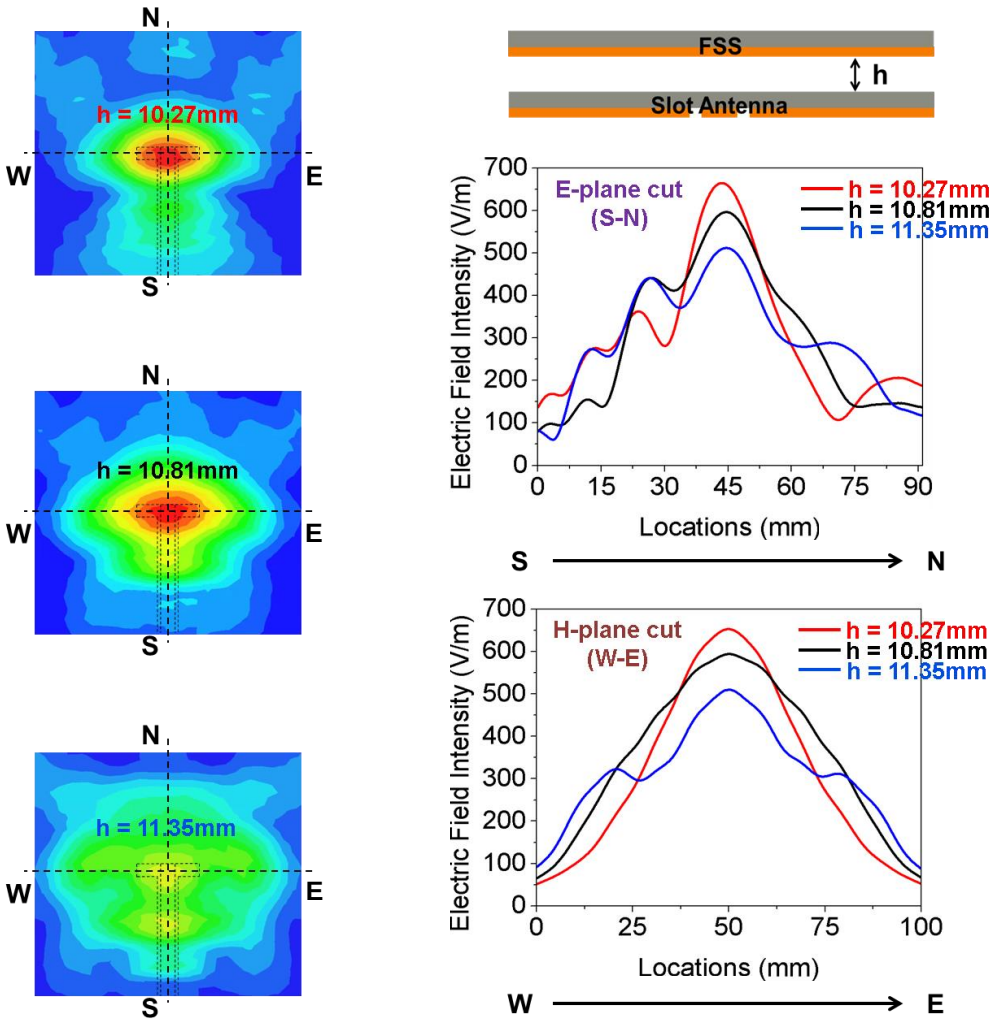

Fig. 3.4. Near-field distributions for cavity height (h) variation with FSS unit cells of W = 8 mm and L = 0.5 mm

more tapered and a focused beam around the center is observed and the peak intensity increases to 664 V/m. As the height increases to 11.35 mm, however, the field spreads out more uniformly due to lower leakage through the FSS and the peak intensity decreases to 512 V/m.

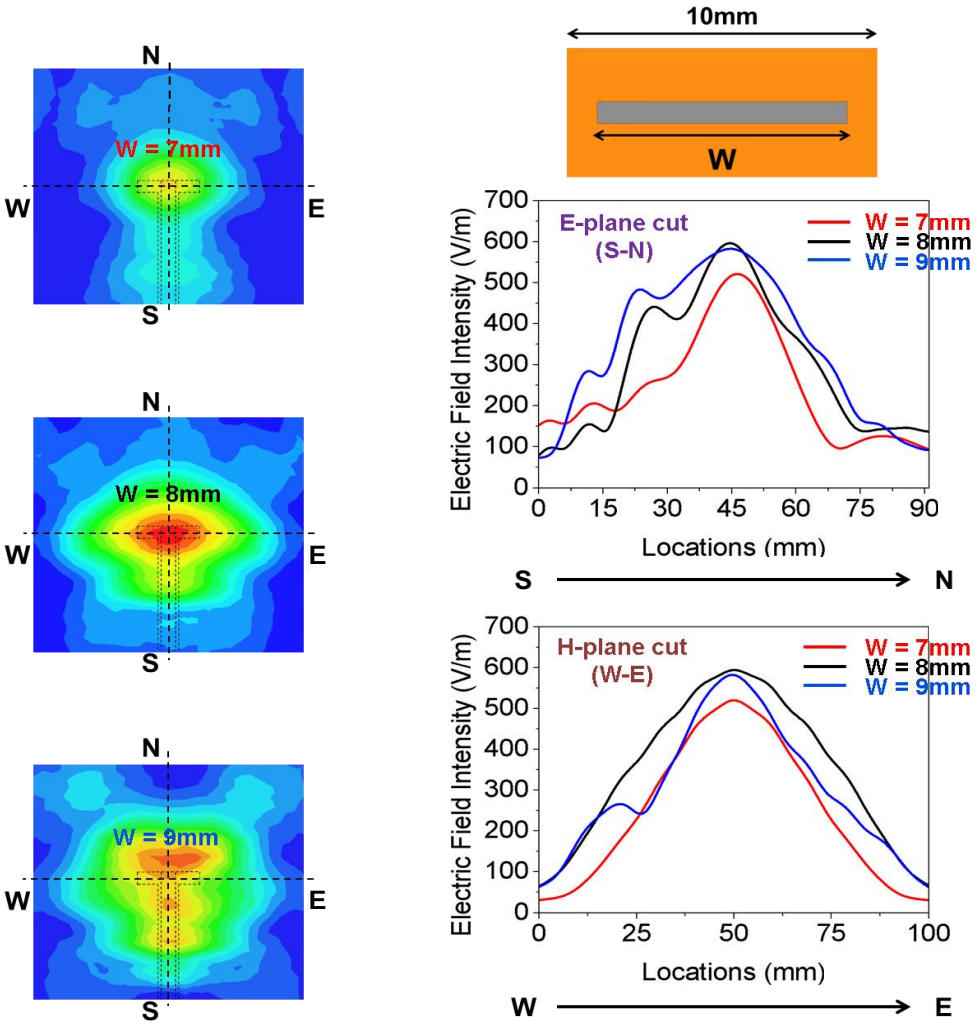

Fig. 3.5. Near-field distributions for FSS unit cell width (W) variation at cavity height (h) = 10.81 mm and FSS unit cell length (L) = 0.5 mm

Second, the aperture width (W) is parametrized by increments ±12.5 % (1 mm) of the baseline (8 mm) as shown in Fig. 3.5. As the width decreases to 7 mm, the electric field distribution in H-plane cut becomes more tapered and the peak intensity decreases to 520 V/m. As the width increases to 9 mm, the location of peak intensity is shifted toward 'N' away from the center and field spreads out more along the S-N line and the peak intensity decreases slightly to 582 V/m compared to the baseline.

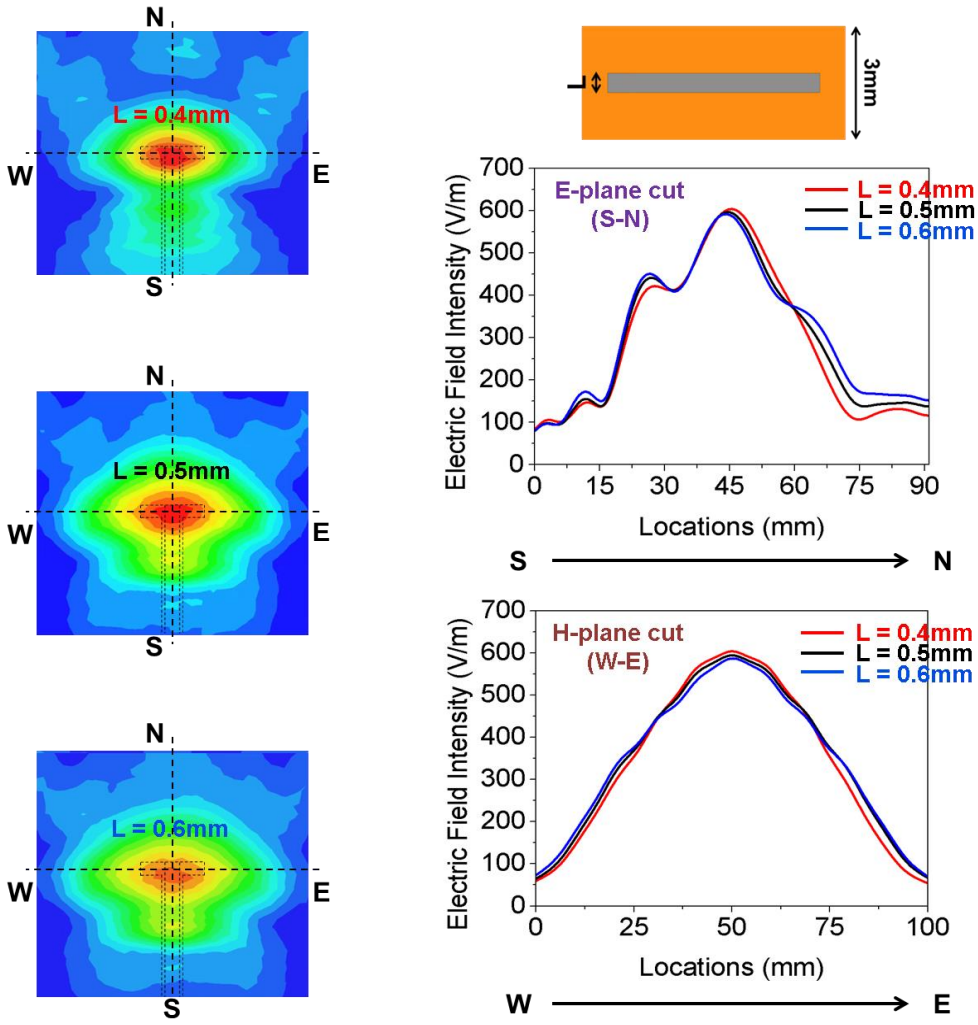

Fig. 3.6. Near-field distributions for FSS unit cell length (L) variation at cavity height (h) = 10.81 mm and FSS unit cell width (W) = 8 mm

Lastly, the aperture length (L) is parametrized by increments ±20 % (0.1 mm) from the baseline (0.5 mm) as shown in Fig. 3.6. The electric field shape and intensity are nearly the same in all cases. It verifies that varying the aperture length up to 20 % has a negligible impact on the reflection response of the unit cell and thus near-field behavior that results from energy leakage through FSS is also similar.

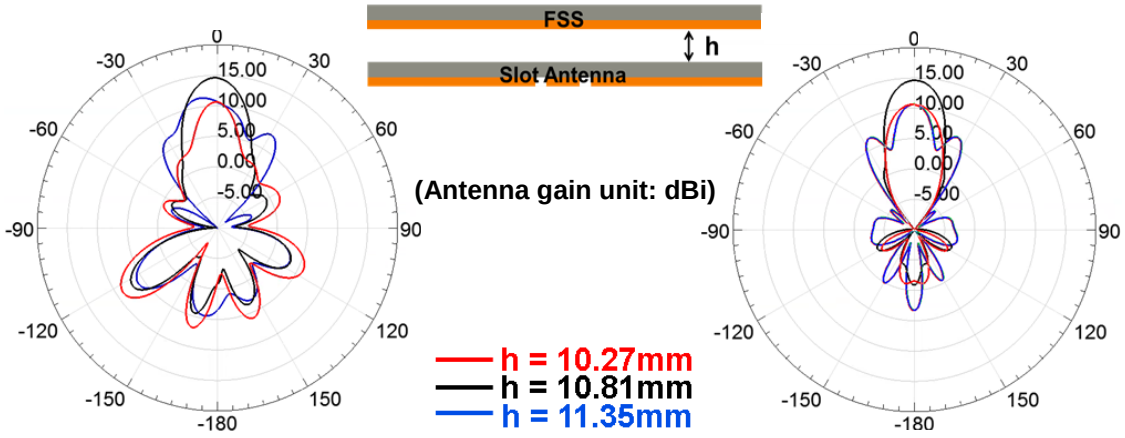

(a) E-plane (b) H-plane

Fig. 3.7. Far-field radiation patterns for cavity height (h) variation with FSS unit cells of L = 0.5 mm and W = 8 mm

The far-field radiation patterns are shown in Fig. 3.7 to Fig. 3.9. For cavity height variation shown in Fig. 3.7, the peak gain for the smaller height (h = 10.27 mm) is 10.66 dBi, for the baseline (h = 10.81 mm) is 14.61 dBi and for the taller height (h = 11.35 mm) is 10.7 dBi. The H-plane beamwidths for the smaller and baseline cavity height are 26º and 22º, respectively. It verifies that the near-field of the smaller height gets more tapered as shown in Fig. 3.4. This results in a reduction in peak gain and increase in beamwidth. For the taller cavity height, the H-plane side lobe gets larger due to a less tapered near-field distribution compared to the baseline. Another factor is a probable change in the phase distribution across FSS array. The cavity height for the baseline is optimized to produce a uniform phase and thus to achieve higher gain. As the cavity height deviates from the baseline, an "even phase error" may occur. Even phase error is the deviation in phase from the desired values varies symmetrically about the array or aperture center.

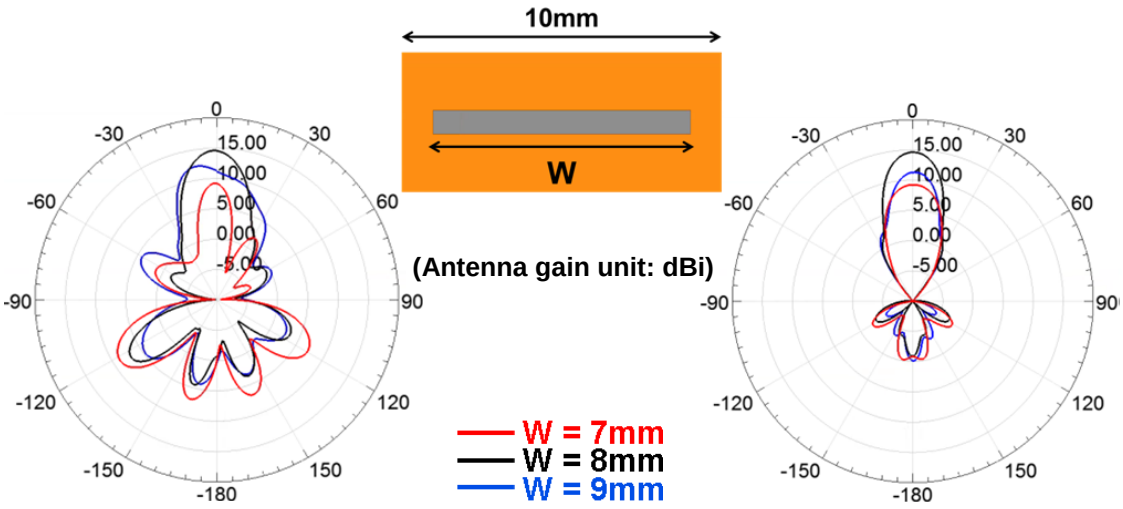

(a) E-plane (b) H-plane

Fig. 3.8. Far-field radiation patterns for FSS unit cell width (W) variation at cavity height (h) = 10.81 mm and FSS unit cell length (L) = 0.5 mm

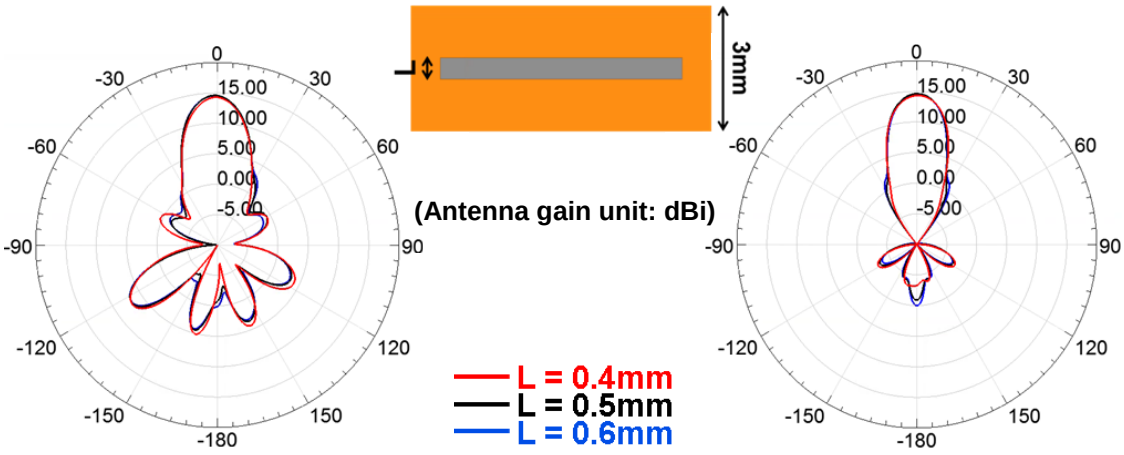

(a) E-plane (b) H-plane

Fig. 3.9. Far-field radiation patterns for FSS unit cell length (L) variation at cavity height (h) = 10.81 mm and FSS unit cell width (W) = 8 mm

For the aperture width (W) variation shown in Fig. 3.8, the peak gain for the narrower apertures (W = 7 mm) is 9.23 dBi, for the baseline (W = 8 mm) is 14.61 dBi and for the wider apertures (W = 9 mm) is 11.28 dBi. The H-plane beamwidths for the

narrower and baseline are 29º and 22º, respectively. It is consistent with the fact that the near-field of the narrower aperture width is more tapered compared to the baseline. An even phase error across the FSS could results in lower gain probably due to the change in FSS reflection coefficient magnitude and phase.

For the aperture length (L) variation shown in Fig. 3.9, all patterns have the identical peak gain and similar level of side and back lobe. It proves that the near-field illumination is similar for each modification and thus far-field pattern is also consistent. Therefore, if energy leakage through FSS unit cell is not sensitive to the aperture length (L), corresponding near- and far-field performance do not change.

3.4. Experimental Characterization - Study of FSS Geometry Effect in FPC Antenna Systems

3.4.1. Design

In this study, two FSS unit cell geometries are considered in FPC antenna systems: (1) rectangular (R) aperture and (2) circular (C) aperture discussed in section 3.2 [40]. The FSS array is optimized to reduce the size that emulates infinite array. The first FSS design (R) is chosen to have 9 by 27 rectangular unit cells (total aperture area = 90 mm by 81 mm) and the second FSS design (C) is chosen to have 8 by 8 circular unit cells (total aperture area = 96 mm by 96 mm). See Fig. 3.10. The source is a slot antenna and is fed by a 50 Ω CPW line. The cavity height for this FPC system with rectangular or circular FSS array is 10.81 mm and 10.53 mm, respectively, obtained from the transverse

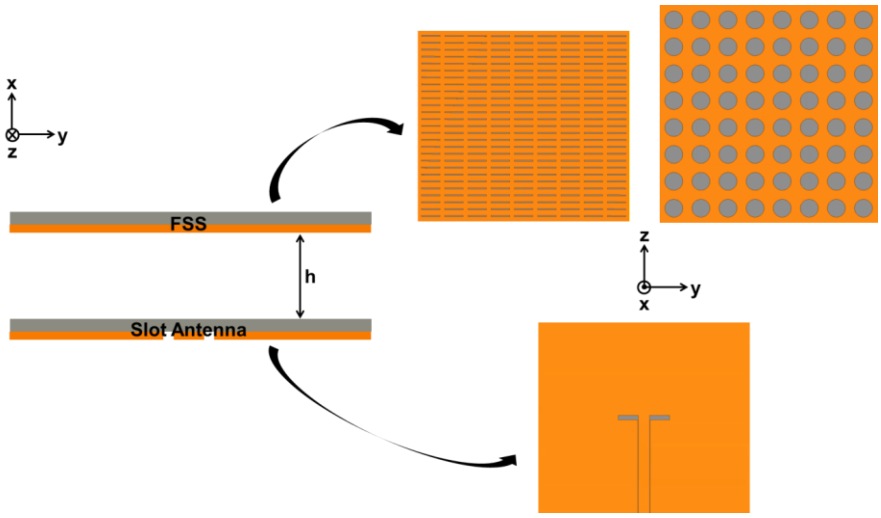

Fig. 3.10. FPC antenna systems with rectangular (R) or circular (C) FSS array

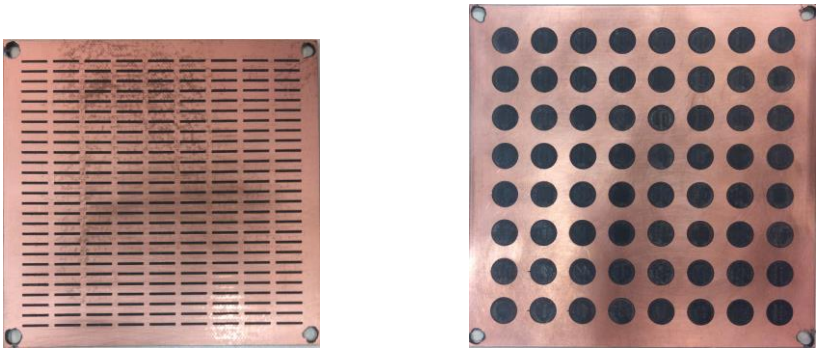

(a) (b)

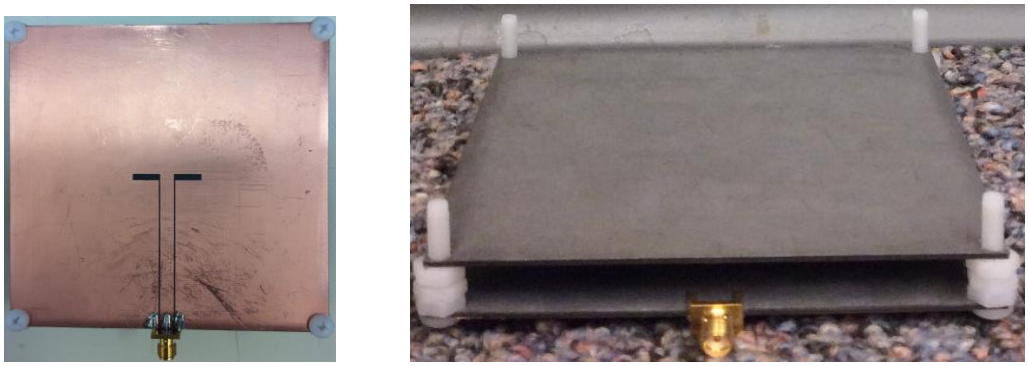

(c) (d)

Fig. 3.11. Picture of the FPC antenna systems: (a) rectangular FSS (b) circular FSS (c) slot antenna (d) FPC antenna system

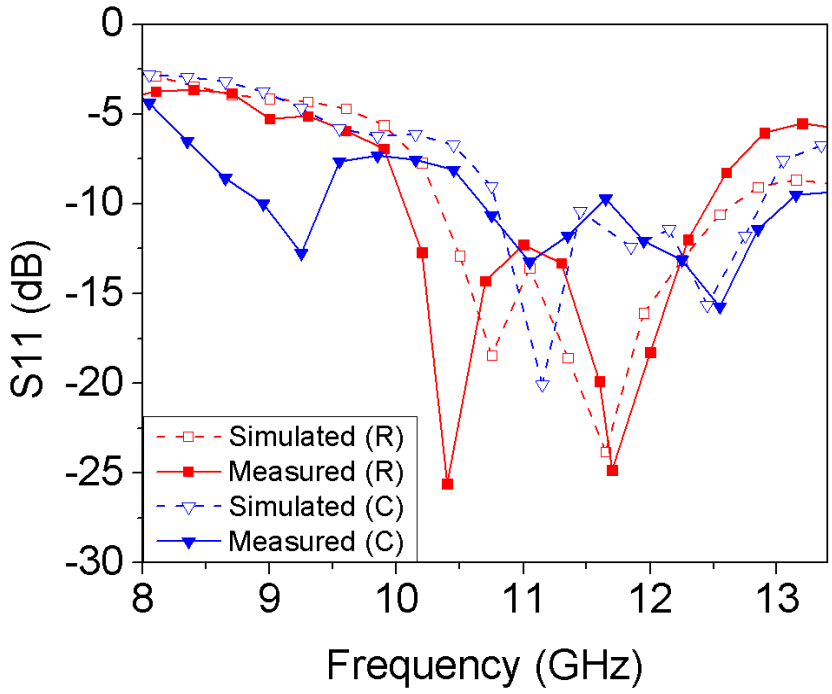

Fig. 3.12. S11 (dB) vs. frequency (GHz) of FPC antenna systems with rectangular (R) or circular (C) FSS

resonance condition. The combined FPC system designs are shown in Fig. 3.10.

3.4.2. Fabrication

All antenna and FSS designs are built on Duroid5880 (ε_r = 2.2, substrate height = 1.57 mm, metal thickness = 35 μm, tan δ = 0.0009) using a LPKF milling machine technology. All structures are assembled with nylon screw, flat washer and nut. Each board is extended to 5 mm in each direction from the total aperture area. An SMA connector feeds each antenna system. Fabricated antenna, FSS array and FPC antenna system are shown in Fig. 3.11.

3.4.3. Results

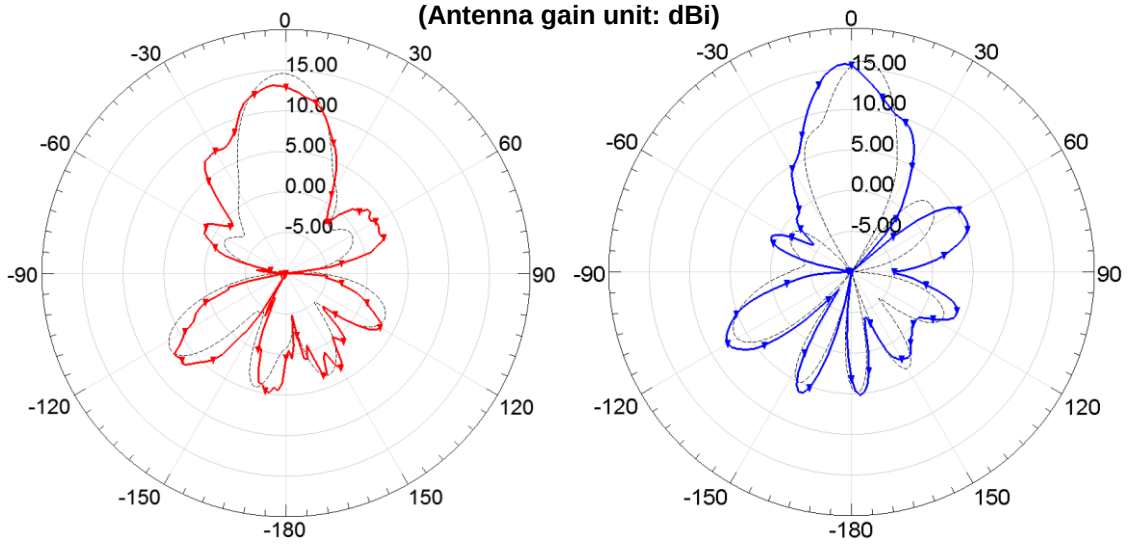

(a)

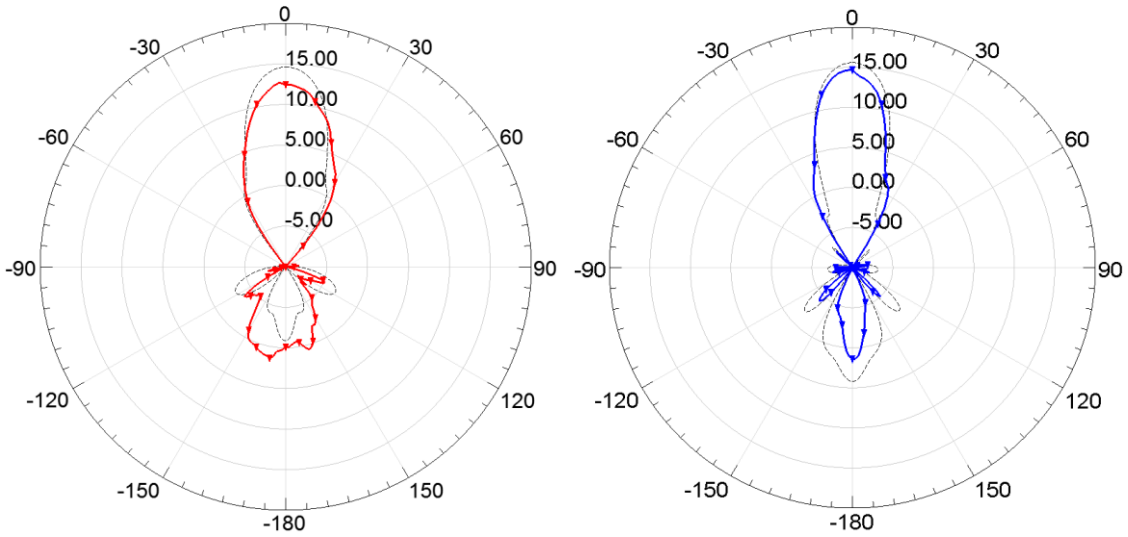

(b)

Fig. 3.13. Simulated (dashed) and measured (solid) far-field radiation patterns of FPC antenna systems with rectangular (**red**) or circular (**blue**) FSS: (a) E-plane (b) H-plane

The reflection response (S11) for FPC antenna system with rectangular or circular FSS is shown in Fig. 3.12. Good agreement between simulation and measurement is observed for both systems. For rectangular FSS design, the two resonances occur at 10.4

GHz and 11.7 GHz in measurement providing good matching (|S11| ~ -25 dB). For circular FSS design, three resonance occurs at 9.2 GHz, 11 GHz and 12.55 GHz with |S11| below -10 dB.

The optimum far-field radiation patterns are shown in Fig. 3.13. For simulation, the peak gain in both planes is 14.61 dBi at 11.2 GHz (rectangle) while the gain in E- and H-plane is 15.95 dBi and 15.58 dBi at 11.8 GHz (circle), respectively. From measurements, the peak gain for the rectangular FSS in E- and H-plane is 13.19 dBi and 12.69 dBi at 10.81 GHz whereas the peak gain for the circular FSS in E- and H-plane is 15.6 dBi and 14.7 dBi at 11.35 GHz (circle). The circular FSS increases the gain by ~ 2 dB. Also, the H-plane back lobe for the circular FSS is significantly suppressed compared to the rectangular FSS. In the section 3.2, it was discussed that the circular FSS unit cell has higher reflection (-0.0061 dB) than the rectangular one (-0.082 dB). Hence, more energy is captured inside the cavity and thus the circular FSS creates a sharper beam with higher gain in the far-field region.

3.5. Study of Source Effect in FPC Antenna Systems

3.5.1. Design

Two source antennas – slot and patch – are shown in Fig. 3.14. Each antenna operates at 12 GHz and is located in the center of the board. The slot antenna is inductively fed by a 50 Ω coplanar waveguide which has strip width of 4.83 mm, gap of 0.2 mm and length of 39.56 mm. The slot antenna has two arms with a length of 22.8 mm

(a) (b)

Fig. 3.14. Structure of two source antennas: (a) slot antenna (b) patch antenna

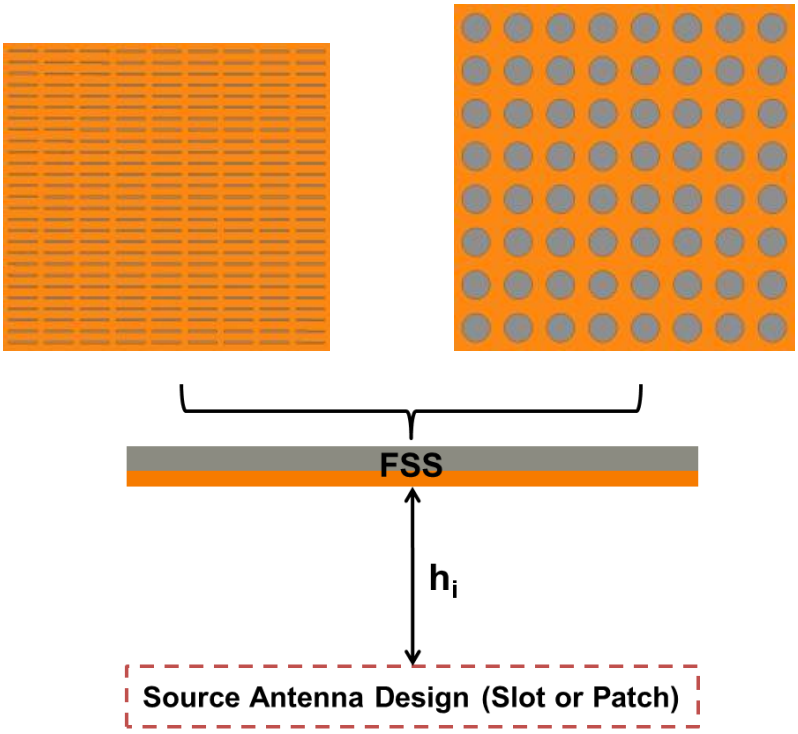

Fig. 3.15. Structure of the FPC antenna system.

and width of 1.88 mm. The patch antenna is fed by 100 Ω microstrip line with a length of 16.09 mm that is connected to a 70.7 Ω quarter-wave transformer with a length of 4.54 mm to convert the 50 Ω line with a length of 17.81 mm at the input port. The inset-fed

Table 3.5. Cavity height of the FPC antenna systems

	Slot antenna (S)	**Patch antenna (P)**
Rectangular FSS (R)	10.81 mm	10.83 mm
Circular FSS (C)	10.53 mm	10.83 mm

method is used to match the patch antenna to 100 Ω line. The patch antenna is a rectangle with a length of 7.65 mm and width of 9.88 mm.

The FPC antenna system is shown in Fig. 3.15. The slot (S) or patch (P) antenna is combined with a rectangular (R) or circular (C) FSS discussed in the section 3.4. Four FPC system designs are considered: (1) Slot with Rectangular FSS (SR) (2) Patch with Rectangular FSS (PR) (3) Slot with Circular FSS (SC) (4) Patch with Circular FSS (PC). A cavity region is formed between two substrates. The cavity height separating the FSS and antenna is obtained from the transverse resonance condition, optimized in HFSS and shown in Table 3.5.

3.5.2. Fabrication

Details for the fabrication have been discussed in the section 3.4.2.

3.5.3. Results

The reflection measurement (S11) is obtained using an Anritsu 37369D network analyzer (40 MHz – 40 GHz). A one-port coaxial calibration is used to establish a reference plane at the SMA port. Far-field radiation patterns are obtained in an anechoic antenna chamber using the desktop antenna measurement systems (DAMS). A standard

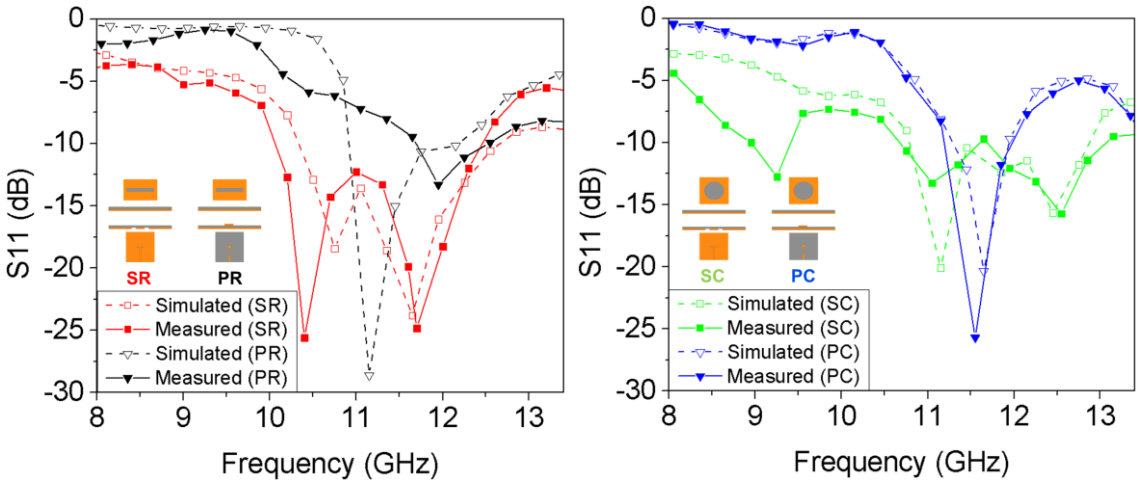

(a) (b)

Fig. 3.16. S11 (dB) vs. frequency (GHz) for FPC systems with: (a) rectangular (R) FSS (b) circular (C) FSS

gain horn antenna in X-band (8.2 – 12.4 GHz) is employed as a transmitter for the pattern measurement. A pre-amplifier in the receiver chain of the antenna measurement system is used to increase the signal-to-noise ratio.

The simulated and measured reflection coefficient (S11) on the FPC antenna systems are shown in Fig. 3.16. Each graph consists of one FSS design with either the slot or patch design. For the systems with the rectangular (R) FSS, the SR (slot) has two measured resonances at 10.4 GHz and 11.7 GHz and PC (patch) has one measured resonance at 11.95 GHz. For the systems with the circular (C) FSS, the SC (slot) has three measured resonances at 9.2 GHz, 11 GHz and 12.55 GHz and PC (patch) has one measured resonance at 11.55 GHz, which is the strongest. The bandwidth for patch (PR and PC) is narrower than slot (SR and SC) due to use of transformer. The best agreement between simulated and measured reflection response is achieved for the PC design.

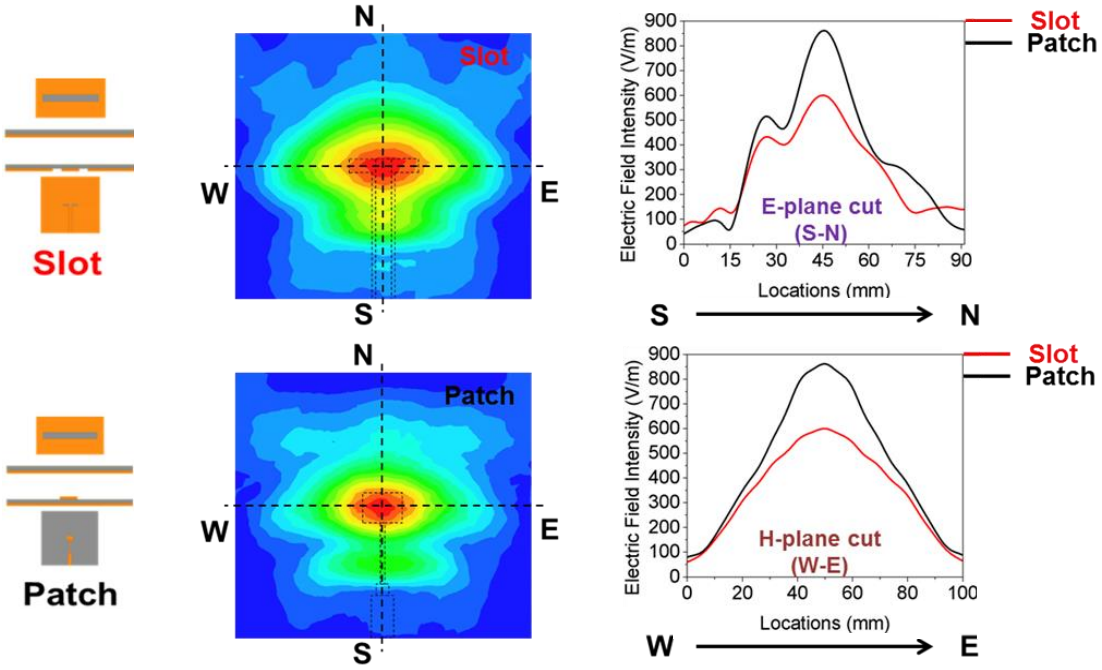

Fig. 3.17. Near-field distribution at 5 mm above FSS for FPC systems with rectangular FSS: slot (**red**) and patch (**black**) at 11.2 GHz

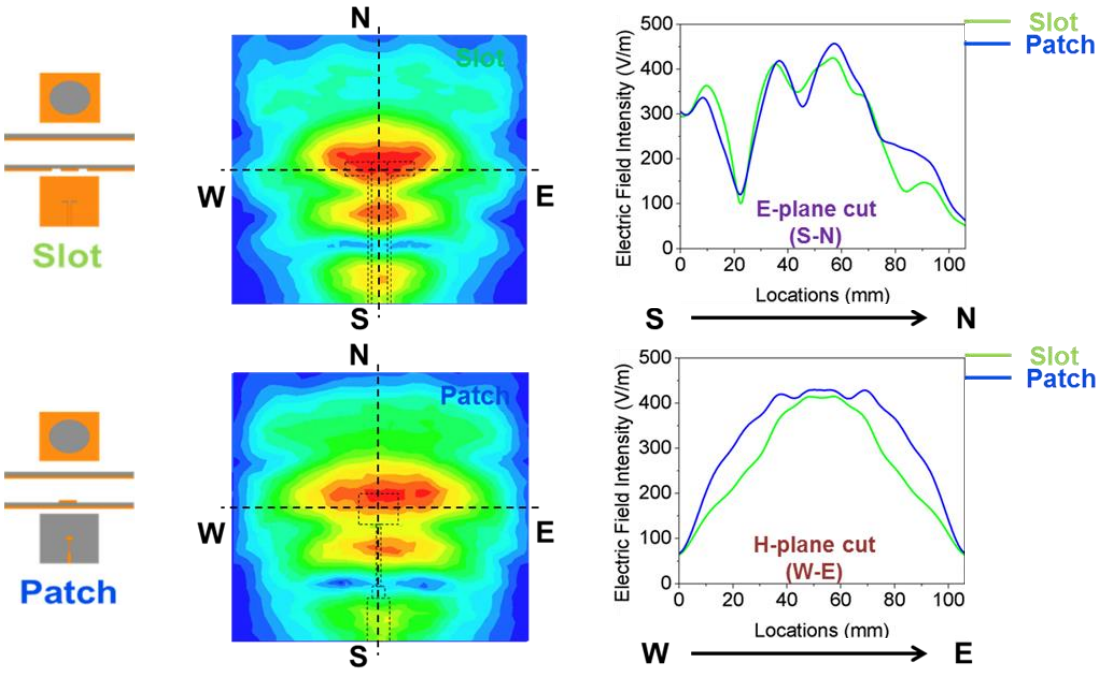

Fig. 3.18. Near-field distribution at 5 mm above FSS for FPC systems with circular FSS: slot (**green**) at 11.8 GHz and patch (**blue**) at 11.6 GHz

The near-field behavior of FPC antenna system with slot or patch for each FSS array is shown in Fig. 3.17 and Fig. 3.18. The near-field is observed a virtual reference plane, located at 5 mm above the FSS, at the frequency where the optimum beamforming is obtained. For the rectangular FSS in Fig. 3.17, the PR (patch) has stronger electric field intensity (861 V/m) concentrated around the center while the SR (slot) has less tapered distribution with the weaker intensity (601 V/m).

For the circular FSS in Fig. 3.18, the overall energy spreads out along the W-E line more than with the rectangular FSS. There are two highly concentrated field regions along the line connecting source and feedline. That is because the circular FSS has higher reflection than the rectangular one and thus it leads to additional excitation above the feedline also. The energy for the PC (patch) along the H-plane cut (W-E) is more uniformly distributed than the SC (slot).

The optimum measured far-field radiation patterns in terms of the most directive main lobe and the least side and back lobes are shown in Fig. 3.19 and Fig. 3.20. The patterns are observed over frequency sweep in X-band (8.2 – 12.4 GHz).

When comparing slot versus patch antenna using the rectangular FSS in Fig. 3.19, the measured E-plane pattern gain for the SR (slot) at 10.6 GHz is 13.41 dBi and for the PR (patch) at 10.85 GHz are 12.69 dBi. Corresponding H-plane pattern gain is 12.7 dBi (slot) and 11.54 dBi (patch), respectively. The side lobe for the SR (slot) in E-plane is larger and it supports that the near-field distribution of the slot with the rectangular FSS is less tapered as shown in Fig. 3.17.

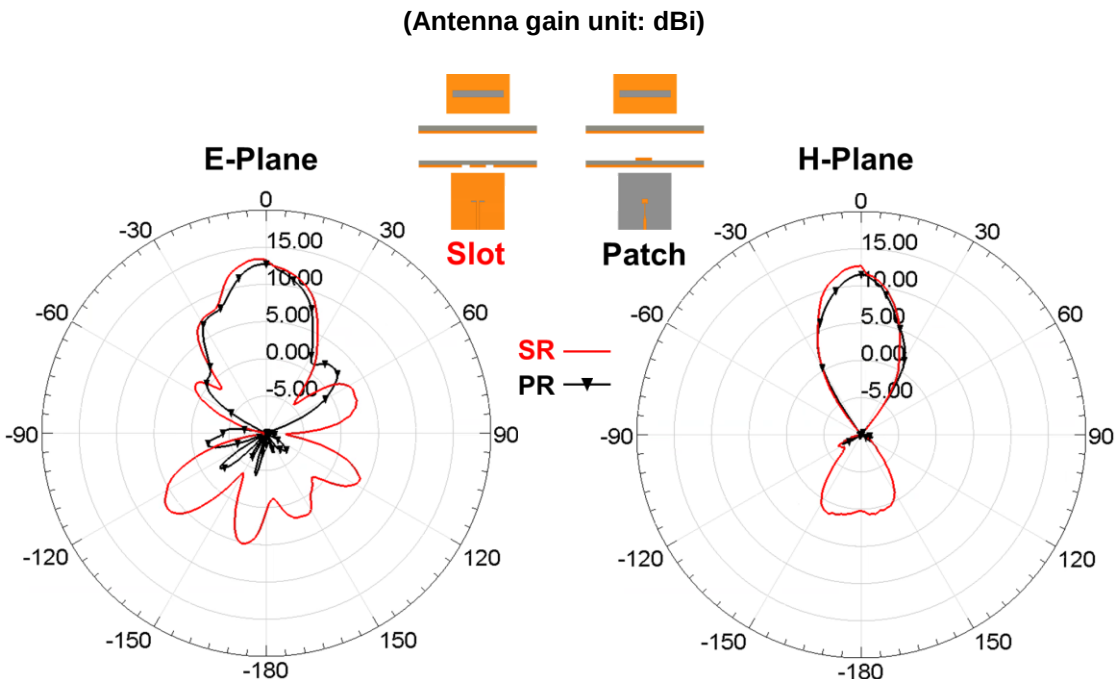

Fig. 3.19. Measured far-field radiation patterns of FPC antenna systems with rectangular FSS: slot (**red**) and patch (**black**)

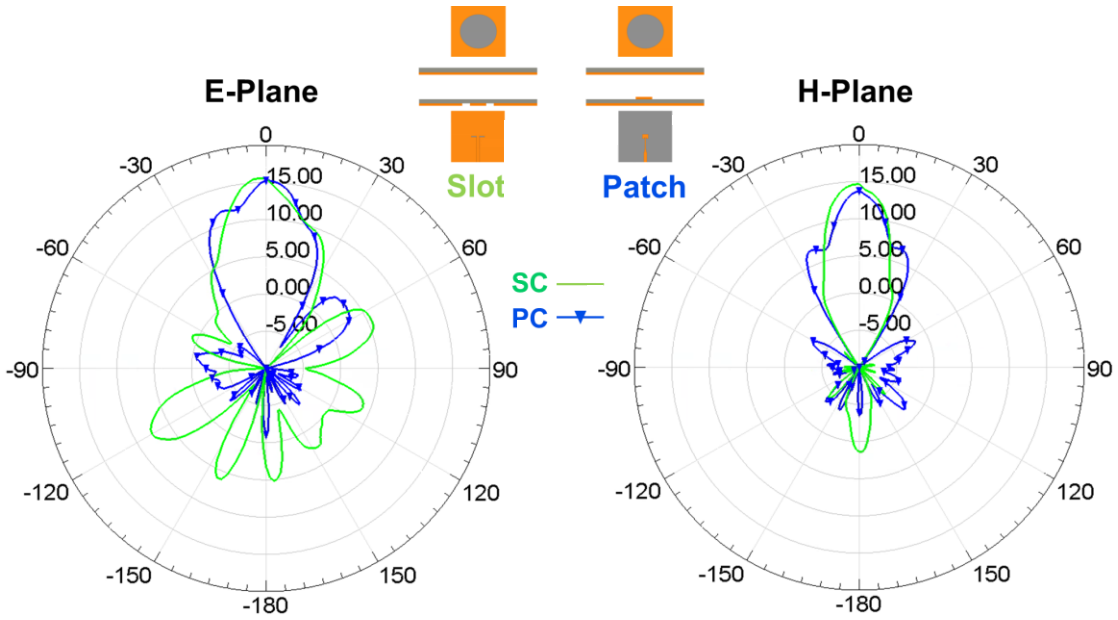

Fig. 3.20. Measured far-field radiation patterns of FPC antenna systems with circular FSS: slot (**green**) and patch (**blue**)

When comparing slot versus patch antenna using the circular FSS in Fig. 3.20, the measured E-plane pattern gain for the SC (slot) at 11.35 GHz is 15.6 dBi and for the PC (patch) at 11.55 GHz is 15.3 dBi. Corresponding H-plane pattern gain is 14.7 dBi (slot) and 13.79 dBi (patch), respectively. Both antenna types with the circular FSS array have more peak gain when compared to the sources with the rectangular FSS because the unit cell in the circular FSS array has higher reflection leading to more energy captured inside the cavity. The side and back lobes, however, increase significantly with the circular FSS compared to the rectangular one. This verifies that the circular FSS array is more uniformly illuminated as shown in Fig. 3.18. In terms of source type, the side lobe for the PC (patch) in H-plane is larger than for the SC (slot) which is consistent with the fact that the near-field of the PC (patch) is more uniformly distributed in H-plane as shown in Fig. 3.18.

3.6. Summary

In this chapter, the FPC antenna systems are parametrically and comparatively studied to understand how each FSS layer and/or source configuration affect the performance.

First, FSS designs evaluated with rectangular, circular and square unit cells were considered and it is concluded that energy leakage was more dependent on the aperture width (W) rather than the aperture length (L) of rectangular unit cells. The effect of the aperture ratio on leakage is more significant for square unit cell than for circular one.

Second, based on the unit cell results, an FPC antenna system with a bi-directionally radiated slot antenna and rectangular FSS array was proposed for a parametric study. Three parameters – cavity height, unit cell aperture length and width – are considered. Near-field distribution and far-field radiation patterns are significantly controlled by the cavity height and aperture width (W) of the unit cell. Aperture length (L) of the unit cell effect were minor for changes between -20 % and +20 % of the baseline length.

Lastly, for FSS geometry effect, the peak gain of the FPC system with circular FSS array increases by 2 dB with reduction of back lobe compared to rectangular FSS. For source effect, the FPC antenna system using the circular FSS design with the slot antenna has highest peak gain compared to the rectangular FSS. The FPC antenna system using the circular FSS design with the patch antenna achieves simultaneously the best impedance matching (|S11| = -25 dB) and maximum gain at one resonant frequency. Therefore, the slot design is best with the circular FSS for beamforming capability and the patch design is best with the rectangular design to suppress the side and back lobes.

CHAPTER 4

Characterization of FPC Antenna Systems

4.1. Introduction

The open cavity FPC system with bi-directionally radiated slot antenna, which has been discussed so far, focuses the antenna's energy to form a more directive and/or high gain beam using FSS. One side effect, however, is that the FSS will also focus energy associated with the feedline in the near-field, which can degrade far-field radiation patterns. Also, the open cavity FPC system suffers from energy leakage on the sides of the cavity region and out the back of the antenna. This leakage can have adverse effects on neighboring electronic elements located in close proximity and can result in unintended interference and coupling. In this chapter, the effect of coplanar waveguide (CPW) feedline on FPC antenna systems is studied. Also, the design approaches to alleviate FSS focusing of CPW feedline energy are presented. Lastly, leakage effects on FPC antenna system hinder performance due to cavity design and source antenna radiation direction is studied.

4.2. Feedline Effect on FPC Antenna Systems

4.2.1. Design

To investigate the CPW feedline effect, three FPC system designs are considered as

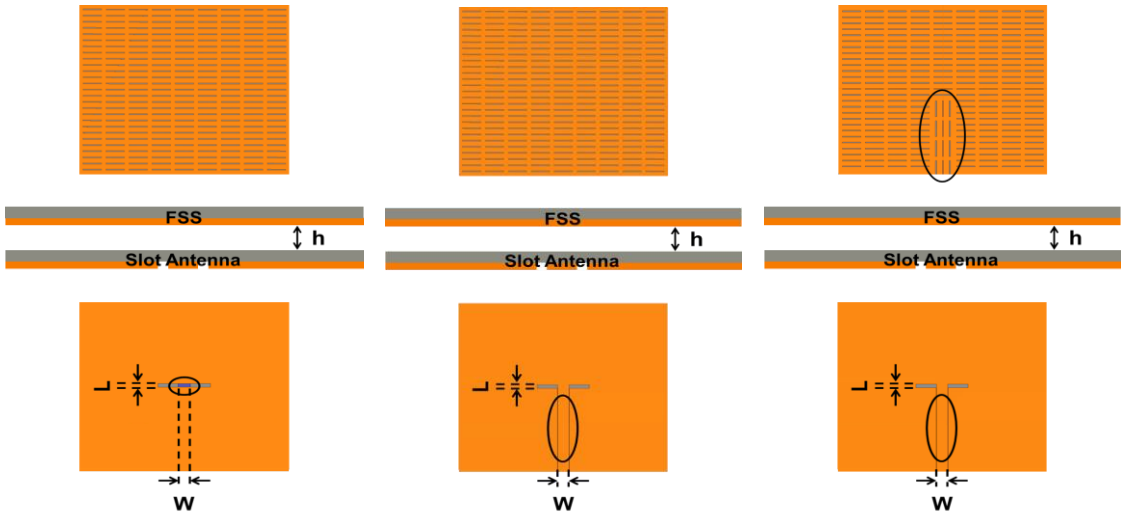

(a) (b) (c)

Fig. 4.1. FPC antenna systems: (a) FSS-AH with lumped port excitation (b) FSS-AH with CPW-fed slot antenna (FSS-AH+CPW) (c) FSS-1V with CPW-fed slot antenna (FSS-1V+CPW)

shown in Fig. 4.1: (1) FSS with all horizontal unit cells with lumped port-excited slot antenna (FSS-AH+LP) (2) FSS-AH with CPW-fed slot antenna (FSS-AH+CPW) (3) FSS with one column of vertically oriented unit cells above where the CPW feedline resides with CPW-fed slot antenna (FSS-1V+CPW) [41]. Lumped ports are used in HFSS to excite and analyze the structures in perspective of voltage and current. Lumped ports can be located internally with a complex user-defined impedance and compute S-parameters directly at the port. In this study, a lumped port resides and fits in the center of the slot antenna. The width (W) and length (L) of the port corresponds to 5.23 mm (CPW width, 4.83 mm+2*gap, 2*0.2 mm) and slot width of 1.88 mm, respectively. All details of the slot and FSS designs have been discussed in the section 2.3. In real systems a feedline exists and in this work coplanar waveguide (CPW) is needed. The following study discusses how FPC system with CPW feedline is affected by FSS focusing.

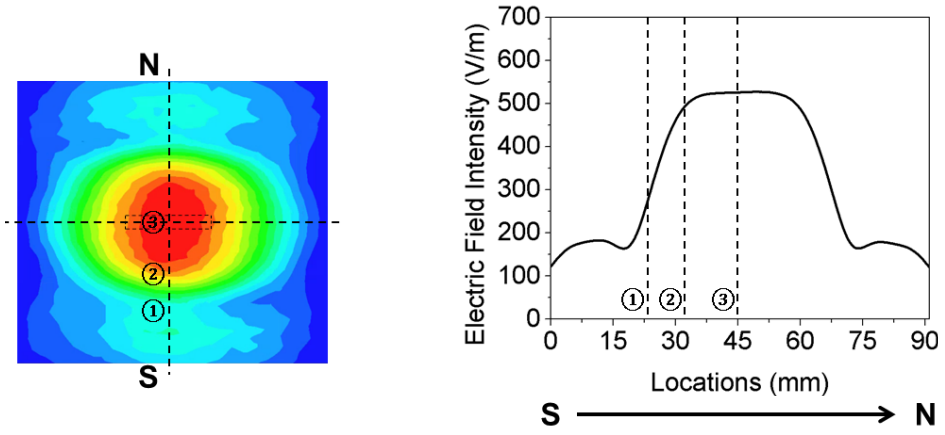

(a)

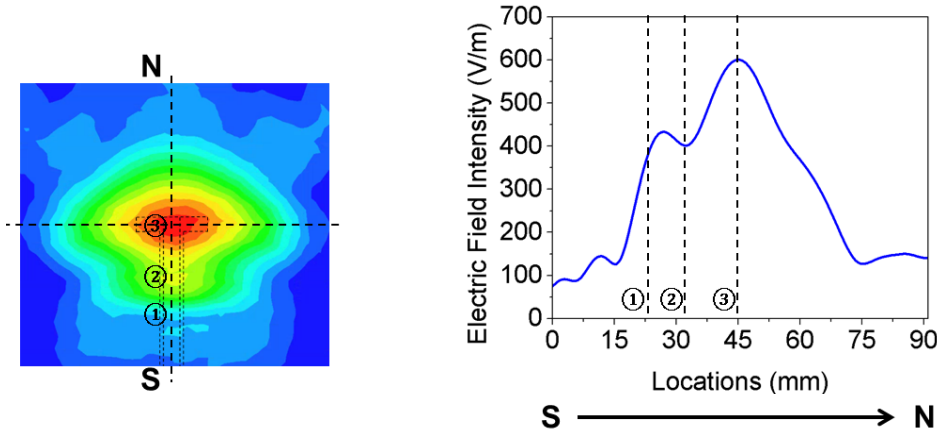

(b)

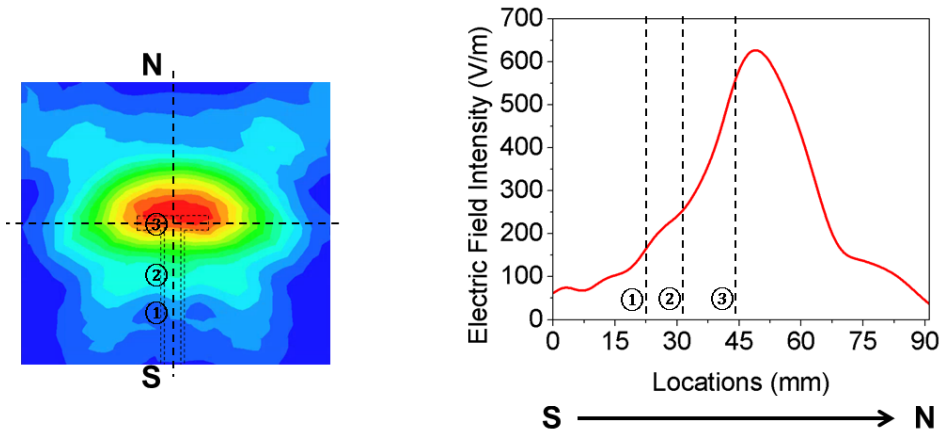

(c)

Fig. 4.2. 2D near-field distribution (left) and electric field intensity along S-N direction (right): (a) FSS-AH+LP (b) FSS-AH+CPW (c) FSS-1V+CPW

4.2.2. Results

The near-field distribution 5 mm above each FSS at 11.2 GHz is shown in Fig. 4.2. The S-N line is defined and chosen to observe the feedline effect. For FSS-AH+LP design in Fig. 4.2(a), a circular shape of electric field is uniformly distributed around the slot and spreads out uniformly in all directions with a circular shape from the center and the peak intensity at '3' is 527 V/m. When the CPW feedline is integrated (FSS-AH+CPW) in Fig. 4.2(b), energy over the feedline leaks out through FSS-AH and an asymmetric field is observed along the S-N direction due to the feedline. The oval shape of field is formed near the slot with a lower intensity tail of energy in the direction of the feedline and the peak intensity at '3' increases to 601 V/m and the field at '2' above the feedline is 402 V/m. When the vertically oriented unit cells are included in the FSS-AH (FSS-1V+CPW) in Fig. 4.2(c), the strongest field is slightly shifted from the center of the slot. The peak intensity at '3' increases slightly to 627 V/m and the field becomes more symmetrically tapered along the S-N line with a reduction (~ 269 V/m) of the field intensity at '2'. It demonstrates that vertically oriented unit cells prevent feedline energy from leaking out through FSS and reduce the near-field feedline effect.

The simulated and measured optimum radiation patterns are shown in Fig. 4.3. For the FSS-AH+CPW case, the measured peak gains at 10.81 GHz in E- and H-plane are 13.19 dBi and 12.69 dBi, respectively. For the FSS-1V+CPW case, the peak gains at 11.15 GHz in E- and H-plane are 13.34 dBi and 12.05 dBi, respectively. Including the vertically oriented unit cells over the feedline suppresses the feedline radiation and improves the E-plane radiation pattern symmetry slightly. The augmented reflective

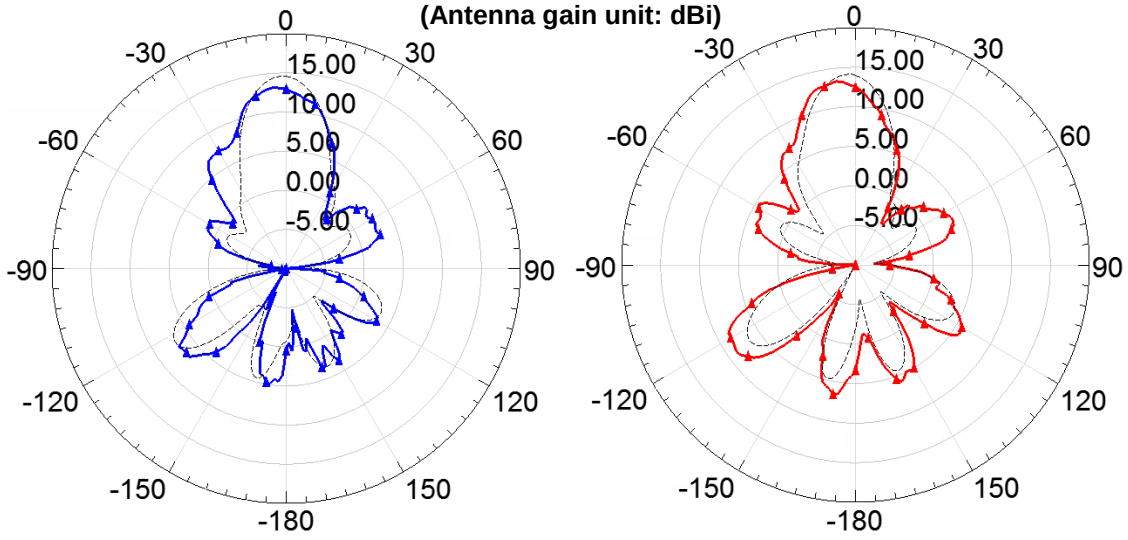

(a)

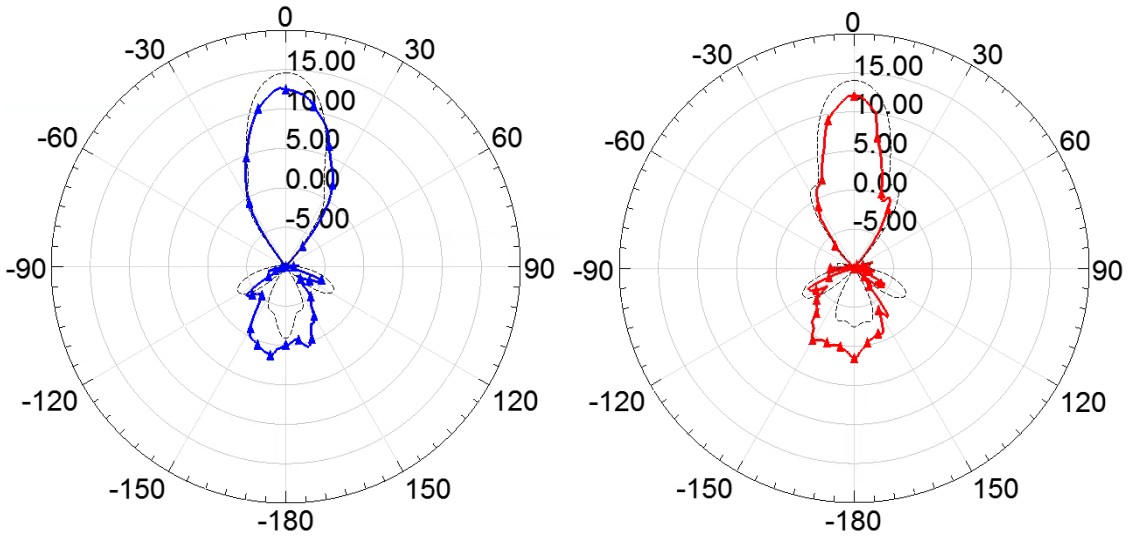

(b)

Fig. 4.3. Simulated (dashed) and measured (solid) far-field radiation patterns for FSS-AH+CPW (**blue**) and FSS-1V+CPW (**red**): (a) E-plane (b) H-plane

surface, however, creates a slight increase in the side and back lobe due to the increased reflection inside the cavity. A slight steering of the E-plane beam away from the center is observed and can be explained by the shift in the near-field concentration as shown in Fig. 4.2(c).

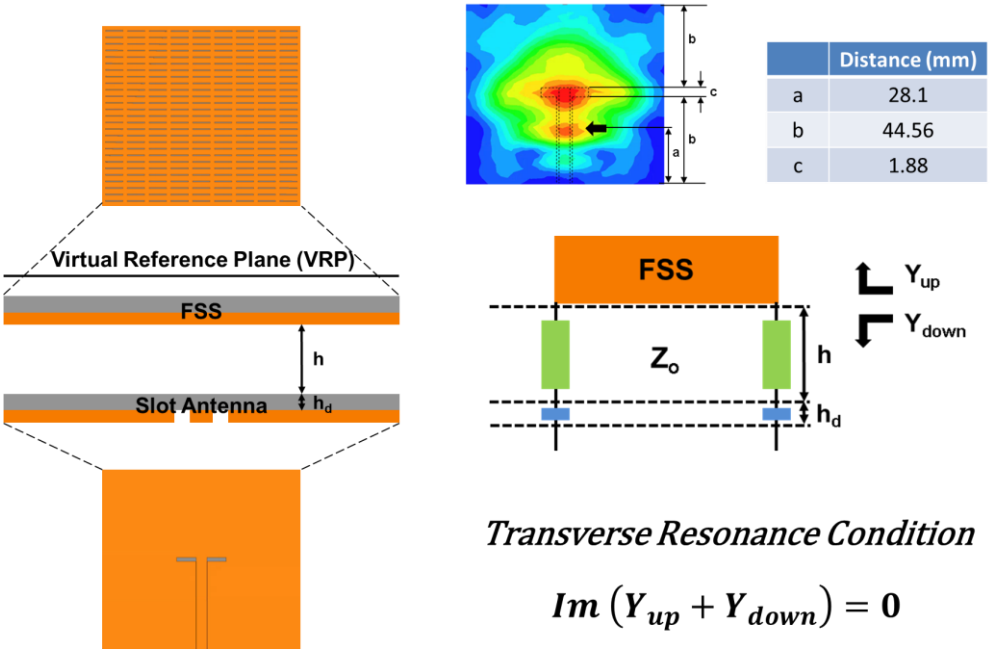

(a) (b)

Fig. 4.4. (a) Open-air cavity FPCA system (b) field distribution above FSS (top right) and circuit model of the FPCA system (bottom right)

4.3. FSS Designs for Coplanar Waveguide Feedline Suppression

4.3.1. Design

An FPC antenna system (FPCA) with an open air-cavity between FSS and antenna layers, as discussed in the previous section, is shown in Fig. 4.4. A CPW-fed slot antenna radiates bi-directionally through an FSS, which has 9 by 27 horizontally oriented unit cells. The cavity height (h) of 10.81 mm is obtained from the transverse resonance condition when the imaginary part of the total admittance (Y_{up}+Y_{down}) is zero as shown in Fig. 4.4(b). A virtual reference plane (VRP) is located 5 mm above the FSS to monitor antenna and feedline behavior in the near-field as shown in Fig. 4.4(a).

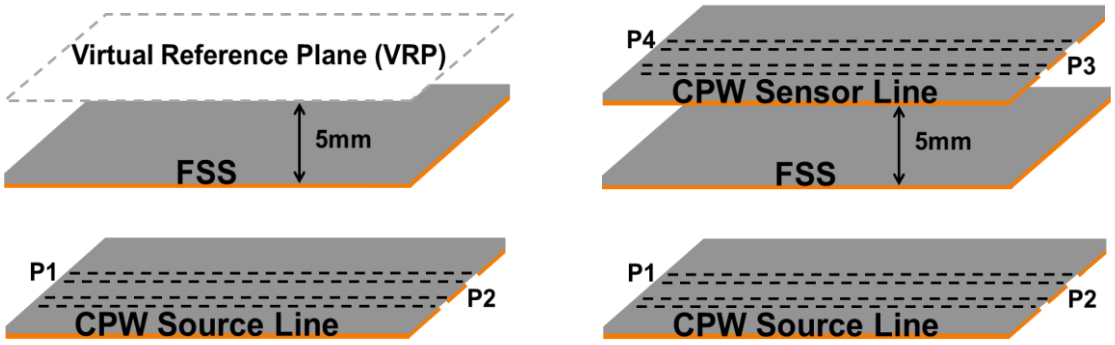

(a) (b)

Fig. 4.5. Cross-section view of the circuit with CPW source line: (a) HFSS model (b) test circuit. All CPW lines point down and are shown as dashed hidden lines on the substrate

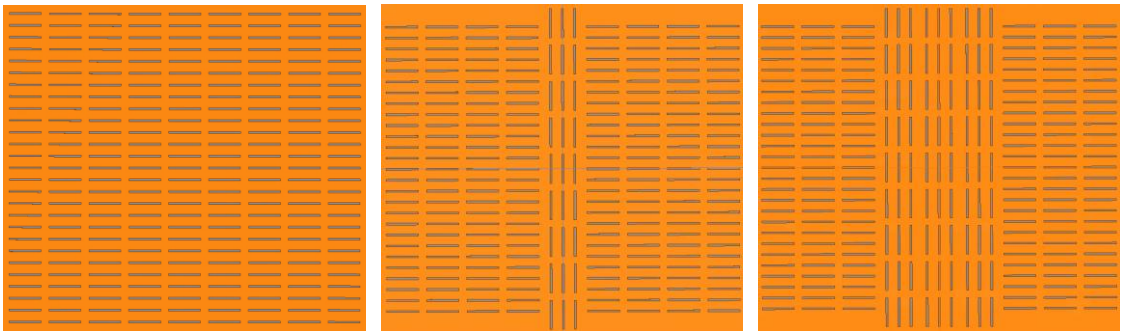

(a) (b) (c)

Fig. 4.6. Top view of the FSS array designs: (a) FSS with all horizontal unit cells (FSS-AH) (b) FSS with one vertical column (FSS-1V) (c) FSS with three vertical columns (FSS-3V)

Two highly concentrated electric field is observed at position ‘c’ and ‘a’ above the feedline, respectively. The radiating element, slot antenna, produces the strongest concentrated field at position ‘c’ in the center. The feedline, a non-radiating element, also shows focused concentration at position ‘a’ that is excited due to multiple reflections inside the cavity. As a result, the concentrated field is observed for a signal peak over the feedline location (b-a) which corresponds to $3\lambda/4$.

In this study, feedline beam focusing behavior is investigated for orientation-

sensitive FSS designs. Performance is evaluated by studying (1) near-field distribution simulations, (2) near-field coupling measurements and (3) far-field radiation pattern simulations. All designs use a 50 Ω CPW source line below the FSS.

For near-field studies, the feedline energy is evaluated at the VRP located 5 mm above the FSS. In simulation, HFSS uses the VRP (Fig. 4.5(a)) for detection whereas in measurements a CPW sensor line (Fig. 4.5(b)) is used in lieu of that plane. For far-field radiation patterns, all surfaces are set to the radiation boundary condition.

Four FPC transmission line (FPC-TL) designs are studied using a CPW source line. First, no-FSS is used as a benchmark to determine a reference value for the CPW source line peak energy. Second, FSS-AH in Fig. 4.6(a), has nine horizontal unit cell columns in the FSS. Third, FSS-1V in Fig. 4.6(b), has eight horizontal unit cell columns and one vertical column in the center. Lastly, FSS-3V in Fig. 4.6(c), has six horizontal unit cell columns and three vertical columns in the center.

The FSS unit cell was designed to have a high reflection of -0.085 dB and simulated in HFSS. Each unit cell is rectangular with a rectangular aperture in the center. The FSS array was optimized to obtain the minimum size of 9 by 27 unit cells that emulates the infinite array. One horizontal column is defined as 27 horizontal unit cells. One vertical column is defined as 9 rows of vertical unit cell sets, where each set has 3 vertically oriented unit cells as shown in Fig. 4.6.

Vertically oriented unit cells prevent the electric field radiated from the CPW gaps from leaking out through FSS. Each design is analyzed and compared to a reference design (FSS-AH). The feedline focusing reduction is evaluated by varying the number of

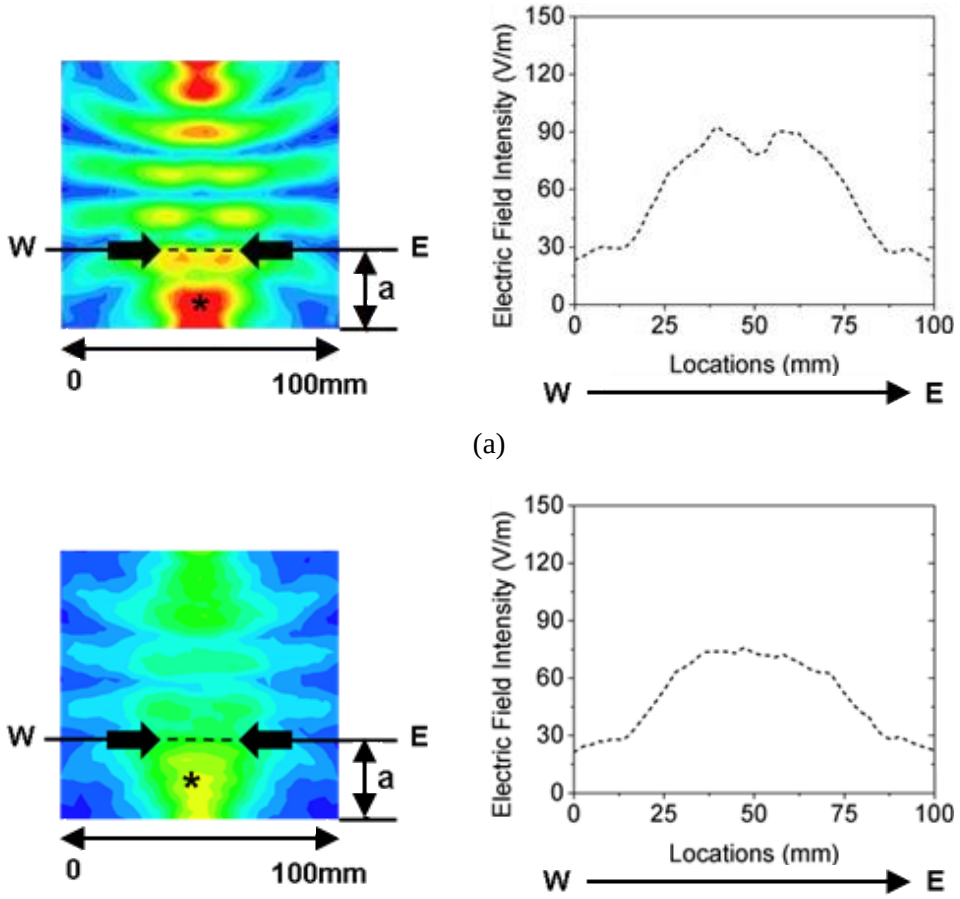

Fig. 4.7. 2D near-field distribution (left) and 1D near-field intensity along W-E line (right) of the HFSS model for the FPC-TL systems with no-FSS (a) at the surface of the CPW source line the * is 200 V/m (b) at the VRP the * is 127 V/m

Table 4.1. Field intensity for four cases

	E_{max} (*) (V/m)	$E_{feedline}$ (---) (V/m)
no-FSS	127	73
FSS-AH	160	137
FSS-1V	99	50
FSS-3V	85	26

vertical sets.

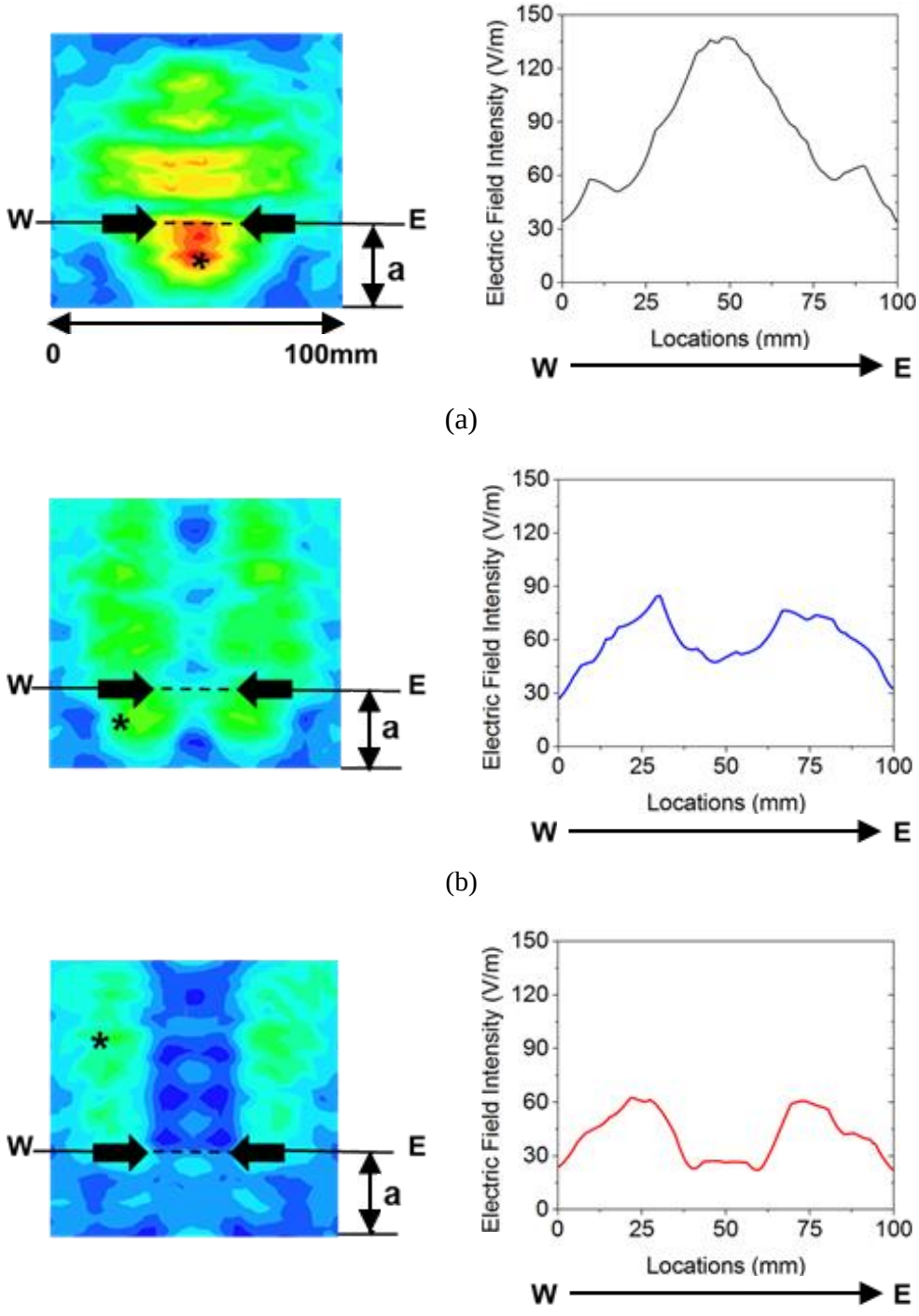

Fig. 4.8. 2D near-field distribution (left) and 1D near-field intensity along W-E line (right) of the HFSS model for the open air-cavity FPC-TL systems (a) FSS-AH, the * is 160 V/m (b) FSS-1V, the * is 99 V/m (c) FSS-3V, the * is 85 V/m

4.3.2. Fabrication

All designs are fabricated on Rogers Duroid5880 (ε_r = 2.2, substrate height = 1.57 mm, metal thickness = 35 μm, tan δ = 0.0009). CPW lines and FSS are combined using nylon screws, nuts and flat washer.

4.3.3. Results

The simulated near-field distribution for CPW source line with no-FSS on the surface of the line and at the VRP above the line is shown in Fig. 4.7(a) and (b), respectively. The peak signal strength diminishes from 90 to 73 V/m at position ‘a’ from the input port shown in Fig. 4.4(a) as the VRP moves away from the CPW line surface.

When the FSS-AH is included, the peak intensity at position ‘a’ almost doubles to 137 V/m due to the beam focusing through the FSS horizontal unit cells. Hence, when the FSS-AH is used in FPCA systems, it also focuses feedline peak energy at the VRP in the near-field region.

The near-field distribution and electric field intensity versus position for three FSS designs are shown in Fig. 4.8: (1) FSS-AH, (2) FSS-1V and (3) FSS-3V. At the position ‘a’ along the feedline, the field intensity reduces as the number of vertical unit cell sets increases as shown in Table 4.1.

The maximum electric field intensity (E_{max}), denoted by ‘*’, however, is displaced away from the feedline when the vertical unit cell sets are incorporated, because the field is suppressed over the feedline. For FSS-1V case, the CPW peak intensity reduces to 50 V/m (64 % reduction) and for FSS-3Vcase reduces to 26 V/m (81 % reduction) when compared to FSS-AH.

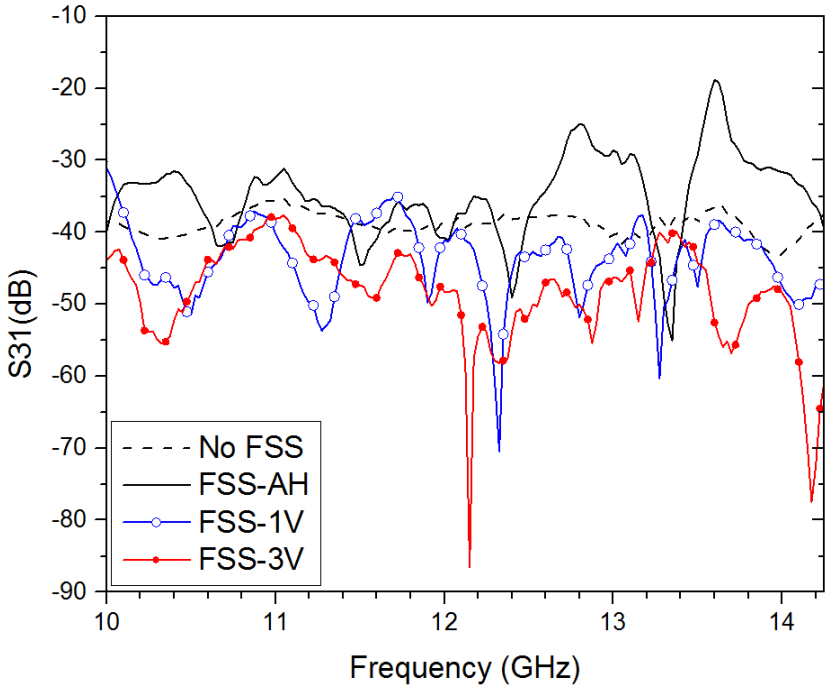

Fig. 4.9. Coupling response (S31) vs. frequency

An Anritsu 37369D network analyzer is used from 10 to 14.2 GHz and the full two-port calibration is performed. The calibration establishes the reference planes at the SMA connector interface to the circuit for S-parameters.

The measurement results of a coupled signal (S31) between the CPW source line and CPW sensor line are shown in Fig. 4.9. S31 is a measure of the focused CPW energy at the VRP above the FSS. The input signal at Port 1 of the CPW source line radiates through the FSS and is detected as a coupled signal at Port 3 of the CPW sensor line. The sensor line is located at the position of the VRP. Ports 2 and 4 are match-terminated in 50 Ω.

The benchmark no-FSS design has an average detected signal range of -41 to -35 dB. The highest signal energy is detected in the FSS-AH case. FSS-AH design couples

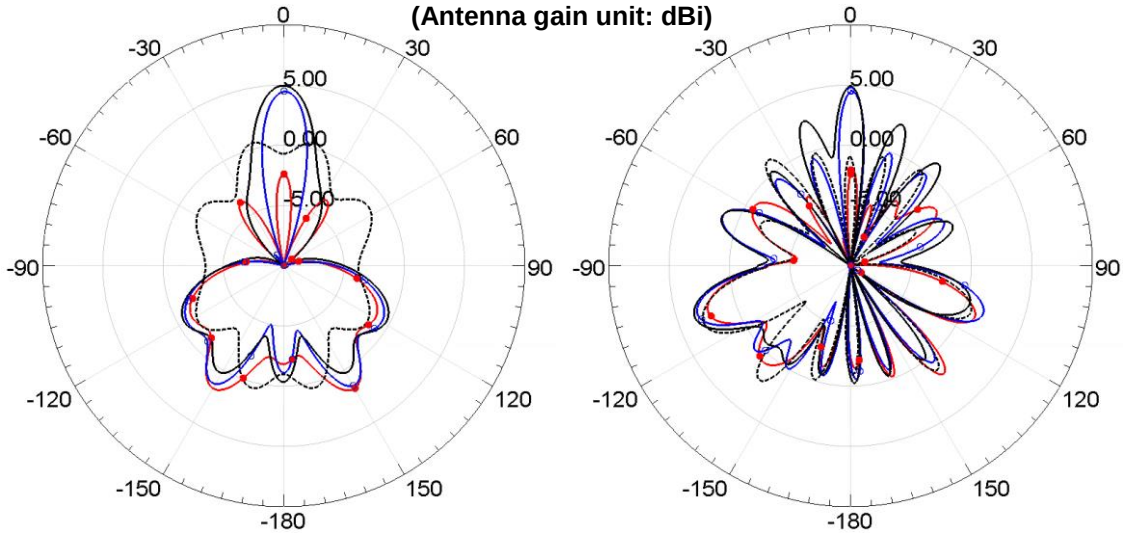

(a) (b)

Fig. 4.10. Simulated far-field radiation patterns for four FPC-TL systems: no-FSS (black-dashed), FSS-AH (black solid), FSS-1V (**blue**) and FSS-3V (**red**): (a) E-plane (b) H-plane

peak energy of the CPW line in the range of 5 and 20 dB compared to the no-FSS design for 60 % of the test frequency range. The maximum coupling occurs at 13.6 GHz and it shows the coupling doubles (-19 dB) compared to the no-FSS coupling. Near-field coupling measurements for FSS-1V and FSS-3V are decreased across most (83 %) or all (100 %) of the test frequency range below the no-FSS case, respectively. The coupling with FSS-1V reduces from 3 – 47 dB for 83 % of the test band and with the FSS-3V, has the smallest reduction of 1 dB at 13.4 GHz and the largest reduction of 45 dB at 12.2 GHz. Therefore, the integration of FSS-1V and FSS-3V successfully suppress feedline beam focusing compared to the reference FSS-AH design.

The simulated far-field radiation patterns for four FPC-TL systems at 11.4 GHz are shown in Fig. 4.10. For the no-FSS case, the pattern has reference gain of -0.85 dBi at boresight in both E- and H-planes. The FSS-AH boresight gain increases considerably to

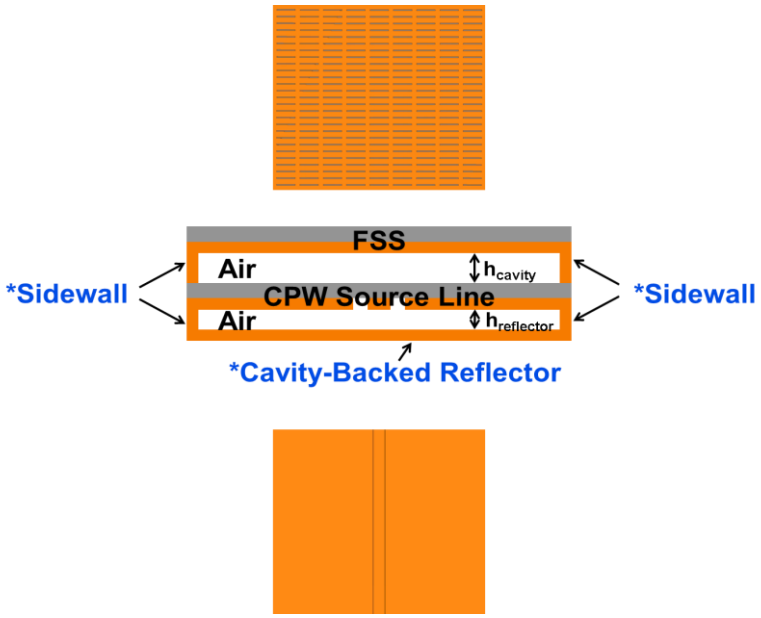

Fig. 4.11. Structure of the enclosed air-cavity FPC system with a CPW source line

4.95 dBi due to FSS beam focusing. The modified FSS-AH array decreases far-field pattern gain in both cases. For the FSS-1V case, the peak gain reduces to 4.55 dBi for FSS-3V reduces considerably to -2.4 dBi. The latter design decreases the gain of the FSS-AH by ~ 7 dB.

The open air-cavity system lacks metallic sidewalls in the air cavity region which can lead to energy leakage. To understand this impact, the enclosed air-cavity design is also investigated. It consists of two parts as seen in Fig. 4.11. Four metallic sidewalls are used to enclose the air cavity region separating the CPW line and FSS. The CPW source line can radiate below the structure also. This is alleviated by including a reflector $\lambda_o/4$ below the line and enclosing that region with four metallic sidewalls. This structure represents unidirectional radiation from the CPW line. All dimensions are the same as the open case with the addition of the lower enclosure forming the cavity-backed reflector underneath CPW source line.

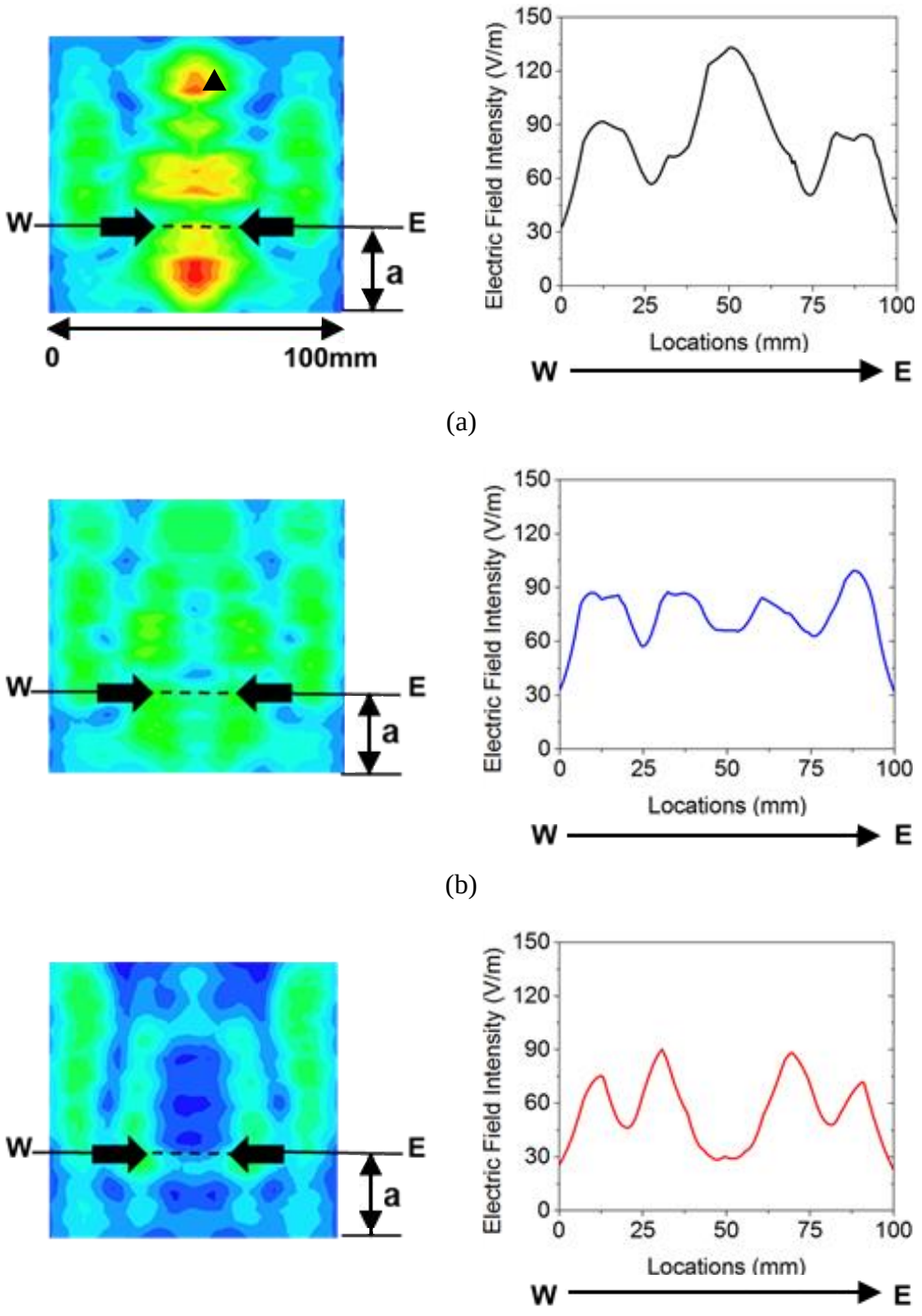

Fig. 4.12. 2D near-field distribution (left) and 1D near-field intensity along W-E line (right) of the HFSS model for the enclosed air-cavity FPC-TL systems (a) FSS-AH (b) FSS-1V (c) FSS-3V

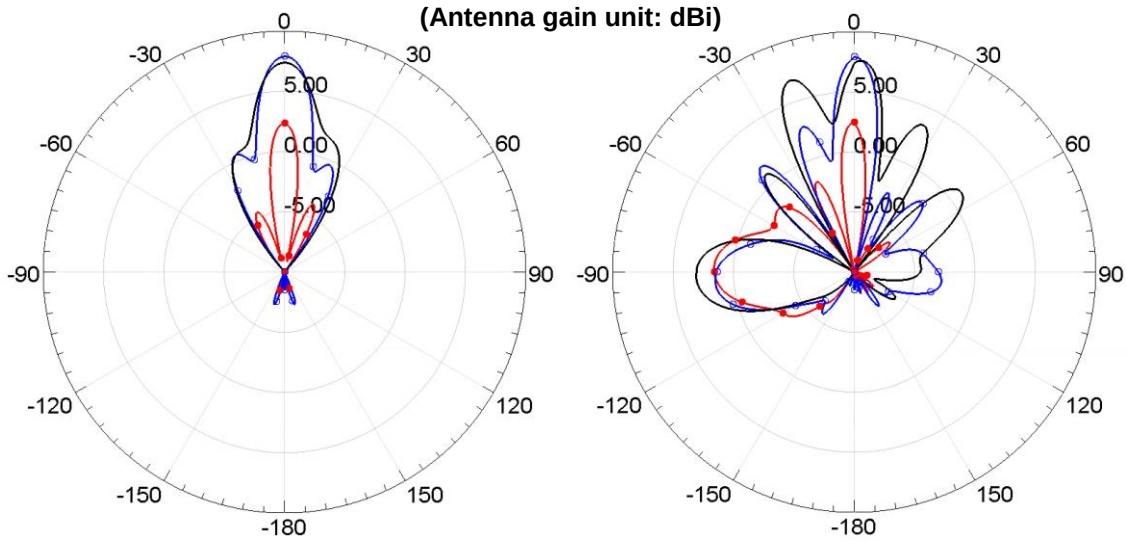

Fig. 4.13. Simulated far-field radiation patterns for three enclosed air-cavity FPC-TL systems: FSS-AH (**black**), FSS-1V (**blue**) and FSS-3V (**red**): (a) E-plane (b) H-plane

The near-field distribution at the VRP above the FSS is shown in Fig. 4.12. The cavity-backed enclosure introduces a third high intensity signal along the line (▲) as shown in Fig. 4.12(a). As expected, the overall field intensity slightly increases due to metallic enclosure compared to open-air cavity systems. It also demonstrates that FSS-1V and FSS-3V designs suppress the energy focused through FSS for enclosed air-cavity systems in a more uniform manner.

The simulated far-field radiation patterns are shown in Fig. 4.13. The inclusion of the cavity-backed reflector suppresses the side and back lobes observed in Fig. 4.10 for the open cavity system as expected. The overall peak gain also increases and the side lobes are suppressed. The FSS-3V reduces the gain of the FSS-AH by ~ 8 dB, which is similar to the open-air cavity systems. Thus, the FSS-3V suppresses the most energy from the feedline, mitigating unintended feedline radiation in the far-field region.

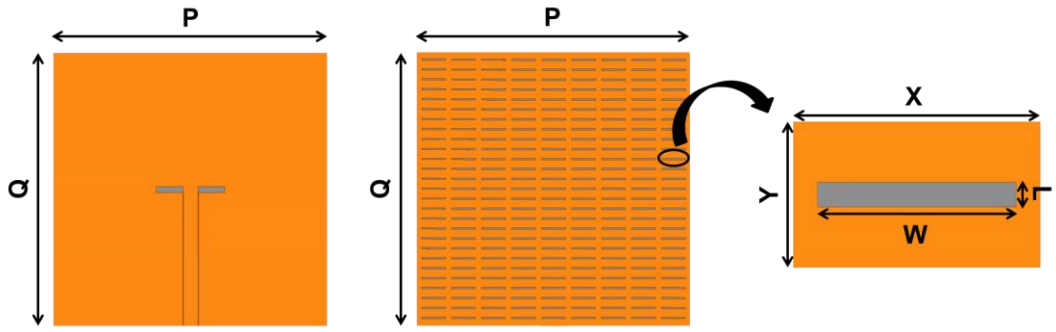

(a) (b) (c)

Fig. 4.14. Structure of FPC antenna system: (a) slot antenna (b) FSS array (c) unit cell in FSS array (P × Q = 90 mm × 81 mm)

4.4. Leakage-Controlled FPC Antenna Systems

4.4.1. Design

The slot antenna and FSS design used in the FPC antenna system study are shown in Fig. 4.14. The slot antenna is designed to operate at 12 GHz and is located in the center of the ground plane with P = 90 mm and Q = 81 mm. The antenna has a length of 22.8 mm and width of 1.88 mm. It is fed with a 50 Ω coplanar waveguide having strip width of 4.83 mm, gap of 0.2 mm and length of 39.56 mm. The FSS array is designed to operate at 12 GHz and have reflection coefficient of -0.085 dB. It consists of 9 by 27 unit cells of rectangular aperture array and has a total surface area of P = 90 mm by Q = 81mm. Each rectangular aperture has width (W) of 8 mm and length (L) of 0.5 mm and it is centered in a rectangular unit cell whose width (X) is 10 mm and length (Y) is 3 mm.

Four FPC antenna system designs are described in Fig. 4.15. Each system consists

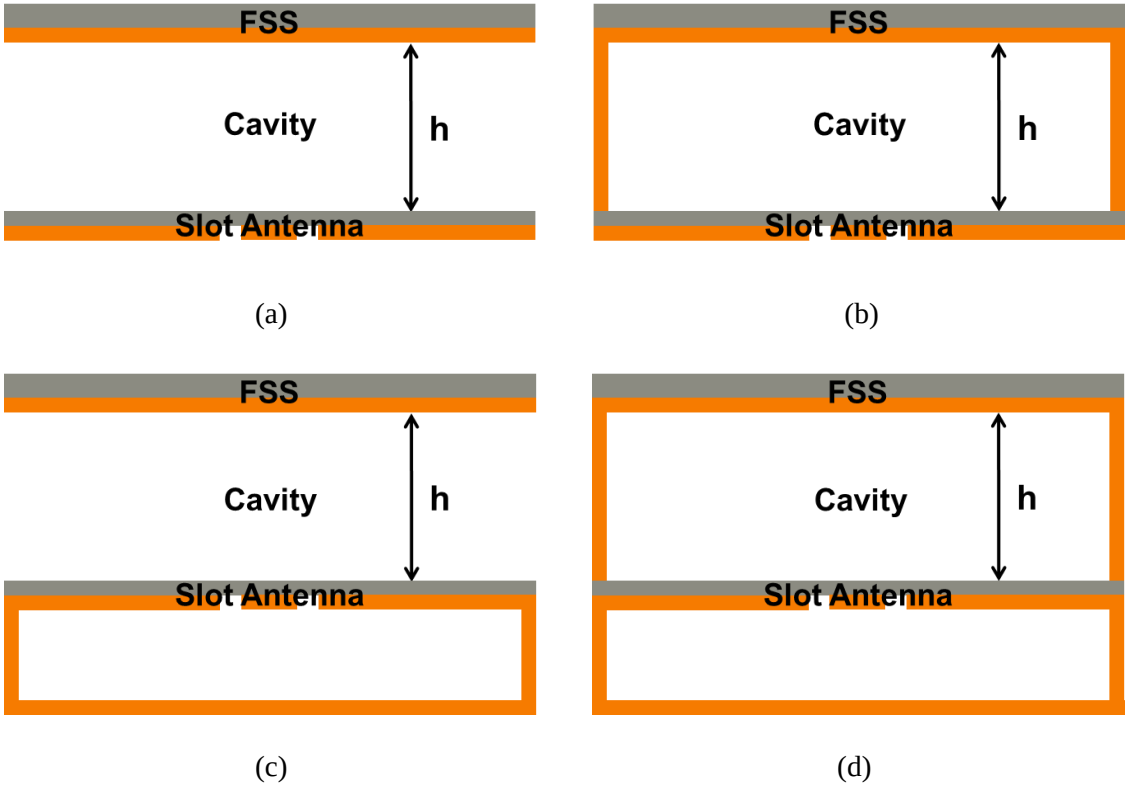

Fig. 4.15. Cross-section side view of the FPC antenna system designs: (a) slot with open cavity (S-OC) (b) slot with enclosed cavity (S-EC) (c) cavity-backed slot with open cavity (CBS-OC) (d) cavity-backed slot with enclosed cavity (CBS-EC)

of a slot antenna and rectangular FSS array as shown in Fig. 4.14 and has a cavity that is formed between the two layers. The cavity height (h = 10.81 mm) for all cases is obtained from transverse resonance condition and is simulated in full wave simulations (ANSYS HFSS). The FSS metal surface points into the cavity while the slot antenna metal surface points away from the cavity. Two antenna types are studied: (i) slot with bi-directional radiation and (ii) cavity-backed slot with uni-directional radiation.

For slot antenna with open cavity (S-OC) case (Fig. 4.15(a)), energy from the source radiates bi-directionally – above and below the antenna. Above the antenna, when electromagnetic waves hit the FSS surface, it is reflected from the surface and bounces up

and down between the FSS and ground plane of the antenna inside the cavity. As small amounts of energy leak through the FSS, beamforming occurs. In this case, however, peak gain above the FSS will be reduced due to lateral energy leakage from the absence of cavity sidewalls and back radiation of the slot antenna. To reduce lateral energy leakage, the cavity is enclosed with metallic sidewalls and is referred to as enclosed cavity (S-EC) (Fig. 4.15(b)).

To suppress the back radiation from the slot, a cavity-backed slot is used to radiate energy uni-directionally. The antenna includes a reflector that is located 6.25 mm below the antenna. This height is $\lambda_o/4$ at 12 GHz (the source antenna design frequency) and chosen to make the reflected energy from the reflector and the source energy of the antenna in phase. This cavity consists of base and metallic sidewalls.

For cavity-backed slot with open cavity (CBS-OC) case, lateral leakage is expected to be similar to that of the slot with open cavity (S-OC). However, the gain is expected to be higher due to the additional energy presented to the FSS that results from the redirected back radiation of the slot. When the cavity-backed slot with enclosed cavity (CBS-EC) case is considered, the gain can be maximized due to the considerable reduction in leakage from both lateral and back radiation of the slot that increases the available energy to the FSS.

4.4.2. Fabrication

Details for the fabrication have been discussed in the section 3.4.2

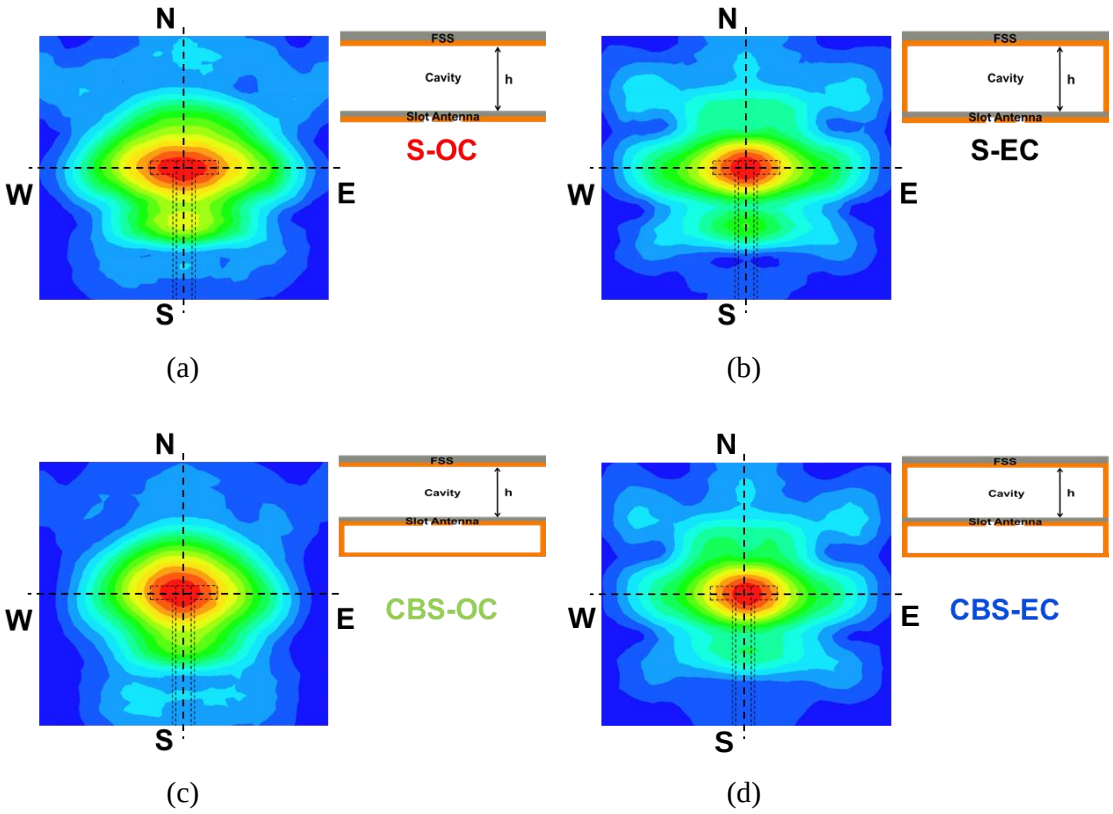

Fig. 4.16. 2D near-field distribution for each FPC system at 11.2 GHz above rectangular FSS array

4.4.3. Results

The 2D near-field behavior of each FPC system design is shown in Fig. 4.16. The near-field is observed at the frequency of 11.2 GHz at a reference plane located at 5 mm above the FSS. This frequency corresponds to the optimum beamforming obtained in the far-field. The feedline is localized along the S-N line and the slot is located in the center.

For slot with bi-directional radiation case, the field for the enclosed cavity (S-EC) is more focused around the slot than the open cavity (S-OC) and spreads more evenly above the FSS. It is due to the metallic sidewalls that prevents open cavity energy leakage

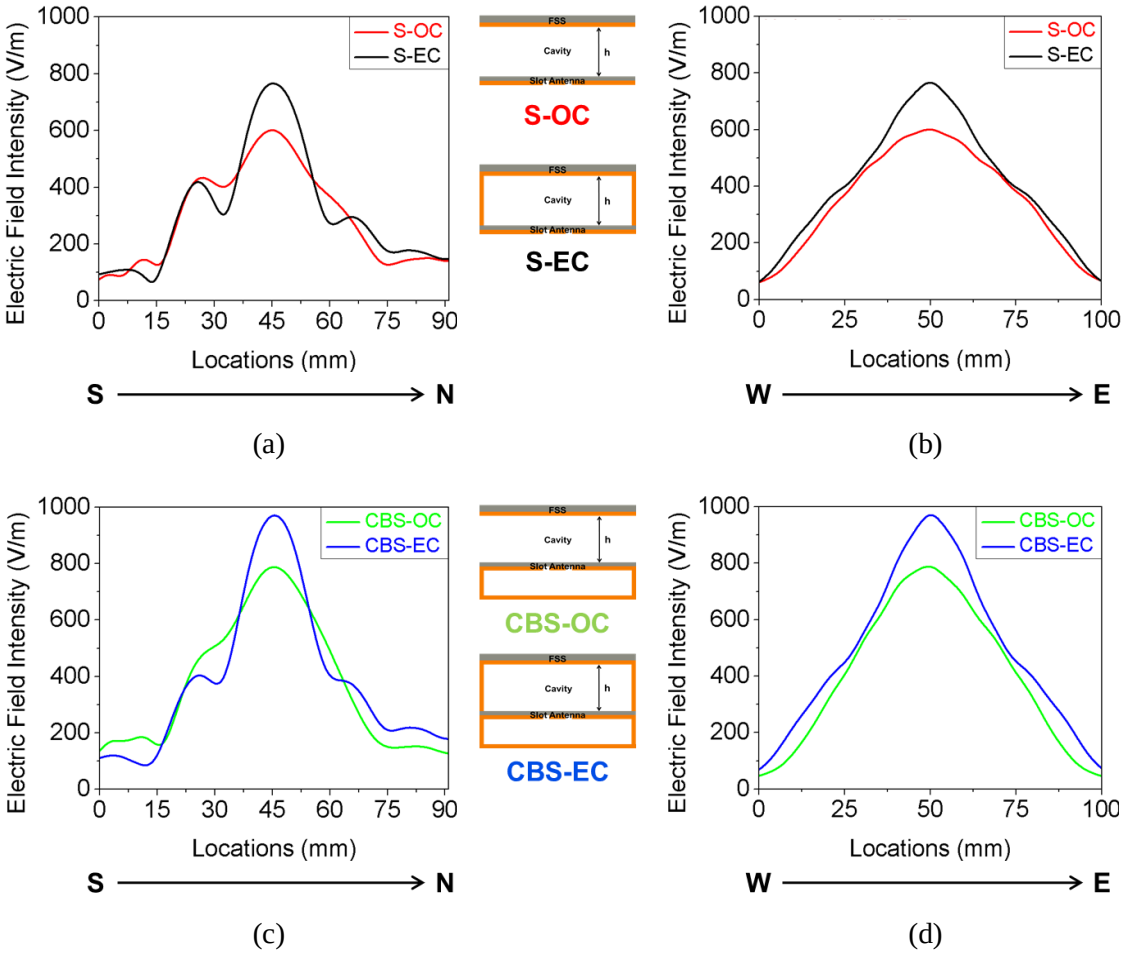

Fig. 4.17. 1D near-field distribution for each FPC system at 11.2 GHz above rectangular FSS array: (a)(c) E-plane cut (S-N) (b)(d) H-plane cut (W-E)

out of the cavity sides. The enclosed cavity (S-EC) with its metallic sidewalls stores energy captured inside the cavity then contributes to a more tapered and more center-concentrated distribution. The cavity-backed slot with uni-directional radiation case shows a similar trend where the open cavity (CBS-OC) forms an oval shape around the slot and the enclosed cavity (CBS-EC) spreads out more evenly.

The one dimensional near-field distribution of each FPC system design is shown in Fig. 4.17. The E-plane cut is along the S-N line and the H-plane cut along the W-E line

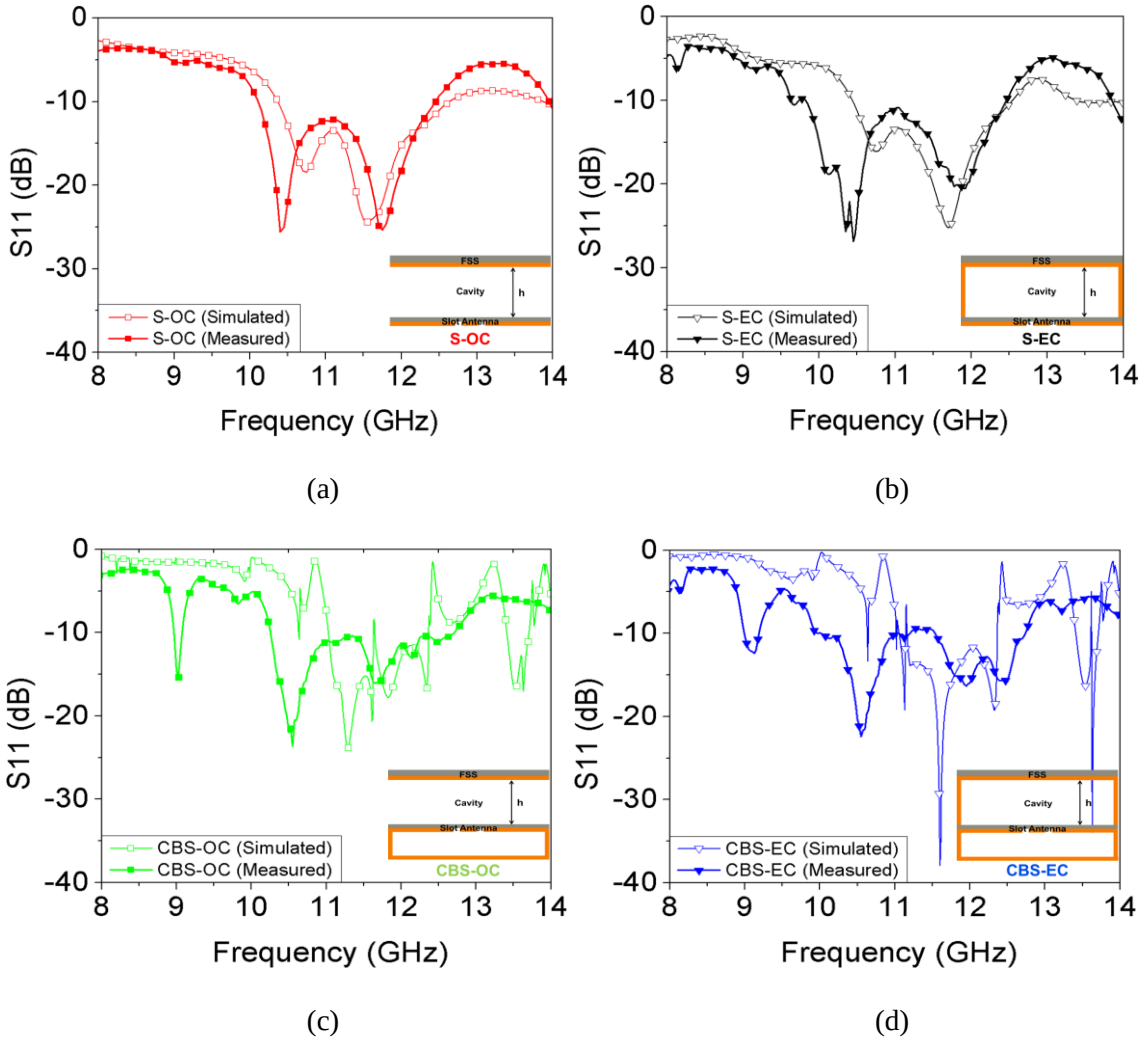

Fig. 4.18. Simulated and measured S11 (dB) vs. frequency (GHz)

as shown in Fig. 4.16. The E-plane cut distribution is asymmetric due to the presence of feedline. The enclosed cavity cases in Fig. 4.16(b) and (d) have more peak intensity due to the metallic sidewalls and more tapered distribution compared to the open cavity cases (a) and (c). For slot with bi-directional radiation case, the peak intensity is 600 V/m for the open cavity (S-OC) and increases by 166 V/m to 766 V/m for the enclosed cavity (S-EC). For cavity-backed slot with uni-directional radiation case, the peak intensity is 787

V/m for the open cavity (CBS-OC) and increases by 130 V/m to 971 V/m for the enclosed cavity (CBS-EC). The bi-directional slot radiation (S-OC and S-EC) case has more lateral energy leakage and back radiation to control due to lack of metallic sidewalls and reflector.

The simulated and measured reflection coefficient (S11) of the FPC antenna systems are shown in Fig. 4.18. The uni- or bi-directional radiation case has similar reflection response for the open and enclosed cavity. The slot with bi-directional radiation cases show better agreement between simulation and measurement compared to the cavity-backed slot with uni-directional radiation case. For slot antenna with open cavity (S-OC), the resonances occur at 10.75 GHz and 11.55 GHz in simulation and at 10.4 GHz and 11.75 GHz in measurement. For slot antenna with enclosed cavity (S-EC), the resonances occur at 10.78 GHz and 11.7 GHz in simulation and 10.35 GHz, 10.45 GHz and 11.85 GHz in measurement. For cavity-backed slot with uni-direction (CBS-OC and CBS-EC), the multiple resonances occur in broad band and measured 10 dB bandwidth (~ 50 %) is 10 % larger compared to the bi-directional radiation case (~ 40 %).

The optimum simulated patterns for each system is shown in Fig. 4.19. The optimum patterns in terms of the most directive main lobe and the least side and back lobes are determined to evaluate and analyze the far-field performance at the frequency of 11.2 GHz where the near-field is observed. The peak gain for the slot with the enclosed cavity (S-EC) increases by 0.82 dB (~ 20 %) while the back lobe as well as side lobe reduces due to decrease in lateral energy leakage compared to the open cavity (S-OC). The back lobe, however, is still observed significantly because the slot radiates bi-

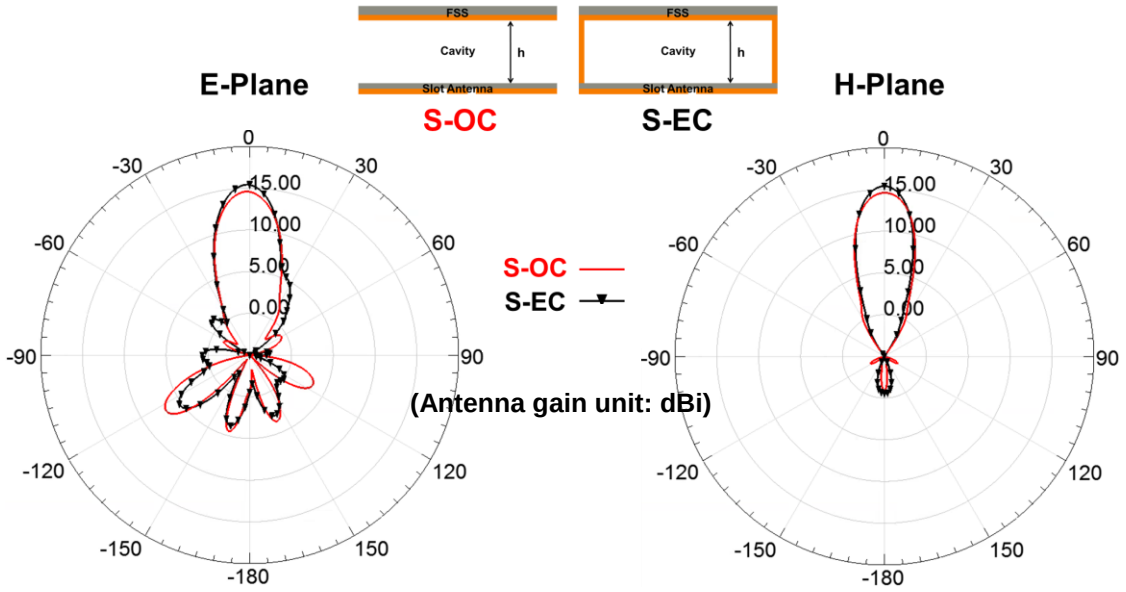

(a)

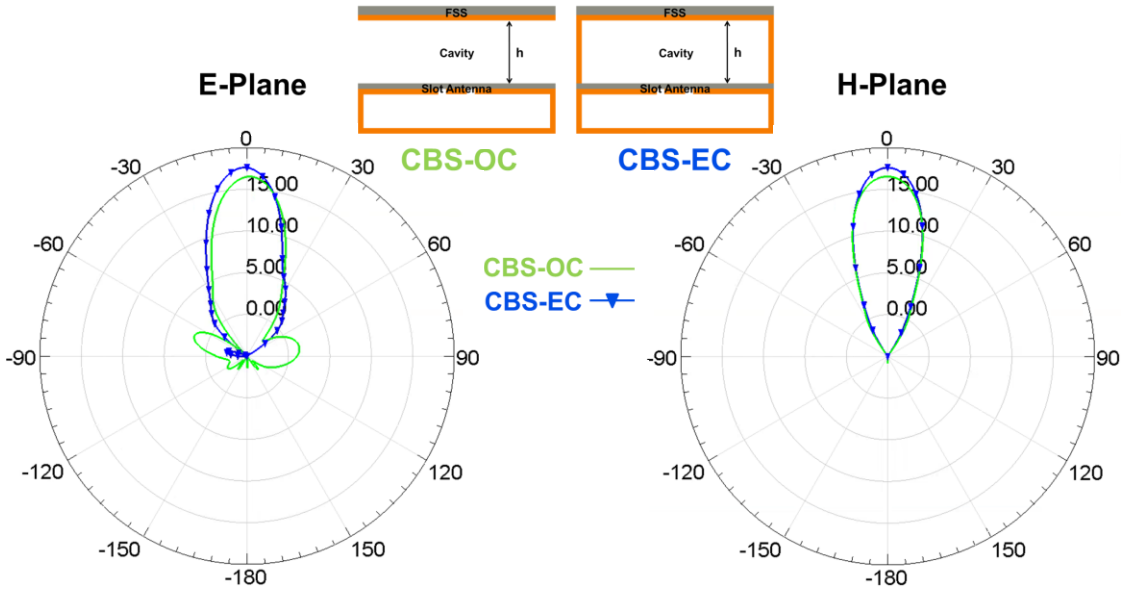

(b)

Fig. 4.19. Simulated radiation patterns for each FPC system at 11.2 GHz

directionally. The peak gain for the cavity-backed slot with enclosed cavity (CBS-EC) increases by 1.2 dB (~ 32 %) while the side lobe in E-plane for the enclosed cavity (CBS-

Table 4.2. Simulated pattern peak gains and beamwidth

	Peak gain (dBi)	Beamwidth (degree)
S-OC	14.6	25
S-EC	15.42	22
CBS-OC	16.5	23
CBS-EC	17.7	22

EC) reduces by 5 dB (~ 210 %) due to metallic sidewalls compared to the open cavity (CBS-OC). The cavity-backed slot antenna with enclosed cavity (CBS-EC) has the highest peak gain as expected. Also, since the cavity-backed slot has uni-directional radiation due to the reflector, the back lobe is considerably suppressed compared to the slot with bi-directional radiation.

The optimum measured patterns for each system is shown in Fig. 4.20. The optimum patterns in terms of the most directive main lobe and the least side and back lobes are obtained at 10.81 GHz. The frequency where the optimum patterns are observed is shifted compared to simulation. Also, the peak gain reduces while the beamwidth increases compared to simulation. It is probably due to fabrication tolerances such as uneven aperture size in rectangular FSS array and imperfectly flat cavity height.

The peak gain for the enclosed cavity (S-EC) increases by 0.3 dB (~ 7 %) while the back lobe as well as side lobe in E-plane is reduced compared to the open cavity (S-OC). The peak gain for the enclosed cavity (CBS-EC) increases by 1.4 dB (~ 38 %) compared to open cavity (CBS-OC). This variation is very close to the theoretical value, which is 1.2 dB (~ 32 %).

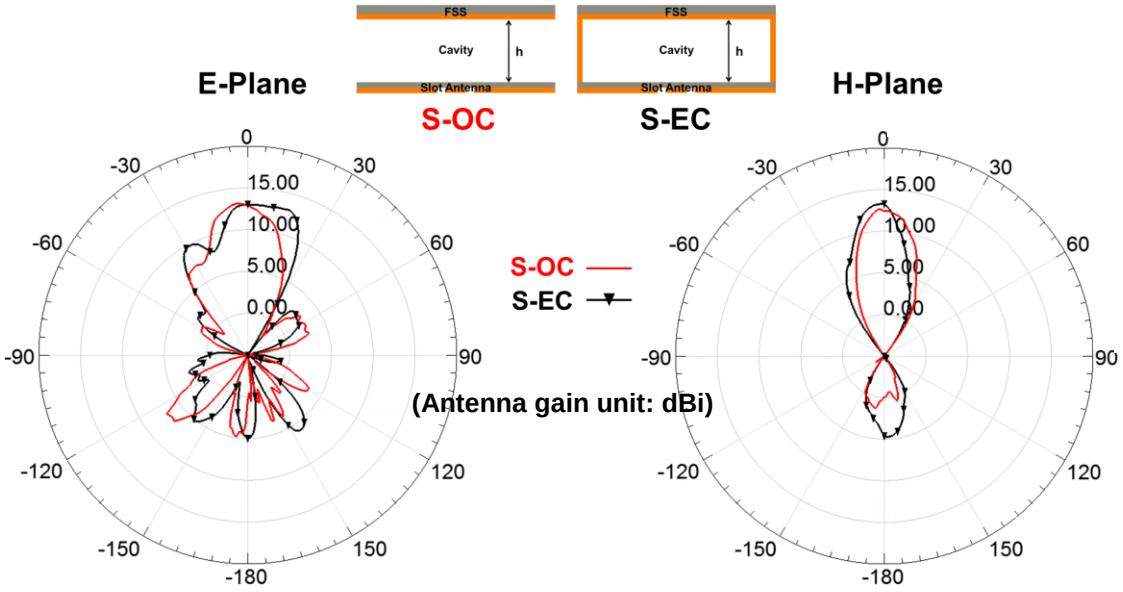

(a)

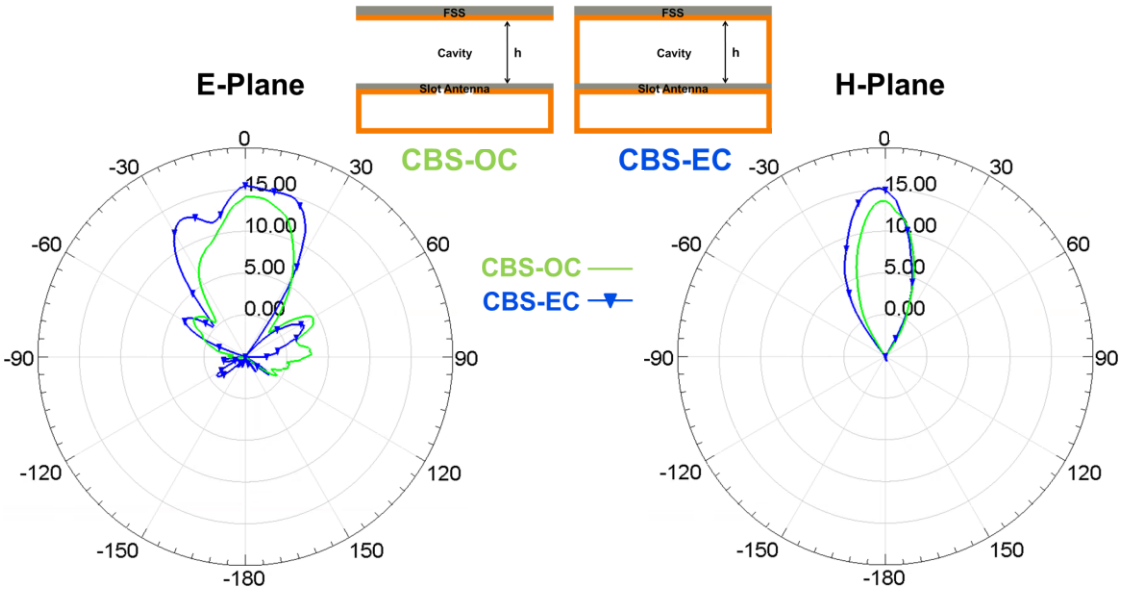

(b)

Fig. 4.20. Measured radiation patterns for each FPC system at 10.81 GHz

Table 4.3. Measured pattern peak gains in E- and H-plane

	E-plane (dBi)	H-plane (dBi)
S-OC	13.2	12.7
S-EC	13.5	13.0
CBS-OC	14.1	13.6
CBS-EC	15.5	15.2

4.5. Summary

In this chapter, FPC systems are characterized to investigate the FSS focusing effect on the feedline and system energy leakage effect on the system and improve the performance.

First, the use of a CPW feedline in the FPC system creates focusing beam above the feedline, and more asymmetric and tapered linear distribution in the near-field due to FSS beam focusing.

Second, the technique to orient one or more columns of an all horizontal set of apertures (FSS-AH) vertically over the feedline is proposed. This results in the largest energy reduction observed of ~ 45 dB and ~ 7 dB in the near- and far-field regions, respectively, for the FSS-3V structure relative to the peak feedline energy observed with the FSS-AH design only. As a result, FSS focusing effect from CPW feedline contribution is mitigated.

Lastly, the effects of leakage on FPC antenna system performance are studied using slot and cavity-backed slot antenna with rectangular FSS array. The enclosed cavity

due to metallic sidewalls prevents lateral energy leakage and results in 130 V/m of increased electric field in the near-field and 1.2 dB of increased gain in the far-field. The enclosed cavity, however, reduces the side and back lobe levels by 5 dB and 3 dB. In terms of reflection response, all systems achieve good impedance matching (|S11| < -12 dB) at the frequency where the optimum beamforming is obtained in the far-field. The cavity-backed slot with uni-directional radiation case has wider 10 dB bandwidth (~ 50 %) than the slot with bi-directional radiation case (~ 40 %). This study offers the design flexibility, near-field and far-field analysis in array antenna systems and 3-D packaging applications.

CHAPTER 5

Reconfigurable FPC Antenna Systems

5.1. Introduction

The need to manipulate and control RF systems in wireless communication and biomedical applications has been growing. As a result, reconfigurable wireless RF platforms are being developed and advanced to address this need.

Microfluidic technologies are one of the attractive and feasible solutions for reconfigurable capability and many research groups have explored the use of dielectric fluid and/or liquid metal for this purpose. For example, integrated microfluidic channel is used for cooling of high power passive and active devices on multilayer organic liquid crystal polymer (LCP) substrate by circulating fluid [42-43]. Introducing fluids provides the frequency tuning in the coplanar waveguide-fed annular slot antenna by dynamically changing the resonant frequencies [44-45]. The directivity of the microstrip directional coupler is improved by a microfluidic superstrate in the coupling gap [46] and microstrip ring filter leverages the degenerate mode by placing the DI water on a stub of the ring [47]. Liquid metal also has been widely used in antenna systems. By adjusting the lengths of parasitic elements via pressure-driven flow of liquid metal, for instance, Yagi-Uda monopole array antenna is tuned over wider frequency range [48]. The use of reactive loading effect of a liquid metal on top of each slot antenna offers the frequency tuning in dual-band slot antenna [49]. Dual-band patch antenna is fluidically tuned by placing two

oil-filled channels in the substrate of the antenna along the nonradiating edges of the patch and moving metal cylinder [50].

Only recently FSS and fluids have been explored. Four-arm Archimedean spiral FSS is tuned in bandpass and bandstop band by adding a PDMS bonding layer and fluidic channel layer above the FSS [51]. The use of pressure-driven flow in a T-junction to adjust the amount of mercury and mineral oil provides the tuning with wider fractional bandwidth for FSS array consisting of periodically spaced polytetrafluoroethylene (PTFE) [52]. The transmission phase of circularly polarized transmitarray unit cell based on ring-split ring is fluidically tuned by injecting liquid metal into the gap in the PDMS channel [53]. Large scale fluidic tuning of 2D high impedance subwavelength periodic structure is achieved by moving the periodic train of balls over small distances with respect to the fixed periodic structure [54]. A 2D perturbed FSS integrates the microfluidic capillary on an FSS element in a waveguide structure to enhance the spectral shift of the odd resonance for microwave sensing applications [55].

As discussed in the previous sections, an FPC antenna system has the advantage of replacing complex feedline network with a single source and FSS to synthesize the behavior of the array antenna systems. Since FSS dominates the performance of the FPC antenna system, it is required to augment or modify the FSS structure for reconfigurable system. Due to complex design of FSS structure, however, it is challenging to modify the FSS structure. So, to control and improve the performance of the FPC antenna system, it is desirable to reconfigure the FPC system without modifying the uniform FSS design.

In this chapter, a microfluidic channel is integrated into the FPC antenna system

and the channel is filled with air and deionized (DI) water. The fluidic channels are placed on top of the slot antenna in the FPC system and the effect of fluidic volume on tuning and switching capability is investigated. Also, a microfluidic housing is attached to the uniform FSS design to synthesize the behavior of the augmented FSS structure. This leads to near-field beam-splitting with a novel technique and it can provide the potential to chip to chip communication and biomedical imaging.

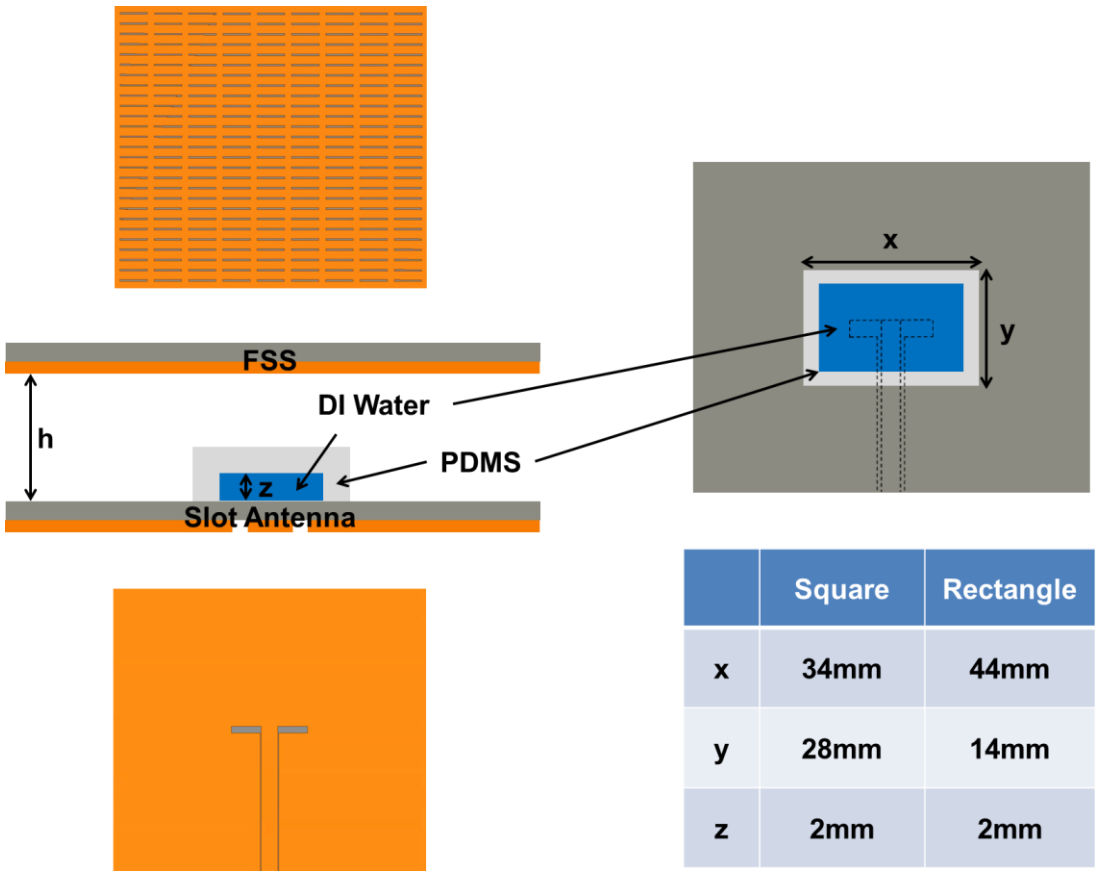

	Square	Rectangle
x	34mm	44mm
y	28mm	14mm
z	2mm	2mm

(a) (b)

Fig. 5.1. Structure of FPC antenna system with microfluidic channel: (a) side view (b) top view and channel dimension (right)

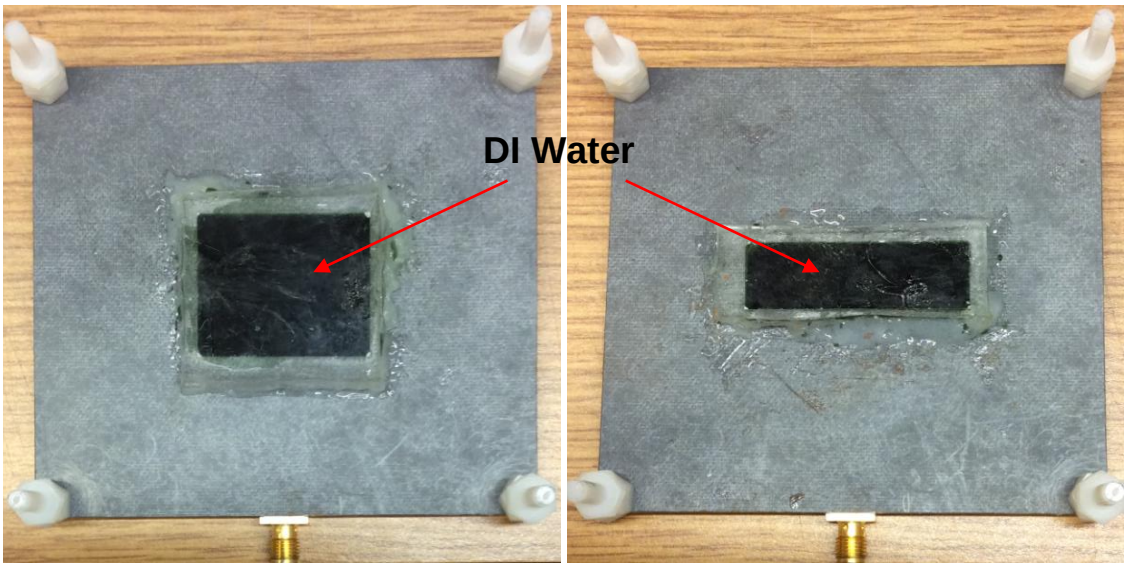

(a) (b)

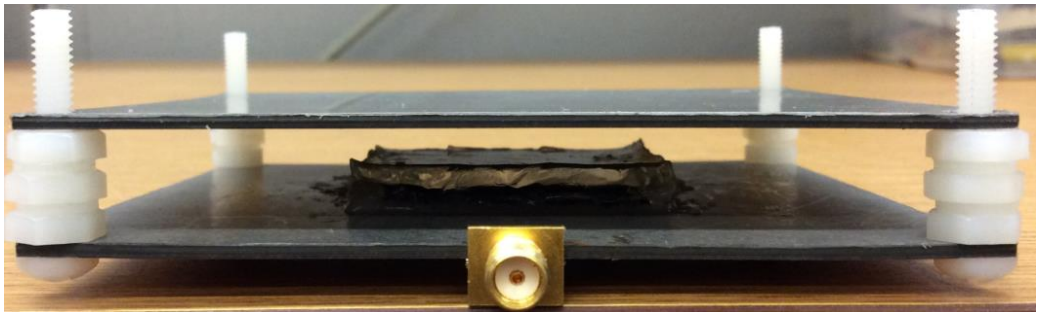

(c)

Fig. 5.2. Picture of the FPC antenna system with DI water-filled microfluidic channel: (a) square channel (b) rectangular channel (c) side view of the FPC system

5.2. Fluidic Switching and Tuning

5.2.1. Design

The FPC antenna system with the integrated microfluidic channel is shown in Fig. 5.1 [56]. The slot antenna and FSS are designed as discussed in the section 2.3. The FSS consists of 9 by 27 rectangular unit cells. A fluidic housing is created using

polydimethylsilone (PDMS) and is attached to the backside of the slot antenna to absorb the radiated energy from the slot antenna for switching and to achieve tuning that results from dielectric loading. The fluidic housing is filled with air or deionized (DI) water. DI water is used as a fluid because it has high dielectric constant (ε_r = 81) and high resistivity (ρ = 18 MΩ·cm). To investigate the effect of fluidic volume on tuning and switching capability in FPC antenna systems, two fluidic channels are considered: square (34 mm × 28 mm × 2 mm) and rectangle (44 mm × 14 mm × 2 mm). The dimension of the channels is empirically determined for this study.

5.2.2. Fabrication

Fabricated FPC system with integrated microfluidic channel is shown in Fig. 5.2. A glass mold is designed and made to create the desired fluidic channels. The PDMS mixture (Dow Corning Sylgard 184 and silicone hardener) is poured onto the mold and heated up to 700 ˚C for 4 hours to make PDMS harden. The PDMS channel is removed from the mold and attached to the Duroid5880 (ε_r = 2.2, substrate height = 1.57 mm, metal thickness = 35 μm, tan δ = 0.0009) using PDMS adhesive (Dow Corning SE 9186).

5.2.3. Results

The measured reflection response (S11) for three cases is shown in Fig. 5.3. For air case, the resonance occurs at 10.4 GHz and 11.75 GHz with good matching (< -25 dB). When DI water is injected into rectangular channel, the second resonance shifts from 11.75 GHz to 11.3 GHz (3.8 %) while the first resonance gets weaker with high reflection coefficient relative to air case. For square channel case, however, the first resonance

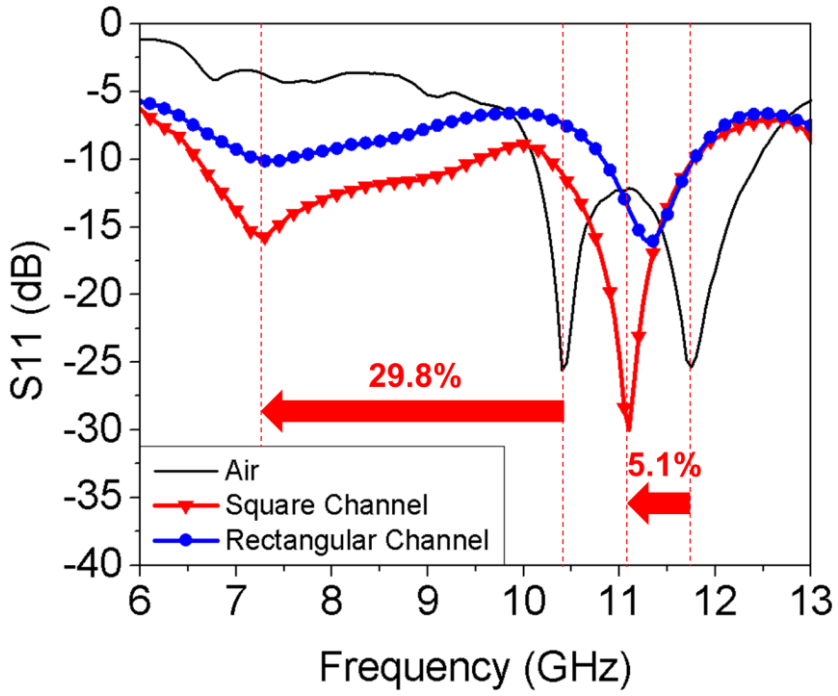

Fig. 5.3. Measured S11 (dB) vs. frequency (GHz)

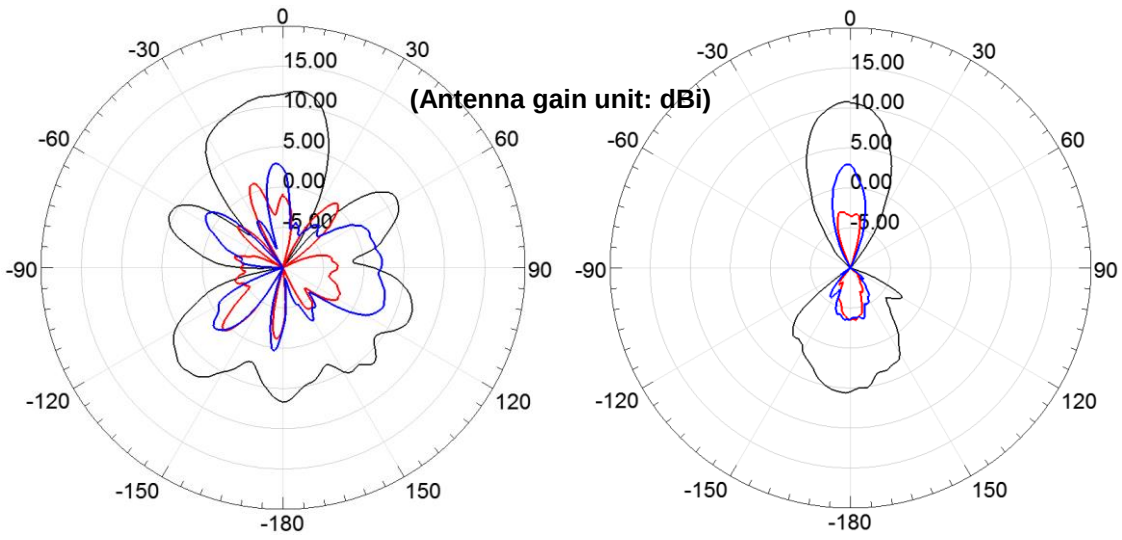

(a) (b)

Fig. 5.4. Measured far-field radiation patterns for FPC system with air (black) or square channel (red) and rectangular channel (blue): (a) E-plane (b) H-plane

shifts from 10.4 GHz to 7.3 GHz (29.8 %) and the second resonance shifts from 11.75

GHz to 11.15 GHz (5.1 %) compared to air case. The resonant frequencies for DI water-filled fluidic channel are shifted down because highly dielectric and resistive fluid increases capacitance in the FPC system.

The measured far-field radiation patterns for three cases at 10.4 GHz are shown in Fig. 5.4. For air case, the E- and H-plane gains are 11.98 dBi and 10.72 dBi, respectively. For square channel, the E- and H-plane gains are 0.94 dBi and -2.9 dBi. For rectangular channel, the E- and H-plane gains are 2.98 dBi and 2.89 dBi. It demonstrates that the larger fluidic volume suppresses more radiated energy due to higher absorption of fluid. Also, it is observed that the volume of square channel is ~ 55 % larger than that of rectangular one leading to ~ 40 % reduction of the E-plan peak gain.

5.3. Near-Field Beam-Splitting FSS

5.3.1. Design

As discussed in the section 4.3, it is demonstrated that the FSS augmentations with vertically oriented unit cells (FSS-1V and FSS-3V) suppress near- and far-field feedline behavior efficiently in FPC transmission line systems. In this section, the FSS augmentations – FSS-1V and FSS-3V – are integrated into the FPC antenna systems with a source of slot or patch antenna to evaluate the beam-splitting capability [57-58]. The slot and patch antenna are designed as discussed in the section 3.5. The cavity height is 10.81 mm and the virtual reference plane (VRP) for electric field observation is designed and located 5 mm above FSS in simulation.

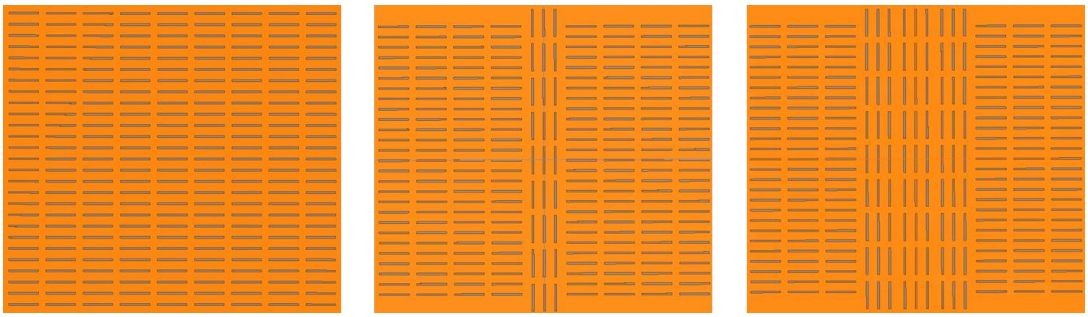

(a)

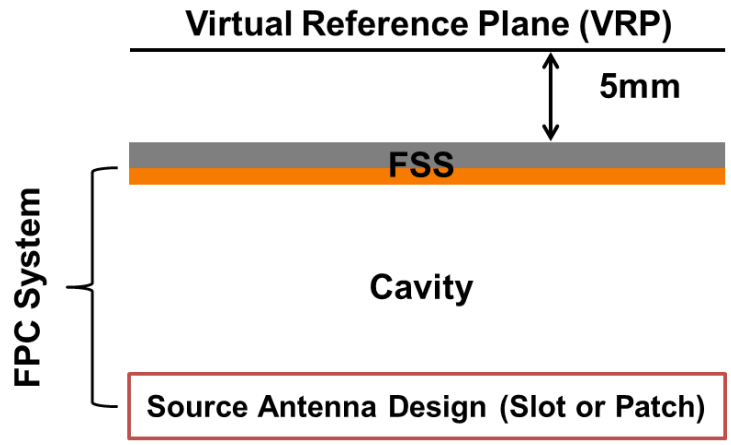

(b)

(c)

Fig. 5.5. FPC antenna system with three FSS and two source antennas: (a) top view of the FSS arrays (b) side view of the FPC system (c) top view of the slot (left) and patch (right) antennas

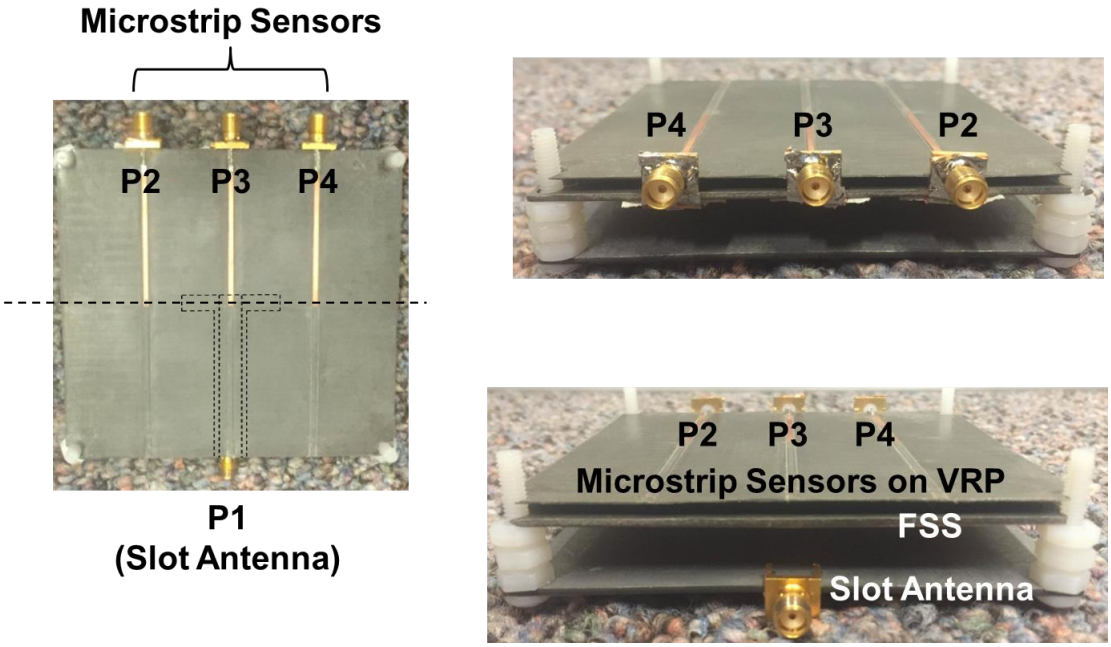

(a) (b)

Fig. 5.6. Picture of the FPC system with the microstrip sensors: (a) top view (b) side view

5.3.2. Fabrication

The test circuit with the sensor is shown in Fig. 5.6. All antenna and FSS structures are printed on Duroid5880 (ε_r = 2.2, substrate height = 1.57 mm, metal thickness = 35 μm, tan δ = 0.0009). To detect energy above FSS in measurement, a microstrip open stub sensor is designed and fabricated on Duroid5880 (ε_r = 2.2, substrate height = 0.508 mm, metal thickness = 17.5 μm). The sensor is located 5 mm above FSS to replicate the VRP for detection and assembled with FPC antenna system using nylon screw, nuts and flat washer. Each microstrip has a width of 1.57 mm and length of 45 mm and is separated by a center to center spacing of 25 mm. The edge of the stub resides in the center line of the board as shown in Fig. 5.6(a). Port 1 from the network analyzer is connected to a source

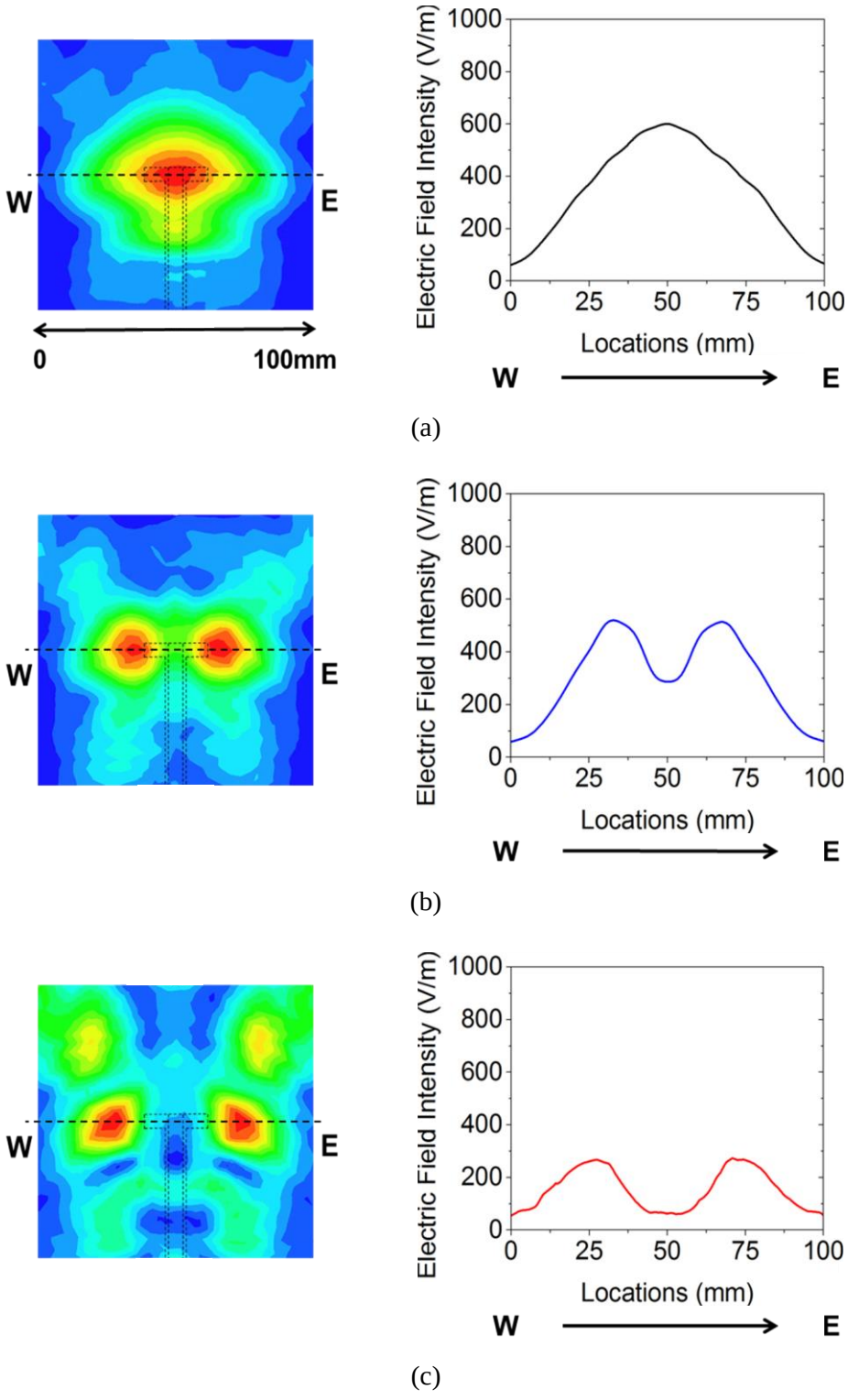

Fig. 5.7. 2D near-field distribution for FPC system with slot antenna above each FSS (left) and 1D electric field intensity along the W-E line (right): (a) FSS-AH (b) FSS-1V (c) FSS-3V

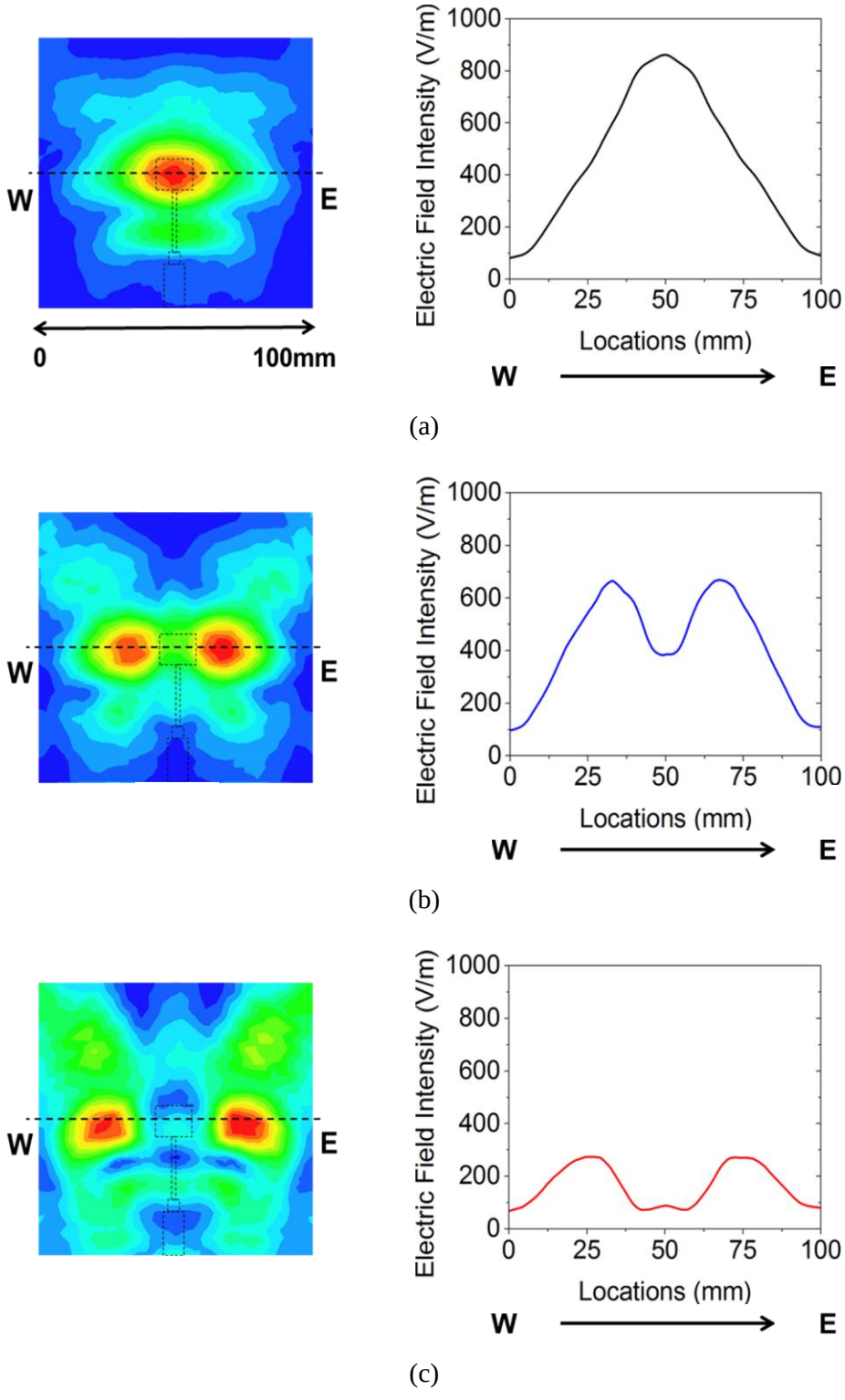

Fig. 5.8. 2D near-field distribution for FPC system with patch antenna above each FSS (left) and 1D electric field intensity along the W-E line (right): (a) FSS-AH (b) FSS-1V (c) FSS-3V

antenna located at P1 of the FPC antenna system as input. Port 2 from the network analyzer is connected to the n^{th} port of the sensor as the output while the other ports of the sensor are terminated with 50 Ω load. Copper tape is used to connect the SMA connector of each stub to the FSS that behaves as a slotted ground plane.

5.3.3. Results

The near-field distribution of FPC antenna system with slot or patch for each FSS at 11.2 GHz is shown in Fig. 5.7 and Fig. 5.8, respectively. For FSS-AH design, the patch shown in Fig. 5.8(a) has most tapered distribution along the W-E line with the strongest field intensity (862 V/m) compared to the slot (601 V/m) shown in Fig. 5.7(a). The highest field intensity with the patch is due to the unidirectional radiation of the patch and beam focusing of FSS-AH compared to the bidirectional radiation of the slot into the cavity region of the FPC system and the air region below the slot.

When the vertical columns are included above the source and feedline, they reduce significantly the leakage of the radiated energy from the source and line through the FSS. This vertical region behaves as a reflector in the cavity which reflects a stronger source signal into the cavity. The resulting effect is that the main beam located over the source is split approximately equally in the W-E direction, which is orthogonal to the vertically oriented unit cells. For the FSS-1V design, the two split beams for slot and patch, have the peak intensity of 520 V/m and 665 V/m, respectively. Their respective center locations for the slot and patch are 16 mm and 17 mm from the center of the source antenna, respectively. The minimum field intensity between the two split beams for slot

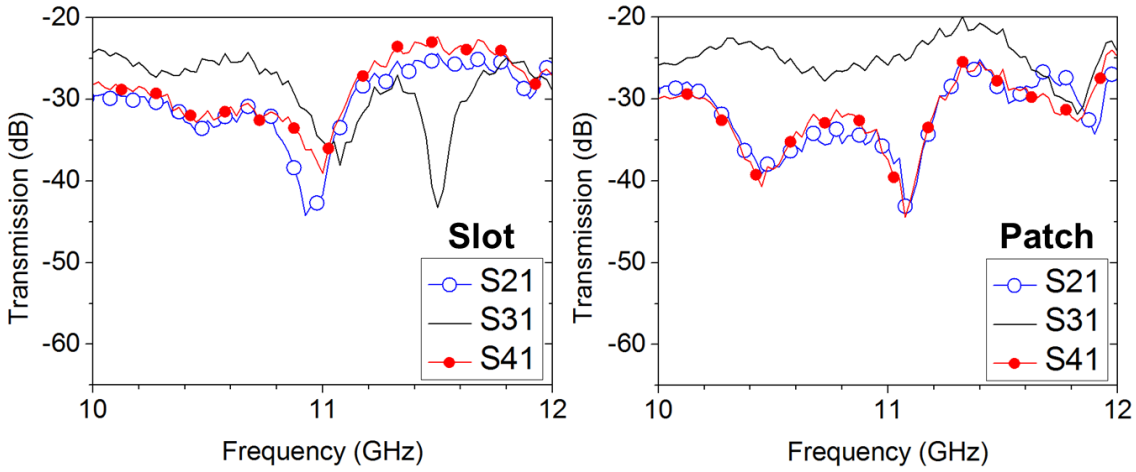

(a) FSS-AH

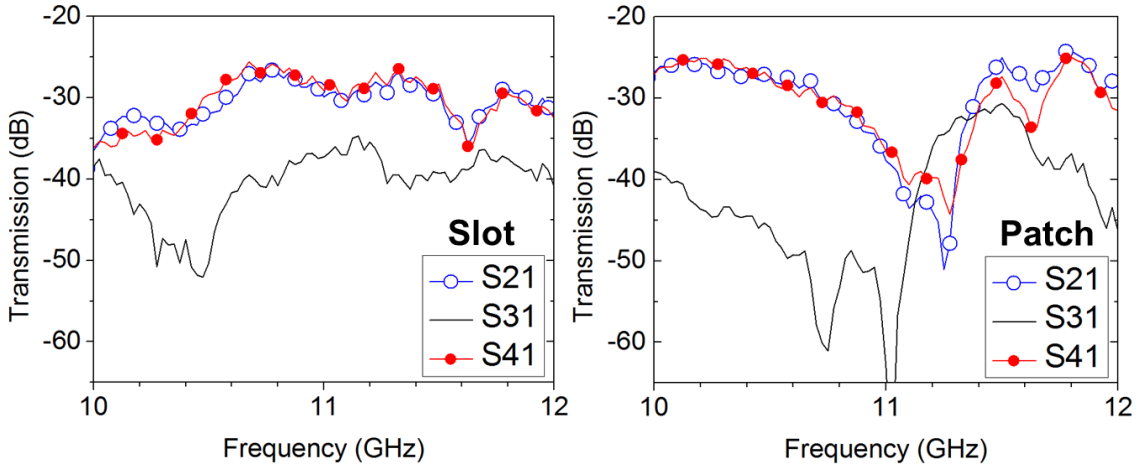

(b) FSS-3V

Fig. 5.9. Measured S-parameters (dB) vs. frequency (GHz): FPC antenna system with slot (left) or patch (right) antenna

and patch is 286 V/m and 383 V/m, respectively. For FSS-3V design, the split beam separation increases to 43 mm for slot and 49 mm for patch and the field intensity decreases to 273 V/m for slot and 271 V/m for patch. Orientation of split beams is no longer symmetric along the W-E line and instead the beam is distributed along an arc angle with respect to the antenna center. Increasing the number of the vertical sets results

in split beams with lower intensity because the additional vertical sets prevent the source radiation from leaking through the FSS. Also, it causes energy redistribution above the horizontal unit cell region that creates two split beams on each side.

The measured S-parameter response for FSS-AH and FSS-3V cases is shown in Fig. 5.9. Port 3 (P3) represents the stub sensor line located in the center of the slot or patch. Port 2 and 4 (P2 and P4) represent the sensor lines 25 mm away from the center, located above the horizontal column region of the FSS. All S-parameters are evaluated to observe the detected energy on the sensor. S21 and S41 are expected to produce similar response due to FSS symmetry. For FSS-AH case, it is shown that the detected signal (S31) over the slot or patch has a higher field intensity compared to the field strength locations at P2 (S21) and P4 (S41). The patch, however, has the largest field intensity difference and it is consistent with the tapered field distribution for the patch compared to the distribution for the slot. In Fig. 5.9(a), the patch signal level for at P2 (S21) and at P3 (S31) is -35 dB and -25 dB at 10.85 GHz whereas for the slot signal level is -32 dB and -27 dB at 10.81 GHz, respectively. For FSS-3V case, the beam is split, therefore, P3 signal (S31) is much lower than the P2 (S21) and P4 (S41) over a broader frequency compared to the FSS-AH design. The maximum beam-splitting occurs for the slot (20 dB) at 10.5 GHz and for the patch (40 dB) at 11 GHz as shown in Fig. 5.9(b).

The simulated far-field radiation patterns are shown in Fig. 5.10. The asymmetric pattern in the E-plane is due to the presence of feedline. For the FSS-1V design, one vertical column decreases the radiation leakage through the FSS. As a result, the peak gain reduces while back lobe increases for the slot and side lobe increases for the patch. For

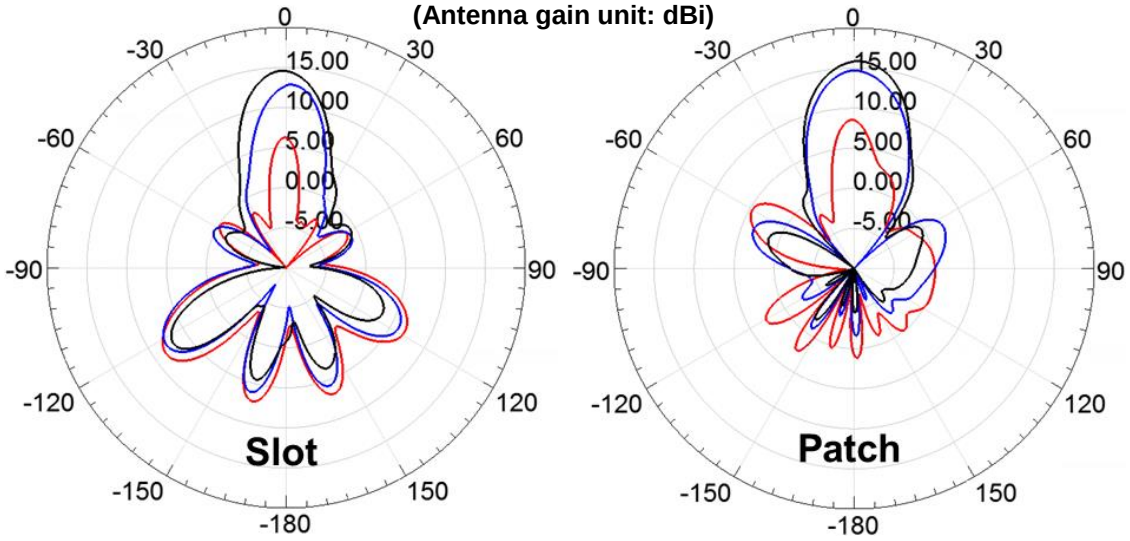

(a) E-plane

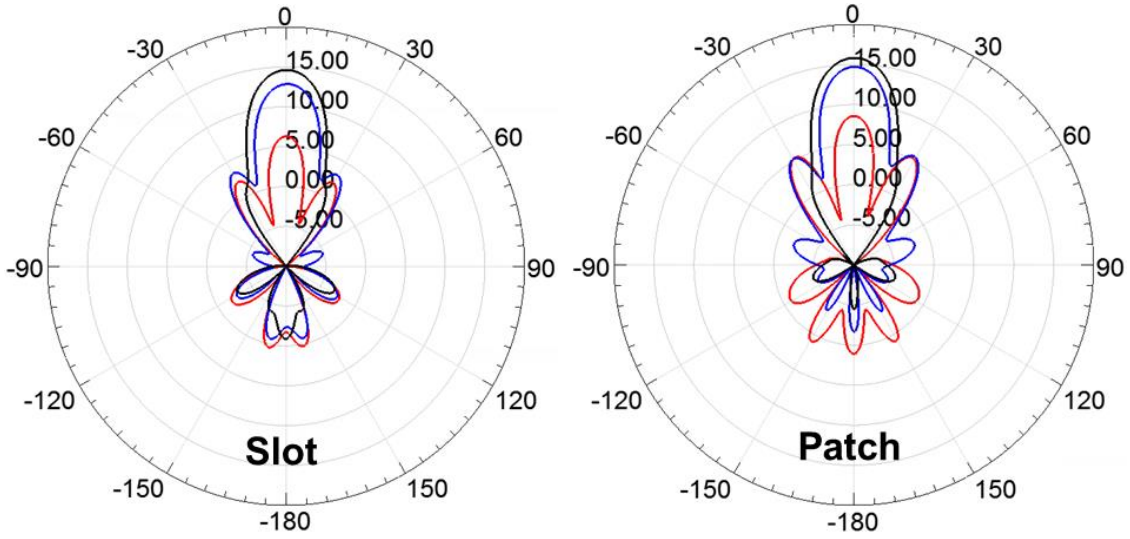

(b) H-plane

Fig. 5.10. Simulated far-field radiation patterns: FPC antenna system with slot (left) or patch (right) antenna: FSS-AH (**black**), FSS-1V (**blue**) and FSS-3V (**red**)

the FSS-3V design, the peak gain decreases significantly and the slot has more back radiation and the patch has more side lobe. It implies more energy is reflected back from vertical sets on the FSS surface to cavity and it radiates out of the cavity sides and the

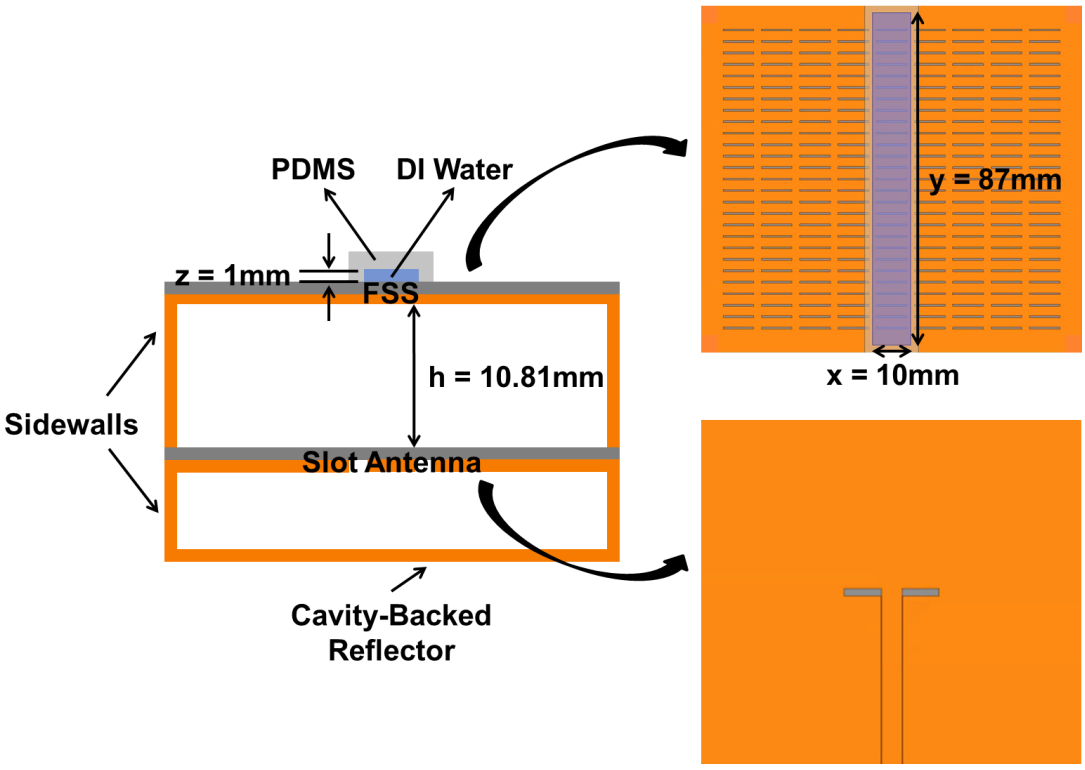

Fig. 5.11. Cavity-backed FPC antenna system with PDMS fluidic channel on FSS-AH: cross-section view (left) and top view (right)

back of the antenna.

5.4. Reconfigurable FSS

5.4.1. Design

This section studies the use of microfluidics to alter an FSS structure to achieve beam-focusing or beam-splitting in the near-field [59]. To investigate the reconfigurable capability of the FPC system, an enclosed cavity-backed FPC antenna system without or with a microfluidic housing is considered as shown in Fig. 5.11. The slot antenna is used

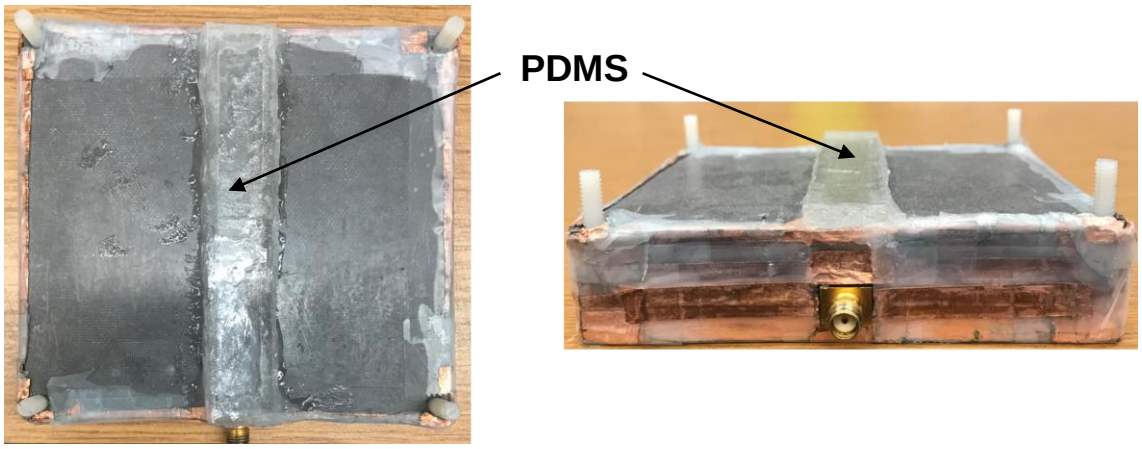

Fig. 5.12. Picture of the cavity-backed FPC antenna system with PDMS fluidic channel on FSS-AH. The channel is filled with air or DI water: top view (left) and side view (right)

as a source to excite the FPC system with a fluidic channel. The FSS array has 9 by 27 horizontally oriented unit cells (FSS-AH). More details for the slot and FSS designs have been discussed in the section 2.3. The microfluidic channel is made of polydimethylsilone (PDMS) and localized along the feedline in the center of the FSS-AH array. The volume of fluid (x × y × z) is 10 × 87 × 1 mm^3. The width of the fluid (x) is equal to the FSS unit cell width of 10 mm. The fluidic channel is filled with air or DI water. To prevent energy leakage around the FPC system, metallic sidewalls and reflector enclose cavity region and region below the slot. Three systems are considered in this study: (1) no PDMS (2) air inside PDMS and (3) fluid inside PDMS.

5.4.2. Fabrication

The cavity-backed FPC antenna system with PDMS fluidic channel on FSS-AH is shown in Fig. 5.12. All designs are fabricated on Duroid5880 (ε_r = 2.2, substrate height = 1.57 mm, metal thickness = 35 μm, tan δ = 0.0009). To build metallic sidewalls and reflector, hard boards are cut and copper tape is attached to the boards. These boards are

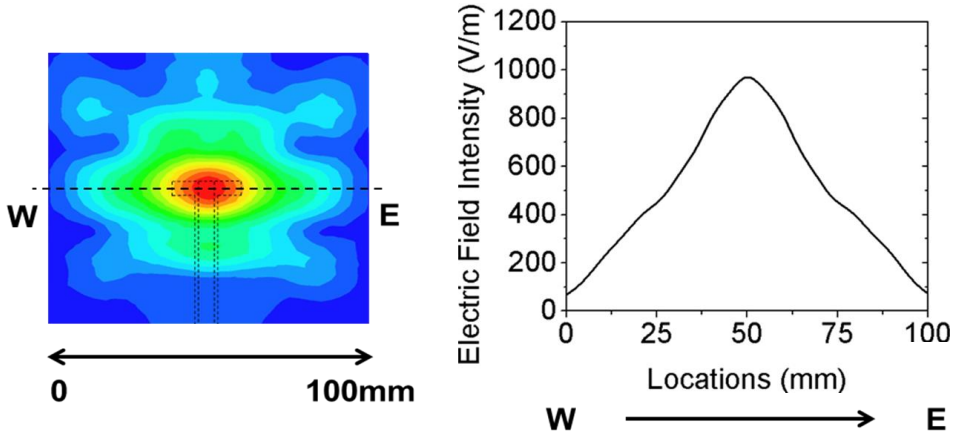

(a)

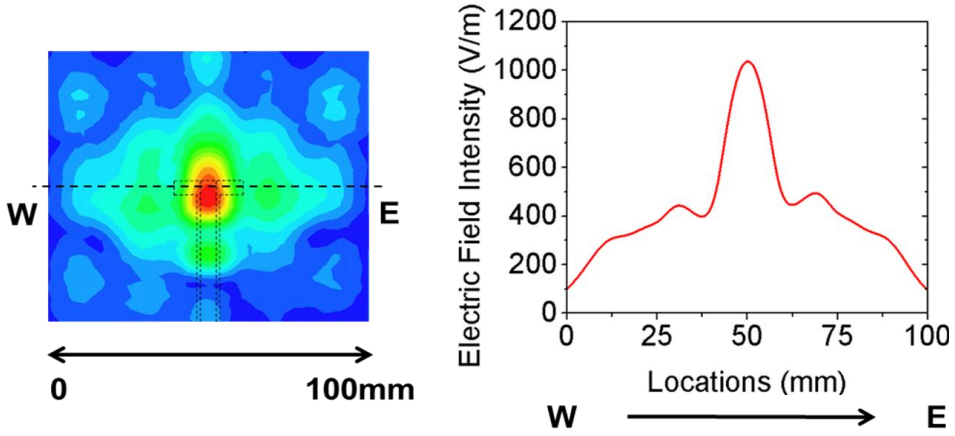

(b)

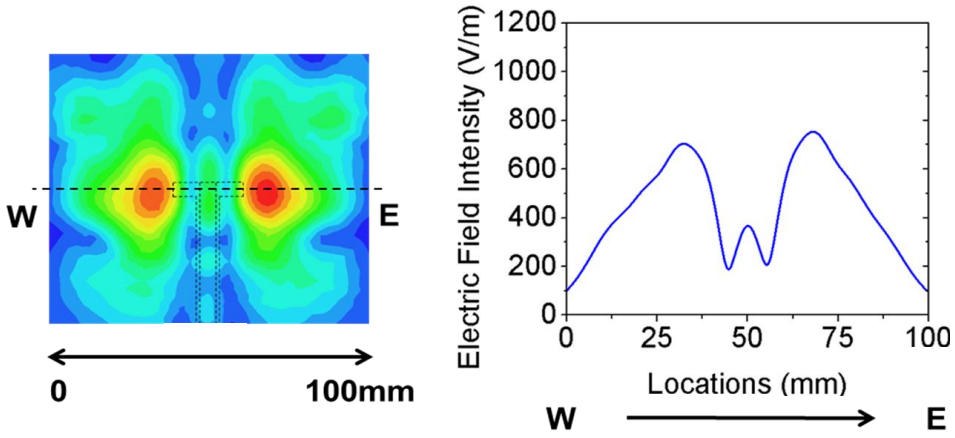

(c)

Fig. 5.13. 2D near-field distribution above FSS (left) and 1D electric field intensity along the W-E line (right): (a) **no PDMS** (b) **air inside PDMS** (c) **fluid inside PDMS**

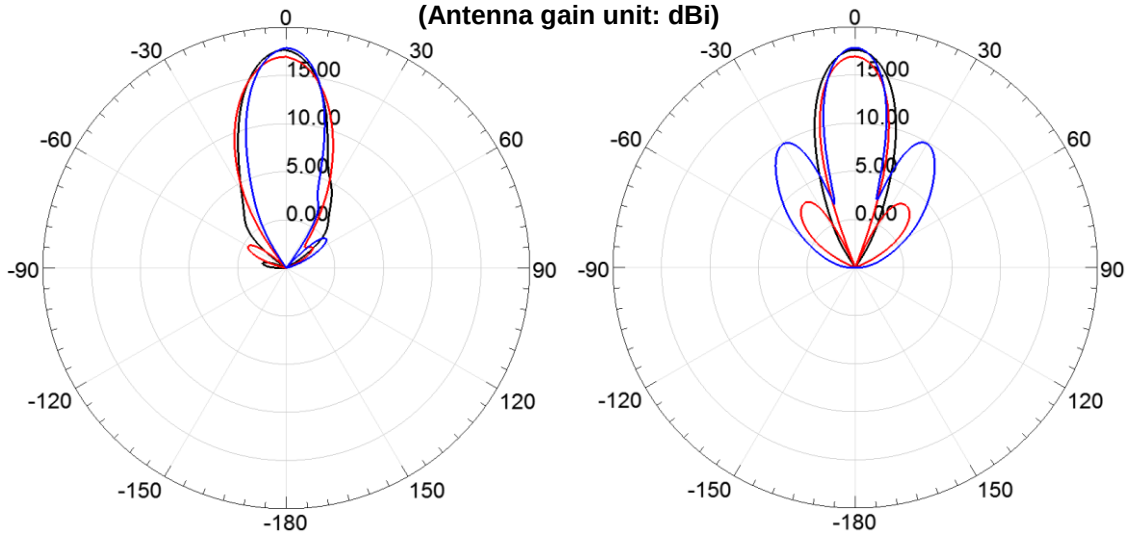

(a) (b)

Fig. 5.14. Simulated far-field radiation patterns for FPC antenna system with no PDMS (**black**), air inside PDMS (**red**) and fluid inside PDMS (**blue**) at 11.2 GHz

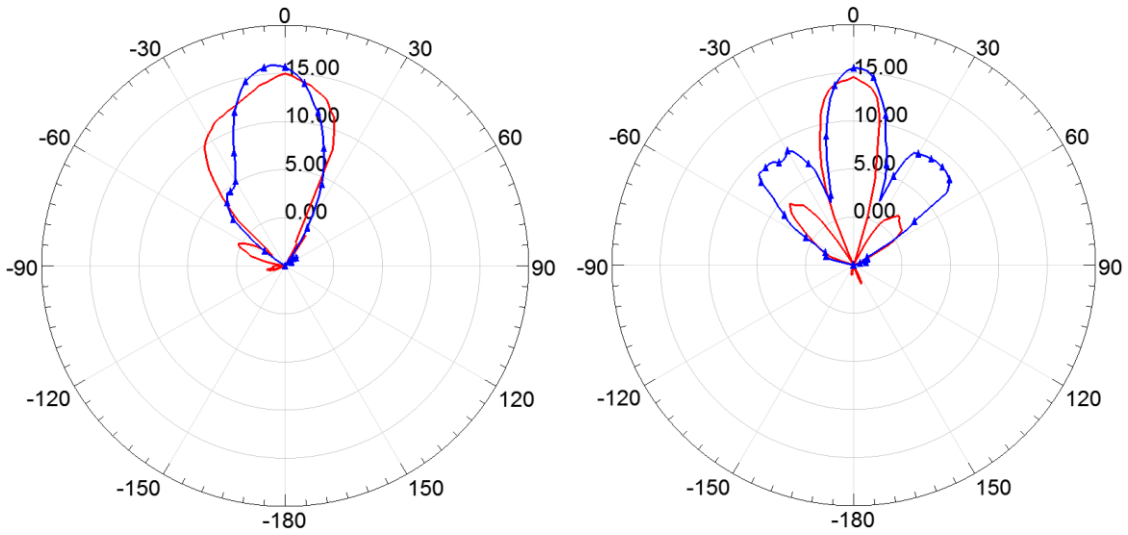

(a) (b)

Fig. 5.15. Measured far-field radiation patterns for FPC antenna system with air inside PDMS (**red**) and fluid inside PDMS (**blue**) at 10.81 GHz

combined with open cavity FPC antenna system. The PDMS channel is created and attached on top of the FSS-AH. The fluid is injected into the channel using syringe.

5.4.3. Results

The near-field distribution 5 mm above FSS for each case at 11.2 GHz is shown in Fig. 5.13. For no PDMS in Fig. 5.13(a), the field is focused around the center of the slot antenna and the field spreads out in all directions and diminishes as it propagates farther away from the center. The peak field intensity is 971 V/m and the percentage of distance that exceeds half of peak intensity (P) is 45.5 % (45.5 mm/100 mm). For air inside PDMS in Fig. 5.13(b), the field is formed more strongly around the center of the system and the field distribution is much more tapered compared to no PDMS case. The peak field intensity increases by 66 V/m (~ 7 %) to 1037 V/m and the percentage of distance (P) reduces to 17.5 %. This beam narrowing is achieved because the air-filled PDMS (ε_r ~ 2.7) channel makes energy leakage through FSS focusing that results from the refractive index difference between air and PDMS. It demonstrates that the air-filled PDMS housing can be used as an additional lens for post-FSS beam focusing. When filled with DI water inside PDMS, the main beam splits along the W-E line and is placed around the edge of the slot antenna. The peak field intensity of split beams is 753 V/m and the null between split beams is 189 V/m. As highly resistive DI water absorbs energy from the source, the fluid significantly suppresses near-field beam in the region above the slot antenna and feedline thus resulting in beam-splitting. It shows that the DI water-filled fluidic channel acts as a near-field beam-splitter.

The simulated and measured far-field radiation patterns for each case are shown in Fig. 5.14 and Fig. 5.15, respectively. For no PDMS case, the peak gain is 17.7 dBi and the pattern is highly directive due to FSS beam focusing. For air inside PDMS, the peak

gain reduces slightly to 16.93 dBi and side lobe level in H-plane increases up to ~ 3 dB. For lossy fluid inside PDMS, the peak gain increases by ~ 1 dB to 17.83 dBi compared to no PDMS case. Also, higher side lobe levels in H-plane are observed due to two split beams along the W-E line in the near-field that result from high absorption of DI water.

5.5. Microfluidic Near-Field Beam-Splitting FSS

5.5.1. Design

It has been demonstrated that a near-field beam is split for FPC antenna system with a slot antenna and augmented FSS array (FSS-1V) in the section 5.3. This design approach, however, requires modification of the uniform FSS design with horizontally oriented unit cells (FSS-AH). In this section, a microfluidic channel is introduced into the FPC antenna system without altering the FSS structure for near-field beam-splitting [60]. Also, the effect of microfluidic volume on an FSS is investigated compared to a fixed FSS design. The cavity-backed FPC antenna system with augmented FSS (FSS-1V) and microfluidic FSS are shown in Fig. 5.16. The augmented FSS array (FSS-1V) has vertically oriented unit cells along the center of the FSS surface and horizontally oriented unit cells in other regions. The microfluidic FSS array (FSS-AH w/ fluidic channel) has all horizontally oriented unit cells on one surface with a microfluidic channel which is localized along the center on the other. Two fluidic volume (x × y × z) are considered in this study: (1) $8 \times 87 \times 1$ mm^3 (narrow channel) (2) $10 \times 87 \times 1$ mm^3 (wide channel). The separation between FSS and slot antenna layer (h) is 10.81 mm.

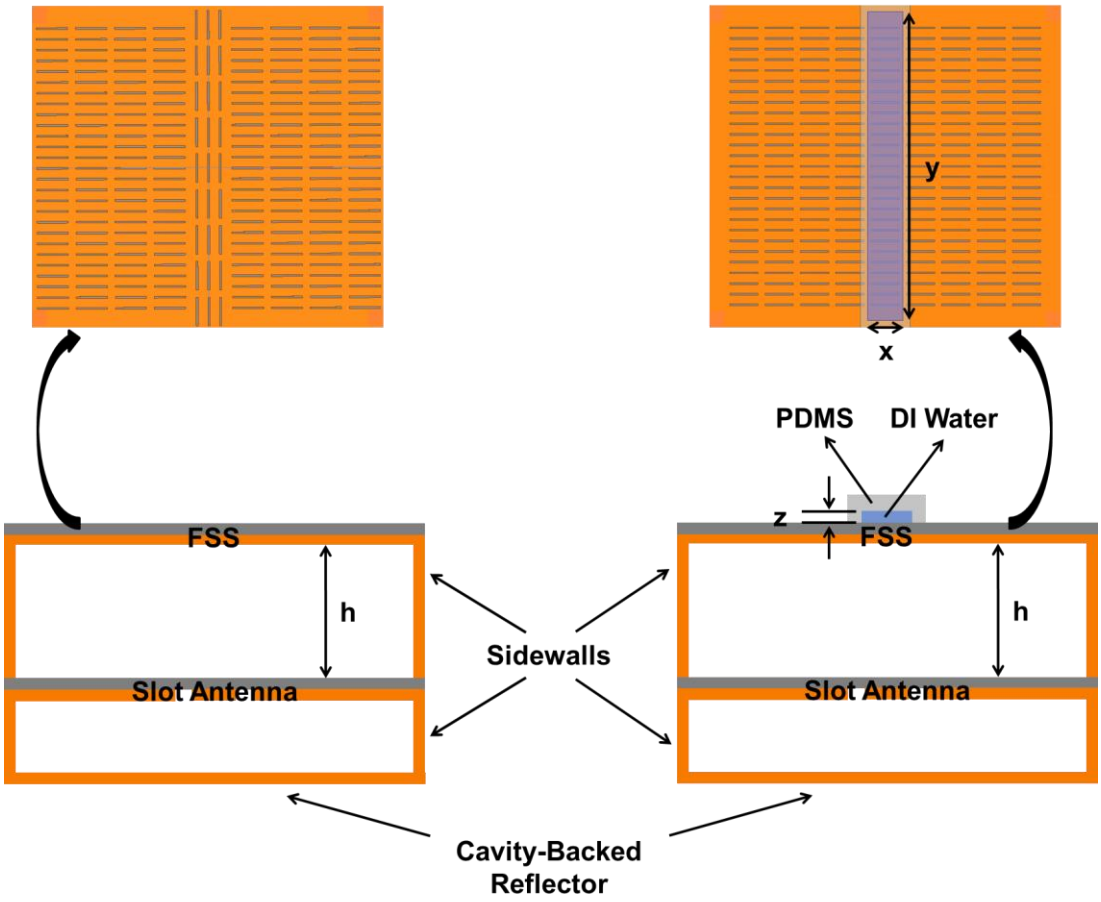

Fig. 5.16. Cavity-backed FPC antenna systems with (a) augmented FSS (FSS-1V) and (b) microfluidic FSS (FSS-AH w/ fluidic channel)

5.5.2. Fabrication

Details for the fabrication have been discussed in the section 5.4.2.

5.5.3. Results

The near-field distribution 5 mm above FSS for each FPC system at 11.2 GHz is shown in Fig. 5.17. The beam is split along the W-E line because highly reflective surface (vertically oriented unit cells or microfluidic channel) reflect energy from the

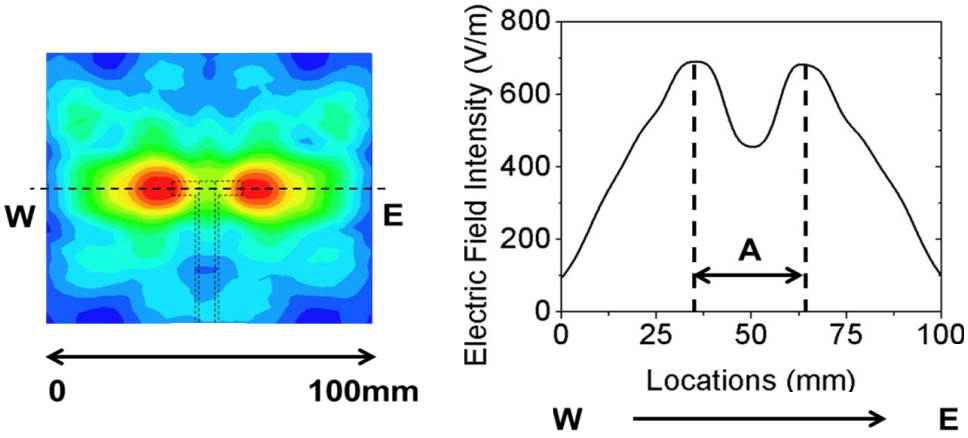

(a) **FSS-1V**

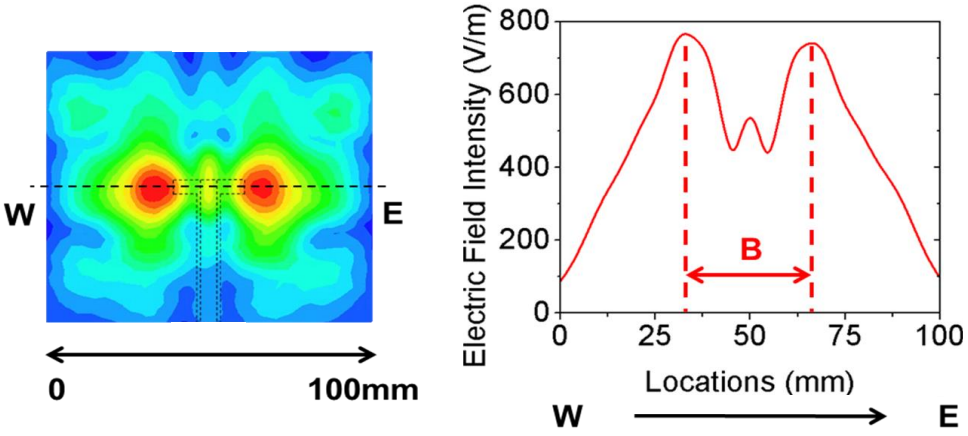

(b) **FSS-AH with 8 mm narrow channel**

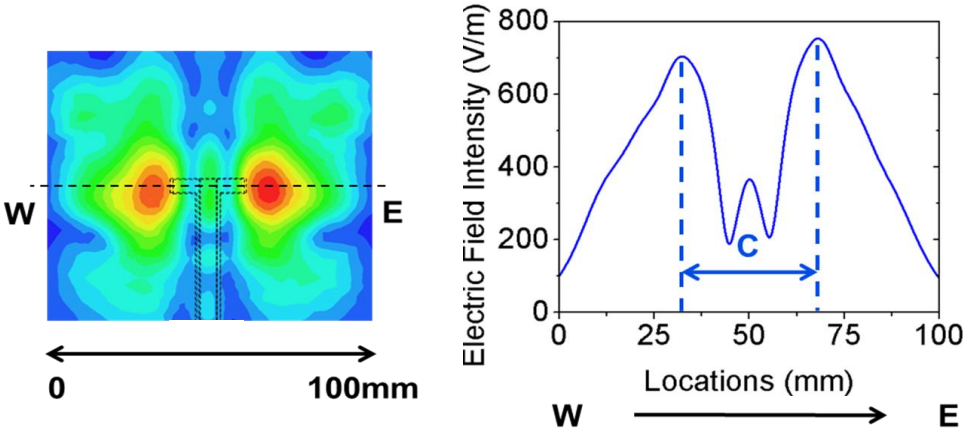

(c) **FSS-AH with 10 mm wide channel**

Fig. 5.17. 2D near-field distribution above FSS (left) and 1D electric field intensity along the W-E line (right)

source back to the cavity and thus the beam above the region over the slot and feedline is suppressed. For the FSS-1V case in Fig. 5.17(a), the spacing between split beams (A) is 29.75 mm and the peak field intensity is 691 V/m. The null between split beams decreases to 456 V/m. The microfluidic channel is used to synthesize the behavior of the vertically oriented unit cells region of the FSS-1V in a reconfigurable manner. For the FSS-AH with 8 mm narrow channel in Fig. 5.17(b), the beam spacing (B) increases by 3.5 mm (~ 12 %) to 33.25 mm and the peak field intensity increases by 76 V/m (~ 11 %) to 767 V/m compared to the FSS-1V case. For the FSS-AH with 10 mm wide channel in Fig. 5.17(c), the spacing (C) increases by 6 mm (~ 20 %) to 35.75 mm and the peak field intensity increases by 62 V/m (~ 9 %) to 753 V/m compared to the FSS-1V case. The narrow channel produces more similar near-field behavior to the 1V design.

The simulated far-field radiation patterns at 11.2 GHz for each FPC system are shown in Fig. 5.18. The H-plane has side lobes that result from two split beams along the W-E line corresponding to H-plane cut. For the FSS-1V design, the peak gain is 17.21 dB and side lobe level is ~ 4.3 dB. For the FSS-AH with narrow channel, the peak gain increases approximately by 1 dB (~ 24 %) to 18.16 dB but side lobe level also increases to 7.08 dB. For the FSS-AH with wide channel, the peak gain slightly drops to 17.83 dB but side lobe level increases to 9.83 dB. It is observed that the larger spacing between two split beams, the higher the H-plane side lobe levels.

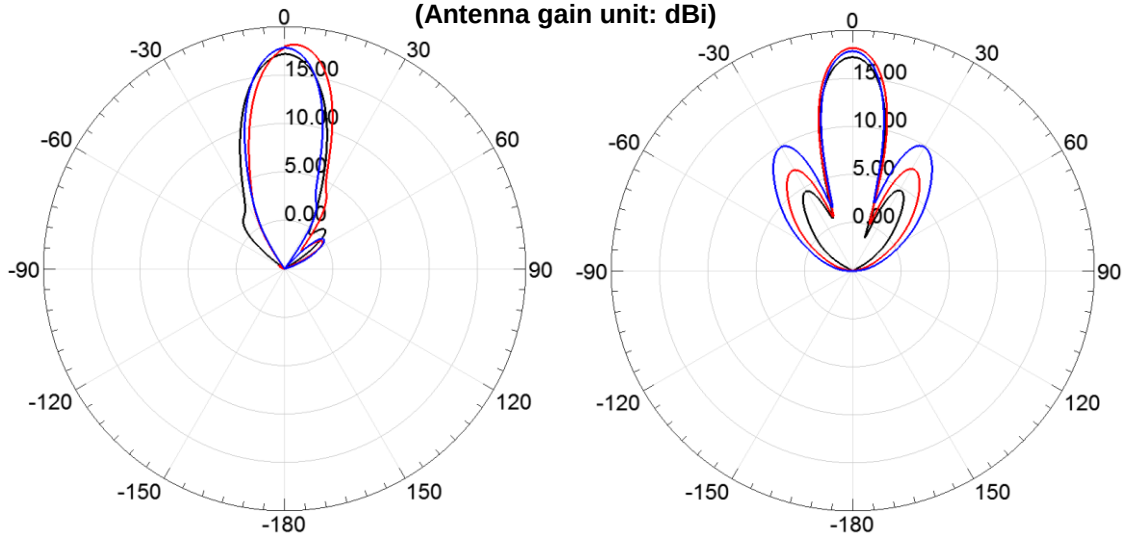

(a) (b)

Fig. 5.18. Simulated far-field radiation patterns for FPC antenna system with FSS-1V (**black**), FSS-AH w/ 8 mm narrow channel (**red**) and FSS-AH w/ 10 mm wide channel (**blue**) at 11.2 GHz

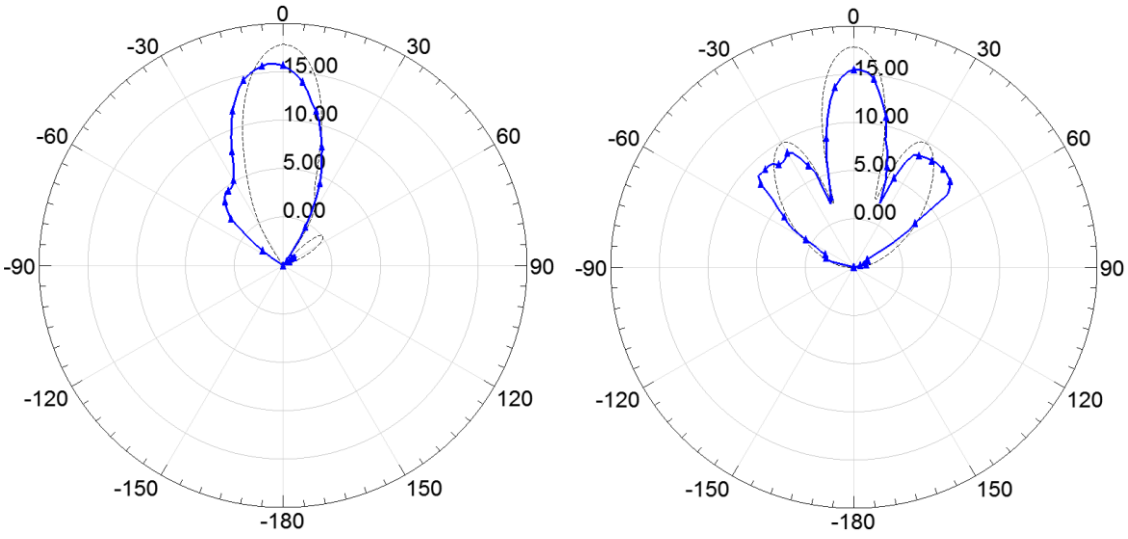

(a) (b)

Fig. 5.19. Simulated (**dashed**) and measured (**solid**) far-field radiation patterns for FSS-AH w/ 10 mm wide channel at 10.91 GHz

5.6. Summary

In this chapter, a design approach to reconfigurable FPC antenna system using microfluids is discussed.

First, a microfluidic housing is integrated into the FPC system with slot antenna for tuning and switching. The placement of the fluidic square channel on the slot antenna achieves ~ 30 % of resonant frequency shift and makes the antenna switch off more effectively compared to rectangular channel.

Second, FSS augmentations with vertical unit cell sets are integrated into the FPC antenna system with slot or patch. As a result, the main beam from the source split equally in the near-field. It demonstrates that the location of the split beam is controlled by the width of vertical unit cell sets.

Third, a microfluidic channel on FSS design is used to alter an FSS design and thus achieves beam focusing or beam-splitting in the near-field. The use of the air inside PDMS creates more focused and tapered near-field beam while the fluid split the main beam horizontally compared to the FSS-AH having all horizontal unit cells.

Lastly, the microfluidic design approach is proposed to achieve near-field beam-splitting without modification of uniform FSS design. The augmented FSS design (FSS-1V) and 8 mm narrow fluidic FSS split the beam to be located at the edge of the slot antenna and produce similar near- and far-field behavior.

CHAPTER 6

High Efficiency FPC Antenna Systems using FSS Subarrays

6.1. Introduction

Recent advances in the field of RF wireless communication require high compact size of the RF/microwave devices. As a result, antenna aperture efficiency improvement that results from the gain enhancement is of high interest and importance to provide the required power for the compact devices. In this chapter, a design approach to increase aperture efficiency of an FPC antenna system is investigated and discussed. An FPC antenna system with slot antenna and rectangular FSS as discussed so far is studied to optimize the FSS size and thus improve the efficiency.

6.2. Design/Results

The cavity-backed FPC antenna system and the FSS subarray to be simulated in HFSS for efficiency enhancement are shown in Fig. 6.1. The source antenna is a cavity-backed slot antenna and FSS unit cell is rectangular. The baseline FSS size is 9 by 27 unit cells (W × L = 100 × 91 mm^2), which has an aperture efficiency of 36.9 %. Several FSS subarrays are evaluated to compare the efficiency. For a fixed FSS length (L) along the vertical direction, three FSS designs are considered: (L-1) 3 by 27 unit cells (40 × 91 mm^2), (L-2) 5 by 27 unit cells (60 × 91 mm^2) and (L-3) 7 by 27 unit cells (80 × 91 mm^2).

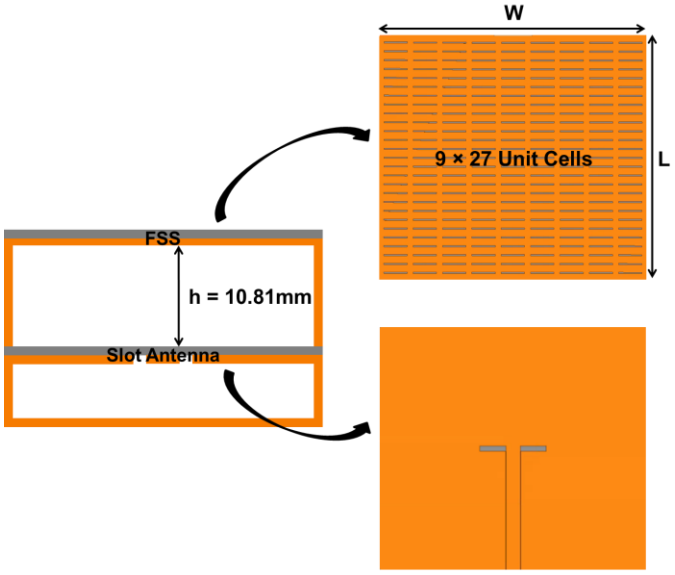

# of unit cells	FSS size (W × L)
3 × 27	40 × 91 mm²
5 × 27	60 × 91 mm²
7 × 27	80 × 91 mm²

# of unit cells	FSS size (W × L)
9 × 15	100 × 55 mm²
9 × 17	100 × 61 mm²
9 × 21	100 × 73 mm²
9 × 23	100 × 79 mm²

(a) (b)

Fig. 6.1. Cavity-backed FPC antenna system: (a) cross-section view (b) number of FSS unit cells and corresponding FSS size

For a fixed FSS width (W) along the horizontal direction, four designs are considered: (W-1) 9 by 15 unit cells (100 × 55 mm^2), (W-2) 9 by 17 unit cells (100 × 61 mm^2), (W-3) 9 by 21 unit cells (100 × 73 mm^2) and (W-4) 9 by 23 unit cells (100 × 79 mm^2). The size of the slot antenna layer corresponds to each FSS dimension proposed above.

The near-field distribution 5 mm above each FSS and far-field radiation patterns for the fixed FSS length (L) and fixed FSS width (W) are shown in Fig. 6.2 and Fig. 6.3, respectively. The peak gain and corresponding aperture efficiency are summarized in Table 6.1 and Table 6.2. For a fixed FSS length (L = 91 mm) along the vertical direction, the width is varied from 40 mm to 80 mm along the horizontal direction. In the near-field region, the electric field is focused around the center of the system and the field is

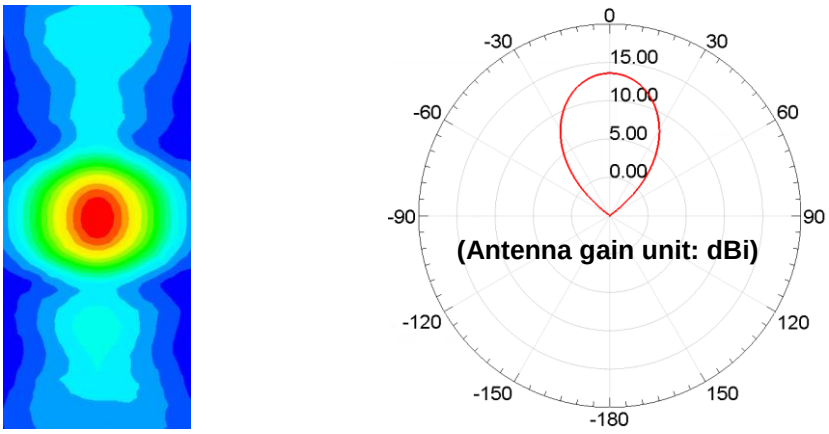

(a) **3 × 27**

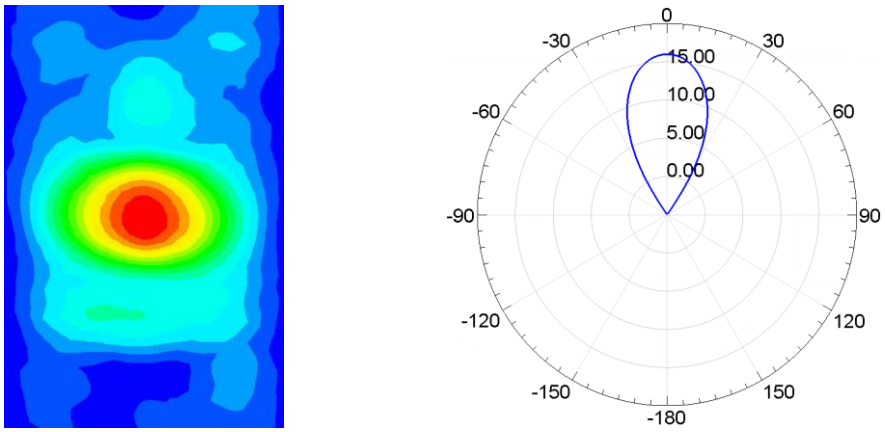

(b) **5 × 27**

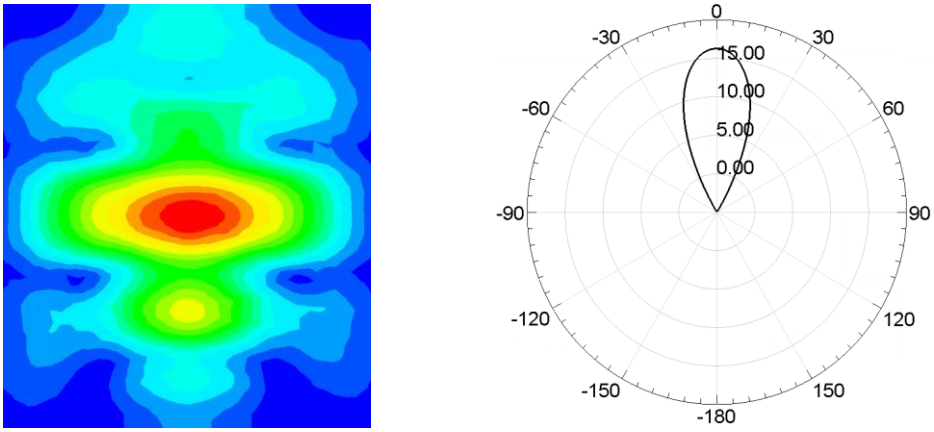

(c) **7 × 27**

Fig. 6.2. 2D near-field distribution above each FSS (left) and H-plane far-field radiation patterns (right) for a fixed FSS length (L) along the vertical direction

Table 6.1. Peak gain and aperture efficiency for a fixed FSS length (L)

	Peak gain (dBi)	Aperture efficiency (%)
3 × 27	13.59	35.9
5 × 27	15.99	41.5
7 × 27	16.28	33.3
9 × 27 (baseline)	17.70	36.9

symmetrically distributed along the horizontal direction in all cases. As the FSS width increases from 3 to 7 unit cells, the field elongates along the horizontal direction, and thus the shape of the field becomes more oval. In the far-field region, as the FSS width increases, this broadening of the near-field results in a narrowing of the far-field beamwidth. This effect is associated with more uniform near-field distribution along the H-plane cut. The peak gain of the H-plane radiation patterns, therefore, increases from 13.59 dBi to 16.28 dBi and the beamwidth reduces from 44˚ to 22˚. This results in slight increase of the aperture efficiency by ~ 5 %, however, compared to the baseline.

For a fixed FSS width (W = 100 mm) along the horizontal direction, the length is varied from 55 mm to 79 mm along the vertical direction. In the near-field region, the

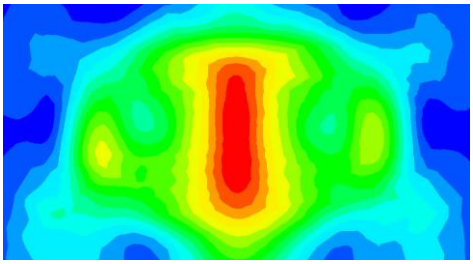

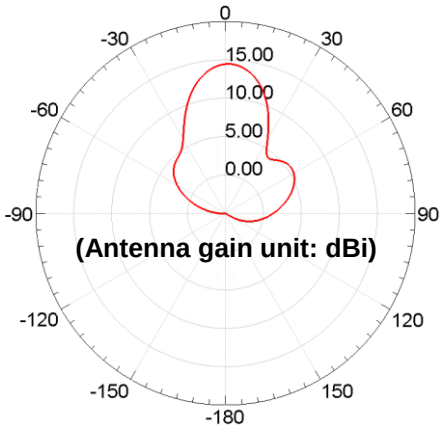

(a) **9 × 15**

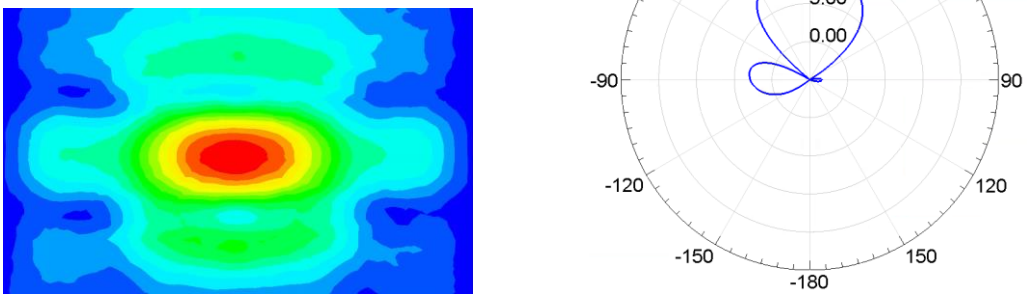

(b) **9 × 17**

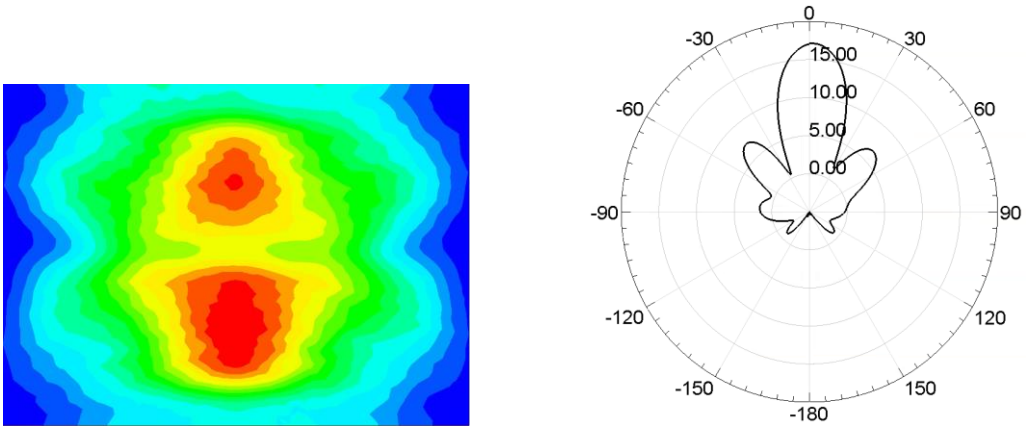

(c) **9 × 21**

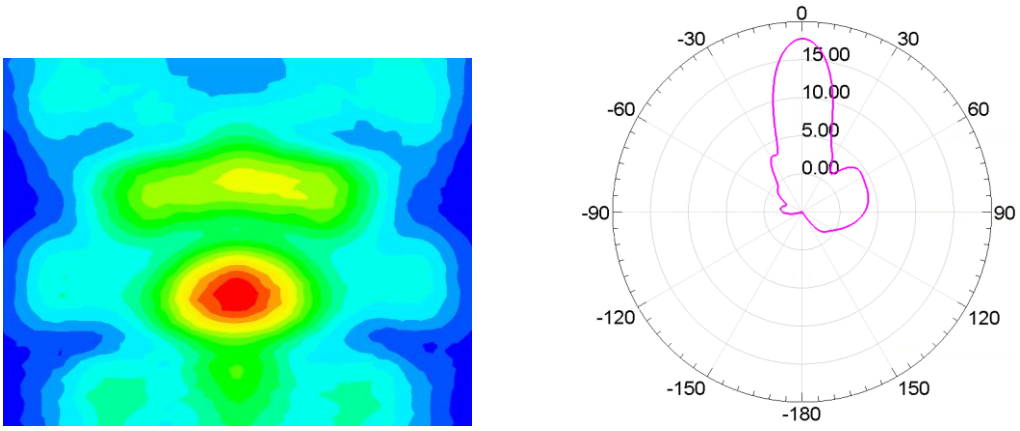

(d) **9 × 23**

Fig. 6.3. 2D near-field distribution above each FSS (left) and E-plane far-field radiation patterns (right) for a fixed FSS width (W) along the horizontal direction

Table 6.2. Peak gain and aperture efficiency for a fixed FSS width (W)

	Peak gain (dBi)	Aperture efficiency (%)
9 × 15	14.47	29.1
9 × 17	16.11	38.2
9 × 21	17.10	40.0
9 × 23	17.79	43.0
9 × 27 (baseline)	17.70	36.9

electric field is concentrated around the center for 9 × 15 (L = 55 mm) and 9 × 17 (L = 61 mm). As the FSS length increases, the beam is split in the vertical direction when 9 × 21 (L = 73 mm) then becomes more focused but displaced from the center when 9 × 23 (L = 79 mm). In the far-field region, as the FSS length increases, the peak gain of the E-plane radiation patterns increases from 14.47 dBi to 17.79 dBi and appears to be heading toward a max (L = 79 mm) since the baseline has the gain of 17.70 dBi when L = 91 mm. The aperture efficiency of L = 79 mm increases slightly by ~ 7 % compared to the baseline.

Decreasing the FSS width or length for a fixed length or width increase slightly the efficiency, respectively. When considering small value of L = 37 mm, it was determined that the efficiency did increase. It is observed that 5 × 9 (L = 37 mm) subarray has the peak gain of 14.0 dBi and the corresponding efficiency is 64.6 %. This FSS subarray design increases the efficiency considerably by ~ 30 % compared to the baseline (36.9 %) in exchange for gain 3 dB lower than the baseline. The near-field distribution and far-field radiation pattern for 5 × 9 subarray are shown in Fig. 6.4. The

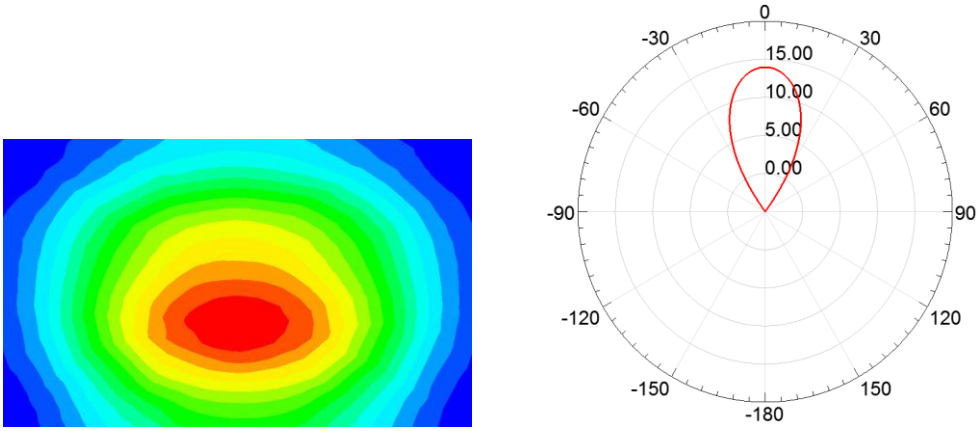

Fig. 6.4. 2D near-field distribution above each FSS (left) and H-plane far-field radiation patterns (right) for the FPC antenna system with 5 × 9 FSS subarray

preliminary results shown above imply that further investigation is needed to optimize the FSS subarray for aperture efficiency improvement. This last result is promising and indicates there is potential to design the high efficiency FPC antenna systems using high efficient FSS subarray elements.

6.3. Summary

In this chapter, the high efficiency FPC antenna systems using FSS subarray are investigated and discussed. The 9 × 27 FSS array is the baseline and has the aperture efficiency of 36.9 %. Various FSS subarrays are evaluated by simulations: A design with 5 × 9 FSS subarray showed increased efficiency to 64.6 %, an increase of ~ 30 % relative to the baseline design. The tradeoff for this improvement was antenna gain from 17.70 dBi to 14.0 dBi, which may be acceptable in many applications.

CHAPTER 7

Conclusion and Future Work

7.1. Conclusion

In this thesis, a scaled model of an FPC antenna system consisting of a single source and FSS was developed and discussed as beamforming antenna systems for customized RFID system. Due to beam focusing of FSS, the FPC antenna system creates high directivity/gain which can provide the power required for specification.

A parametric and comparative study of the FPC antenna systems is performed. Various FSS unit cells with different aperture type are parametrized to evaluate the energy leakage and aperture ratio. It demonstrates that energy leakage is more dependent on the aperture width (W) than the length (L) in rectangular unit cell. The aperture ratio has more significant effect in energy leakage of the square unit cell relative to the circular unit cell. Based on the unit cell results, FPC antenna system with a slot antenna and rectangular FSS is studied and evaluated in the near- and far-field. Also, as a function of beamforming capability, FSS geometry/source type is investigated. The circular FSS array increases the peak gain by 2 dB compared to rectangular FSS geometry. Using the circular FSS design, the slot antenna has highest peak gain relative to patch antenna case.

The FPC antenna system is also characterized to investigate CPW feedline effect with FSS geometry in the near- and far-field. With an FSS, beam focusing of feedline occurs. Thus, the FPC system performance is improved by augmenting the FSS with 90˚

rotated unit cells along the feedline length and thus minimizing the beam focusing effect of feedline. Fully enclosed structure account for 3 dB improvement in the far-field compared to open structure with bi-directionally radiated source.

To investigate the reconfigurability, microfluidic FPC antenna systems are developed. To provide tuning and switching capability microfluidic channel is integrated into the cavity. The microfluidic square channel shifts resonant frequency by ~ 30 % relative to the air case and switch off the antenna more effectively relative to rectangular channel. To synthesize the behavior of the augmented FSS structure a microfluidic channel is attached to the uniform FSS design. In near-field, beam-splitting is observed where one source is split into two beams or more. This technique can be used for interchip communication and biomedical imaging.

The efficiency observed was lower than desired. To improve efficiency, different FSS subarrays are evaluated by simulations. 5 × 9 FSS subarray design increased the aperture efficiency by 30 % to 64.6 % compared to the baseline efficiency of 36.9 % for the 9 × 27 FSS rectangular unit cell design studied in most of this work.

7.2. Future Work

In this work, an FPC antenna system has been investigated and discussed as scaled model of beamforming antenna systems for potential use in 60 GHz customized RFID applications. The novel technique to split the near-field beam using microfluids provides the potential to be useful for many applications. The next step for this work is to develop

the beam-splitting technique to control the spacing between split beams and the number of the split beams, which can be done by reconfiguring the FSS with microfluids. This technique will offer the advantage of splitting power without complex modification of the FSS array in 3-D array and packaging applications.

To improve FPC antenna system efficiency more FSS subarray designs should be investigated and optimized to identify maximum efficiency. The next step would be to develop the FPC antenna system that consist of the multiple of high efficient FSS subarrays.

Lastly, all FPC system designs discussed so far have been developed at the design frequency of 12 GHz. The motivation for this work was V-band (40 – 75 GHz) applications for RFID system. This version in silicon should be implemented and tested to understand performance on high ε_r materials to determine what design modifications are needed.

BIBLIOGRAPHY

[1] Hau-Ling Chan, Tsan-Ming Choi, Chi-Leung Hui, and Sau-Fan Ng, "Quick response healthcare apparel supply chains: value of RFID and coordination," *IEEE Trans. Syst, Man Cybern: Syst*, vol. 45, no. 6, pp. 887–900, Jun. 2015

[2] S. F. Wamba, "RFID enabled healthcare applications, issues and benefits: An archival analysis (1997–2011)," *Jour. Med. Syst.*, vol. 36, no. 6, pp. 3393–3398, Dec. 2012

[3] Luca Catarinucci, Riccardo Colella, Luca Mainetti, Luigi Patrono, Stefano Pieretti, Ilaria Sergi, and Luciano Tarricone, "Smart RFID antenna system for indoor tracking and behavior analysis of small animals in colony cages," *IEEE Sensor J.*, vol. 14, no. 4, pp. 1198–1206, Apr. 2014

[4] Paula Fraga-Lamas, and Tiago M. Fernandez-Carames, "Reverse engineering the communications protocol of an RFID public transportation card," *Proc. IEEE Int. Con. RFID.*, Phoenix, AZ, USA, pp. 1–6, May 2017

[5] Ramsey Z. Doany, Cody Lovejoy, Kyle Jones, and Harold Stern, "A CDMA-based RFID inventory system: A CDMA approach as a solution for decreased power consumption," *Proc. IEEE Int. Con. RFID.*, Orlando, FL, USA, pp. 1–4, May 2016

[6] M. C. Caccami, C. Miozzi, M. Y. S. Mulla, C. Di Natale, and G. Marrocco, "An epidermal graphene oxide-based RFID sensor for the wireless analysis of human breath," *Proc. IEEE Int. Con. RFID Tech. App.*, Warsaw, Poland, pp. 191–195, Sep. 2017

[7] Walther Pachler, Wolfgang Bösch, Gerald Holweg,and Guenther Hofer, "A novel booster antenna design coupled to a one square millimeter coil-on-chip RFID tag enabling new medical applications," *Proc. IEEE European Microw. Con.* Nuremberg, Germany, pp. 1003–1006, Oct. 2013

[8] Basari, Dony Canisius Sirait, Fitri Yuli Zulkifli and Eko Tjipto Rahardjo, "A simple folded dipole antenna for medical implant communications at 900 MHz band," *Proc. IEEE Asia-Pacific Con.*, Kaohsiung, Taiwan, pp. 421–423, Dec. 2012

[9] Zhibin Xiao, Xi Tan, Xianliang Chen, Sizheng Chen, Zijian Zhang, Hualei Zhang, Junyu Wang, Yue Huang, Peng Zhang, Lirong Zheng, and Hao Min, "An implantable RFID sensor tag toward continuous glucose monitoring," *IEEE Trans. Biomed. Health Inform.*, vol. 19, no. 3, pp. 910–919, May 2015

[10] K. Koski, E. Moradi, M. Hasani, J. Virkki, T, Björninen, L. Ukkonen and Y. Rahmat-Samii, "Electro-textiles – the enabling technology for wearable antennas in wireless body-centric systems," *Proc. IEEE Int. Symp. Ant. Prop.*, Vancouver, Canada, pp. 1203–1204, Jul. 2015

[11] Haiyu Huang, Peisen Zhao, Pai-Yen Chen, Yong Ren, Xuewu Liu, Mauro Ferrari, Ye Hu, and Deji Akinwande, "RFID tag helix antenna sensors for wireless drug dosage monitoring," *IEEE Jour. of Transl. Eng. Health Med.*, vol. 2, Mar. 2014

[12] E. Moradi, M.Waqas A. Khan, L. Sydänheimo, and L. Ukkonen, "Metamaterial isolator for RFID based biomedical repeater system," *Proc. IEEE Int. Symp. Ant. Prop.*, San Diego, CA, USA, pp. 227–228, Jul. 2017

[13] Chanjoon Lee, Robert Sainati, and Rhonda Franklin, "Parametric study of near- and far-field performance of the Fabry-Perot Cavity antenna system," *Proc. IEEE Wireless Microw. Tech. Con.*, Clearwater Beach, FL, USA, pp. 1–4, Apr. 2016

[14] David R. Jackson, and Arthur A. Oliner, "A leaky-wave analysis of the high-gain printed antenna configuration," *IEEE Trans. Ant. Prop.*, vol. 36, no. 7, pp. 905–910, Jul. 1988

[15] Tianxia Zhao, David R. Jackson, Jeffery T. Williams, Hung-Yu David Yang, and Arthur A. Oliner, "2-D periodic leaky-wave antennas—part I: metal patch design," *IEEE Trans. Ant. Prop.*, vol. 53, no. 11, pp. 3505–3514, Nov. 2005

[16] Tianxia Zhao, David R. Jackson, and Jeffery T. Williams, "2-D periodic leaky-wave antennas—part II: slot design," *IEEE Trans. Ant. Prop.*, vol. 53, no. 11, pp. 3515–3524, Nov. 2005

[17] A.P. Feresidis and J.C. Vardaxoglou, "High gain planar antenna using optimised partially reflective surfaces," *Proc. IEEE Microw. Ant. Prop.*, vol. 148, no. 6, pp. 345–350, Dec. 2001

[18] Ronan Sauleau, Philippe Coquet, Toshiaki Matsui, and Jean-Pierre Daniel, "A new concept of focusing antennas using plane-parallel Fabry–Perot Cavities with nonuniform mirrors", *IEEE Trans. Ant. Prop.*, vol. 51, no. 11, pp. 3171–1990, Nov. 2003

[19] James R. Kelly and Alexandros P. Feresidis, "Array antenna with increased element separation based on a Fabry–Pérot resonant Cavity with AMC walls," *IEEE Trans. Ant. Prop.*, vol. 57, no. 3, pp. 682–687, Mar. 2009

[20] R. Sauleau, Ph. Coquet and T. Matsui, "Low-profile directive quasi-planar antennas based on millimetre wave Fabry–Perot cavities," *Proc. IEEE Microw. Ant. Prop.*, vol. 150, no. 4, pp. 274–278, Sep. 2003

[21] Li Yanfei, Raj Mittra and Lu Guizhen, "A novel design for a low profile high directivity Fabry-Perot cavity antenna," *Proc. IEEE Int. Symp. Ant. Prop.*, Charleston, SC, USA, pp. 1–3, Jun. 2009

[22] Amit K. Singh, Mahesh P. Abegaonkar, and Shiban K. Koul, "High-gain and high-aperture-efficiency cavity resonator antenna using metamaterial superstrate," *IEEE Ant. Wireless Prop. Letter*, vol. 16, pp. 2388–2391, Jun. 2017

[23] C. Mateo-Segura, A.P. Feresidis, and G. Goussetis, "Analysis of broadband highly-directive Fabry-Perot cavity leaky-wave antennas with two periodic layers," *Proc. IEEE Int. Symp. Ant. Prop.*, Toronto, ON, Canada, pp. 1–4, Jul. 2010

[24] D. Kim, J. H. Ju and J. I. Choi, "A wideband Fabry-Perot Cavity antenna with successively tapered meandering loops," *Proc. IEEE European Con. Ant. Prop.*, Rome, Italy, pp. 604–605, May. 2011

[25] Konstantinos Konstantinidis, Alexandros P. Feresidis, and Peter S. Hall, "Multilayer partially reflective surfaces for broadband Fabry-Perot Cavity antennas," *IEEE Trans. Ant. Prop.*, vol. 62, no. 7, pp. 3474–3481, Jul. 2014

[26] Renato Gardelli, Matteo Albani, and Filippo Capolino, "Array thinning by using antennas in a Fabry–Perot Cavity for gain enhancement", *IEEE Trans. Ant. Prop.*, vol. 54, no. 7, pp. 1979–1990, Jul. 2006

[27] S.I. Latif, L. Shafai and C. Shafai, "Gain and efficiency enhancement of compact and miniaturised microstrip antennas using multi-layered laminated conductors," *IET Microw. Ant. Prop.*, vol. 5, no. 4, pp. 402–411, Apr. 2011

[28] Scale model antenna measurments http://www.antenna-theory.com/measurements/scalemodel.php

[29] S.Ali Hosseini, Filippo Capolino, and Franco De Flaviis, "Single-feed highly-directive Fabry-Perot Cavity antenna for 60 GHz wireless systems: Design and Fabrication," *Proc. IEEE Int. Symp. Ant. Prop.*, Orlando, FL, USA, pp. 746–747, Jul. 2013

[30] Bing Han, Xue-xia Yang, and Hai-gao Xue, "A millimeter-wave Fabry-Perot antenna with high-gain and circular polarization operation," *Proc. IEEE Asia-Pacific Con. Ant. Prop.*, Harbin, China, pp. 40–43, Jul. 2014

[31] Yoonjae Lee, Xuesong Lu, Yang Hao, Shoufeng, Yang, Julian R. G. Evans, and Clive G. Parini, "Low-profile directive millimeter-wave antennas using free-formed three-dimensional (3-D) electromagnetic bandgap structures," *IEEE Trans. Ant. Prop.*, vol. 57, no. 10, pp. 2893–2903, Oct. 2009

[32] Frequency selective surface https://en.wikipedia.org/wiki/Frequency_selective_surface

[33] G. Von Trentini, "Partially reflecting sheet arrays," *IRE Trans. Ant. Prop.*, vol.4, no. 4, pp. 666–671, Oct. 1956

[34] ANSYS High Frequency Structure Simulator (HFSS), Version 15, Pittsburgh, PA, 2013

[35] Master and Slave Boundaries https://ansyshelp.ansys.com/account/secured?returnurl=/Views/Secured/Electronics/v182/home.htm%23/Subsystems/HFSS/Content/HFSS/MasterandSlaveBoundaries.htm?Highlight=master%20slave%20boundary

[36] S. Ali Hosseini, Filippo Capolino, and Franco De Flaviis, "A 63 GHz single-feed low-profile Fabry-Pérot cavity antenna using a thick metallic FSS," *Proc. IEEE Int. Symp. Ant. Prop.*, Orlando, FL, USA, pp. 746–747, Jul. 2013

[37] T.K. Wu, "Frequency Selective Surface and Grid Array," Wiley, 1995

[38] Ben A. Munk, "Finite Antenna Arrays and FSS," John Wiley & Sons, 2003

[39] Ben A. Munk, "Frequency Selective Surfaces: Theory and Design," John Wiley & Sons, 2005

[40] Chanjoon Lee, Robert Sainati, and Rhonda Franklin, "Comparative analysis of frequency selective surface geometry effect in Fabry-Perot Cavity antenna design," *Proc. IEEE Wireless Microw. Tech. Con.*, Clearwater, FL, USA, pp. 1–4, Apr. 2015

[41] Chanjoon Lee, Robert Sainati, and Rhonda Franklin, "Analysis of coplanar waveguide feedline effect on Fabry-Perot Cavity antenna system performance," *Proc. IEEE Int. Symp. Ant. Prop.*, Fajardo, Puerto Rico, pp. 353–354, Jun. 2016

[42] Outmane Lemtiri Chlieh, Carlos A. Donado Morcillo, Spyridon Pavlidis, Wasif T. Khan, and John Papapolymerou, “Integrated microfluidic cooling for GaN devices on multilayer organic LCP substrate,” *Proc. IEEE Int. Microw. Symp.*, Seattle, WA, USA, pp. 1–4, Jun. 2013

[43] Outmane Lemtiri Chlieh, Wasif T. Khan, and John Papapolymerou, “Integrated microfluidic cooling of high power passive and active devices on multilayer organic substrate,” *Proc. IEEE Int. Microw. Symp.*, Tampa, FL, USA, pp. 1–4, Jun. 2014

[44] C. Murray, R.R. Franklin, “Frequency tunable fluidic annular slot antenna,” *Proc. IEEE Int. Symp. Ant. Prop.*, Orlando, FL, USA, pp. 386–387, Jul. 2013

[45] C. Murray, R.R. Franklin, “Independently tunable annular slot antenna resonant frequencies using fluids,” *IEEE Ant. Wireless Prop. Letter*, vol. 13, pp. 1449–1452, Jul. 2014

[46] Casey Murray, and Rhonda R. Franklin, “EDGE coupled variable microfluidic directional coupler,” *Microw. Optical Tech. Letters*, vol. 55, no. 4, pp. 756–758, Feb. 2013

[47] C. Murray, R.R. Franklin, “Fluidically adjustable degenerate mode microstrip ring filter,” *Proc. IEEE Wireless Microw. Tech. Con.*, Tampa, FL, USA pp. 1–3, Jun. 2014

[48] A. Dey, R. Guldiken, and G. Mumcu, "Wideband frequency tunable liquid metal monopole antenna," *Proc. IEEE Int. Symp. Ant. Prop.*, Orlando, FL, USA, pp. 392–393, Jul. 2013

[49] Alireza Pourghorban Saghati, Jaskirat Batra, Jun Kameoka, and Kamran Entesari, “A microfluidically-tuned dual-band slot antenna,” *Proc. IEEE Int. Symp. Ant. Prop.*, Memphis, TN, USA, pp. 1244–1245, Jul. 2014

[50] Tonmoy Bhattacharjee, Hongrui Jiang, and Nader Behdad, “A fluidically tunable, dual-band patch antenna with closely spaced bands of operation,” *IEEE Ant. Wireless Prop. Letter*, vol. 15, pp. 118–121, May 2015

[51] Michael S. Kelley and Gregory H. Huff, “Fluidic tuning of a frequency selective surface based on a four-arm Archimedean spiral,” *Proc. IEEE Int. Symp. Ant. Prop.*, Orlando, FL, USA, pp. 468–469, Jul. 2013

[52] M.R. Khan, G.J. Hayes, S. Zhang, M.D. Dickey, G. Lazzi, "A pressure responsive fluidic microstrip open stub resonator using a liquid metal alloy," *IEEE Microw. Wireless Comp. Letters*, vol.22, no.11, pp. 577–579, Nov. 2012

[53] Emre Erdil, Kagan Topalli, Nasim Seyedpour Esmaeilzad1, Özge Zorlu, Haluk Kulah, Ozlem Aydin Civi, “A reconfigurable nested ring-split ring transmitarray unit cell by microfluidic technology,” *European Con. Ant. Prop.*, The Hague, Netherlands, pp. 1–4, Apr. 2014

[54] Tonmoy Bhattacharjee, Hongrui Jiang, and Nader Behdad, “Large-scale fluidic tuning of subwavelength periodic structures,” *IEEE Ant. Wireless Prop. Letter*, vol. 14, pp. 190–193, Sep. 2014

[55] Sumanth K. Pavuluri, Carolina Mateo-Segura, Elizabeth McKeever, George Goussetis, David Flynn, Marc P.Y, “Integration of microfluidic channels with

frequency selective surfaces for sensing and tuning," *European Con. Ant. Prop.*, The Hague, Netherlands, pp. 133–136, Apr. 2014

[56] Chanjoon Lee, Robert Sainati, Rhonda Franklin and Ramesh Harjani, "Fluidic switching and tunig of Fabry-Perot antenna," *Proc. IEEE Int. Symp. Ant. Prop.*, Vancouver, Canada, pp. 2211–2212, Jul. 2015

[57] Chanjoon Lee, Robert Sainati, and Rhonda Franklin, "Fabry-Perot Cavity antenna system with beam-splitting of near-field radiation," *Proc. IEEE Int. Symp. Ant. Prop.*, Fajardo, Puerto Rico, pp. 355–356, Jun. 2016

[58] Chanjoon Lee, Robert Sainati, and Rhonda Franklin, "Design of near-field beam-splitting frequency selective surfaces for Fabry-Perot Cavity antenna systems," *Proc. IEEE European Microw. Con.*, London, UK, pp. 1191–1194, Oct. 2016

[59] Chanjoon Lee, Robert Sainati, Rhonda Franklin, "Reconfigurable frequency selective surface for Fabry-Perot Cavity antenna system," *Proc. IEEE Int. Symp. Ant. Prop.*, San Diego, CA, USA, pp. 1983–1984, Jul. 2017

[60] Chanjoon Lee, Robert Sainati, Rhonda Franklin, "Microfluidic near-field beam-splitting frequency selective surface for Fabry-Perot Cavity antenna system," *Proc. IEEE Int. Symp. Ant. Prop.*, San Diego, CA, USA, pp. 2337–2338, Jul. 2017

[61] Getting Started with HFSS: Floquet Port http://www.1cae.com/articleAccessory/2017/04/16/HFSS%20Floquet%20Ports.pdf

APPENDIX A

Customized Radio Frequency Identification at 60 GHz

A.1. Introduction

This work was inspired by the desire to create customized RFID system at 60 GHz. To do so, specific design requirements were needed to proceed. Below are the design considerations and requirements that impacted the scaled model antenna in this work and gain requirements.

A.2. Design Considerations

The customized RFID system for blood monitoring is shown in Fig. A.1. A reader transmits RF power to a tag attached to blood bag and backscattered energy from the tag is transferred to the reader. Once the tag receives power from the reader, it is transferred to a rectifier through matching network. Using charge pump, energy is stored in super capacitor to keep monitoring temperature during a certain period of time. There are main parameters to consider: (1) transmit frequency, (2) power received by tag vs. distance and area, and (3) turns ratio of transformer in matching circuit. They will be discussed in the following sections.

A.2.1. Frequency

In Chapter 1, the FCC regulates the intentional radiation from a radio transmitter.

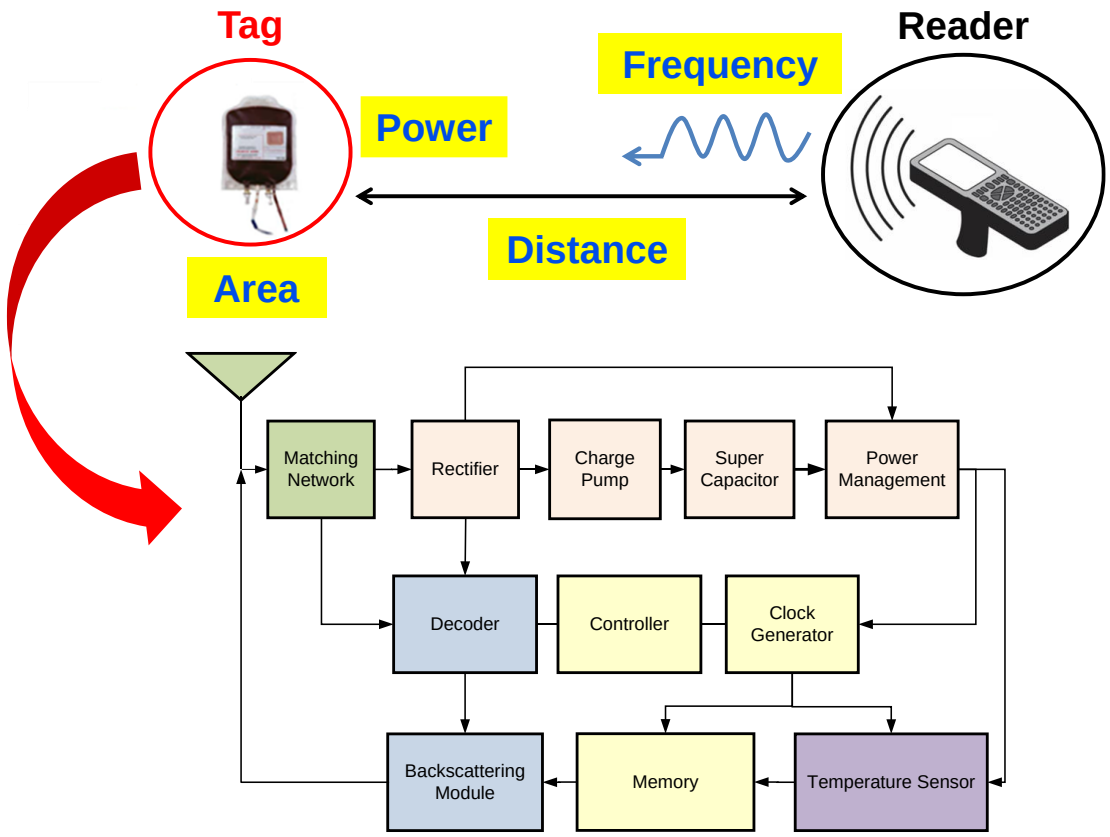

Fig. A.1. Customized RFID system

Therefore, a need exists to determine how much power can be transmitted over a frequency range to achieve maximum power transfer.

A.2.2. Power received by tag

As a reader transmits radio waves to a tag, the power received by the tag depends on distance between reader and tag and tag antenna size. According to FCC regulations, the power density for 57 – 64 GHz is 90 mW/m^2 at a distance of 3 m. Based on that, the power density over distance at 60 GHz is calculated and plotted as shown in Fig. A.2. Assuming that the tag antenna is square patch, the received power is calculated by

Equation 1.

$$P_{received} = P_{density}(\frac{3}{d})^2 l^2 \quad (1)$$

where $P_{density}$ is the power density at a distance of 3 m, d is the distance between reader and tag, and l is the antenna side length.

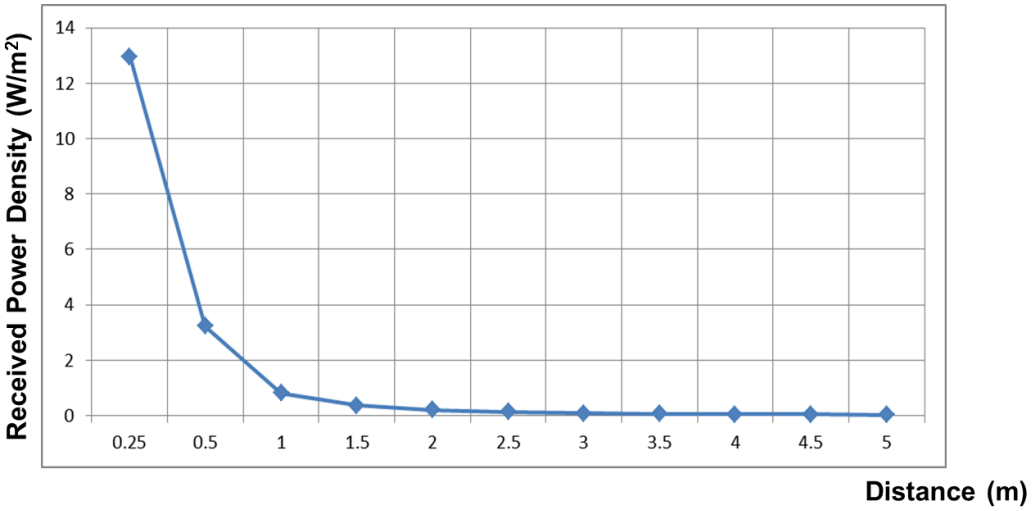

Fig. A.2. Received power density (W/m^2) vs. distance (m) at 60 GHz

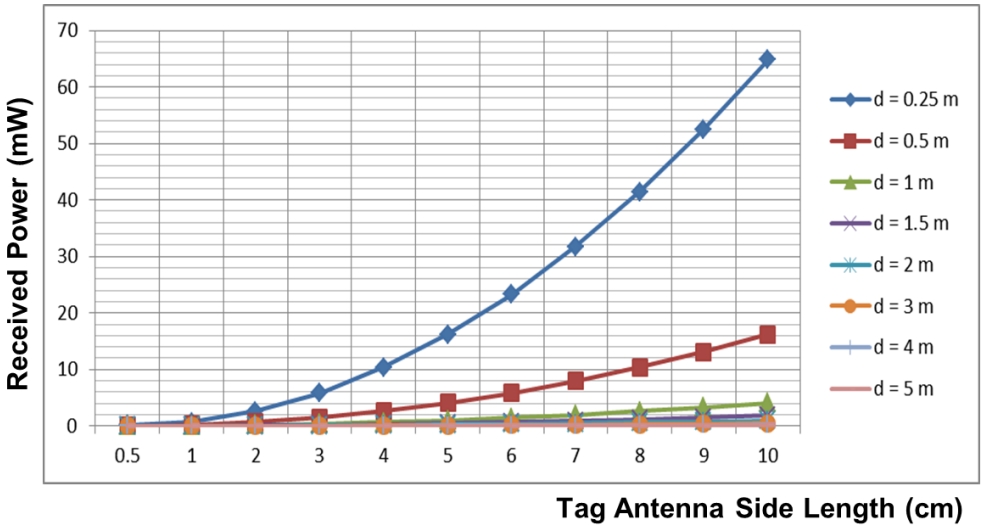

Fig. A.3. Received power (mW) vs. antenna side length (cm) depending on distance (d) between reader and tag at 60 GHz

The received power vs. antenna side length for various distance between reader and tag is shown in Fig. A.3. As expected, the received power is highest at a distance of 0.25 m. As separation increases, the power starts to decrease to below 20 mW. For a distance greater than 1 m, the power drops significantly to below 6 mW. A comparison to the power requirements will be discussed in section A.3.1.

A.2.3. Matching circuit

To maximize power transfer in the RF to DC conversion circuit from the tag antenna, the matching network needs to be carefully designed. The matching circuit is modeled in Advanced Design System (ADS). The RFID tag ADS circuit model is shown in Fig. A.5. The number 1 to 4 in the diagram Fig. A.5 corresponds to the components in ADS circuit model. The tag antenna (#1) is represented by voltage source (V_s) and 50 Ω source resistance (R_s). The matching network (#2) is represented by a transformer having turns ratio of 1 to N. A primary and secondary winding is set to be 1 and N, respectively. The rectifier and charge pump (#3) are described by a diode. The diode converts AC from the tag to DC current, where diode turn-on voltage ($V_{threshold}$) is 0.6 – 0.7 V. The super capacitor (#4) is illustrated by a parallel plate capacitor. The capacitor is used to store and provide energy for monitoring blood as long as possible (up to 1 week). Thus, the desired capacitance value is about 0.1 – 0.2 F. By Faraday's law of induction and law of conservation of energy, ideal transformer yields the following identity.

$$\frac{N_1}{N_2} = \frac{V_1}{V_2} = \frac{I_2}{I_1} \tag{2}$$

where N_i is the number of winding in primary or secondary coil, V_i is the voltage across primary or secondary coil, and I_i is the current through primary or secondary coil.

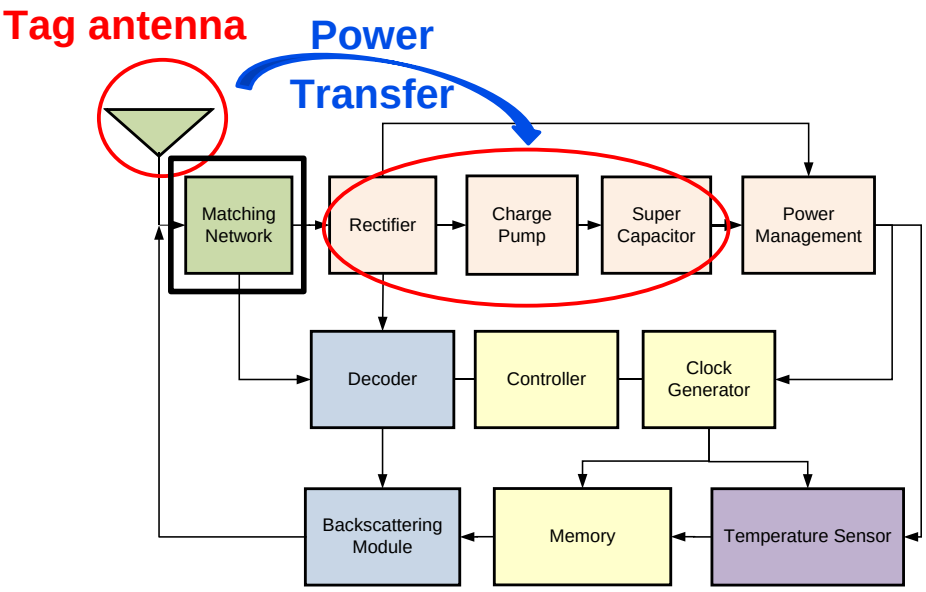

Fig. A.4. RFID tag antenna with matching network

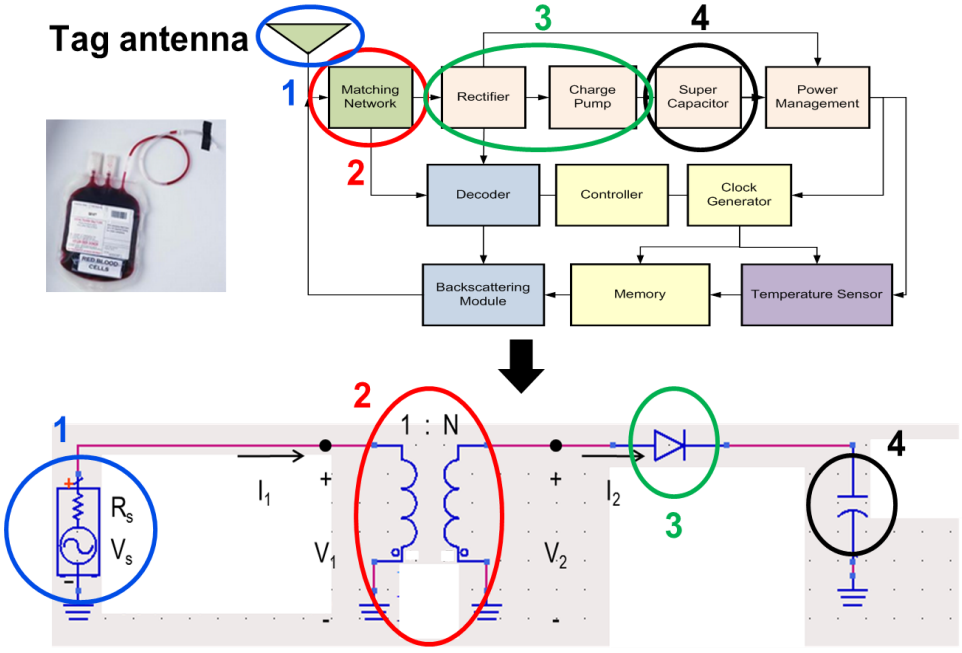

Fig. A.5. RFID tag with matching network and ADS circuit model

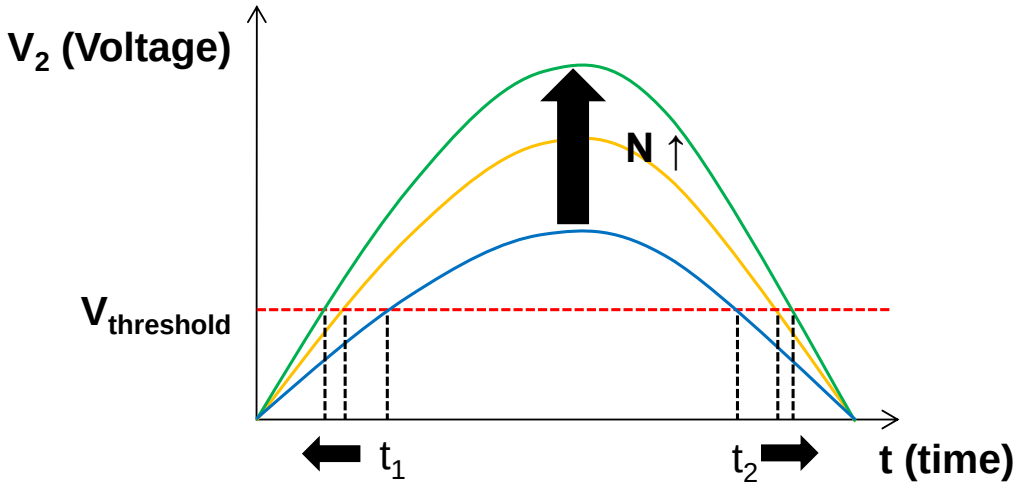

Fig. A.6. Voltage in secondary coil (V_2) vs. charging time (t_2-t_1) depending on the number of secondary winding

$$Q = \int_{t_1}^{t_2} I_2 \, dt \tag{3}$$

where Q is the charge stored in super capacitor, I_2 is the current through secondary coil, t_1 is the start time and t_2 is the end time for charging super capacitor.

When the induced voltage in secondary coil (V_2) is higher than the threshold voltage of diode (~ 0.6 to 0.7 V, $V_{threshold}$), the diode turns on and the charge starts to be stored in super capacitor at a time of t_1 and the charging ends at a time of t_2. Referring to Equation 3, the stored charge (Q) is proportional to the current (I_2) through super capacitor and charging time (t_2-t_1). As shown in Fig. A.6, the charging time (t_2-t_1) increases as the number of secondary winding (N) increases while the secondary current (I_2) decreases according to Equation 2. Therefore, the number of secondary winding needs to be optimized to maximize stored charge that results from power transfer from the tag antenna to the circuit.

A.3. Requirements

A.3.1. Tag

Since blood bags are transported and temperature needs to be monitored during transport, the super capacitor in the tag attached to the bags should be fully charged for a shorter time to make blood scanning process faster. The charging time, however, needs to provide enough power corresponding to distance between reader and tag, and tag size as discussed in section A.2. Assuming the voltage across the capacitor (V) is 3 V, from the rectifier and charge pump, the required power for given charging time (t) and capacitance (C) is calculated by Equation.4 – 6 and the results are presented in Table A.1.

$$Q = CV \tag{4}$$

$$I = \frac{Q}{t} \tag{5}$$

$$P_{required} = \frac{1}{2} VI \tag{6}$$

where V is the voltage across the super capacitor, C is the capacitance of the super capacitor and I is the current through the super capacitor. $P_{required}$ is the required power for given charging time and capacitance.

As show in Table A.1, the maximum required power of 60 mW is obtained for charging time of 15 sec and capacitance of 0.2 F. Thus, the power received by the antenna (l = 10 cm) at a distance of 0.25 m, as shown in Fig. A.3, meets this power requirement.

Table A.1. Required power for charging time and capacitance

Charging time (sec)	Capacitance (F)	Current (A)	Required power (mW)
15	0.1	20	30
15	0.2	40	60
60	0.1	5	7.5
60	0.2	10	15

A.3.2. Reader

The FCC regulation 15.255 for devices operating in the 60 GHz band initially specified the maximum level Equivalent Isotropically Radiated Power (EIRP) up to +40 dBmi. In August 2013, a ruling by the FCC extended the EIRP for outdoor use between fixed points up to +82 dBmi, depending on antenna gain. The maximum antenna gain is specified at +51 dBi, however, the US regulation allows for a tradeoff of antenna gain and conducted power. This regulation does not restrict the transmit power appropriate for blood monitoring system and can satisfy the power requirements for tag as discussed in section A.3.1. Also, to provide sufficient power for tag, a reader antenna needs to transmit highly directive beam. Thus, the higher gain can be obtained using beamforming capability of array antenna systems.

APPENDIX B

ANSYS HFSS Simulation Setup for FSS Unit Cell Design

Since FSS is a repetitive surface designed to emulate the infinite array, the FSS performance is predominated by the FSS unit cell response. To design an FPC antenna system with an FSS array, an FSS unit cell should be carefully designed for desired performance. An FSS unit cell geometry, dimensions and material are selected based on applications, fabrication and etc, and theory and design about an FSS unit cell have been discussed in [38-39]. This section shows how the ANSYS HFSS simulation is set up for the FSS unit cell design from [61].

B.1. Assign the Master and Slave Boundaries

1. Select one surface of the radiation boundaries as shown in Fig. B.1 and click HFSS>Boundaries>Assign>Master.

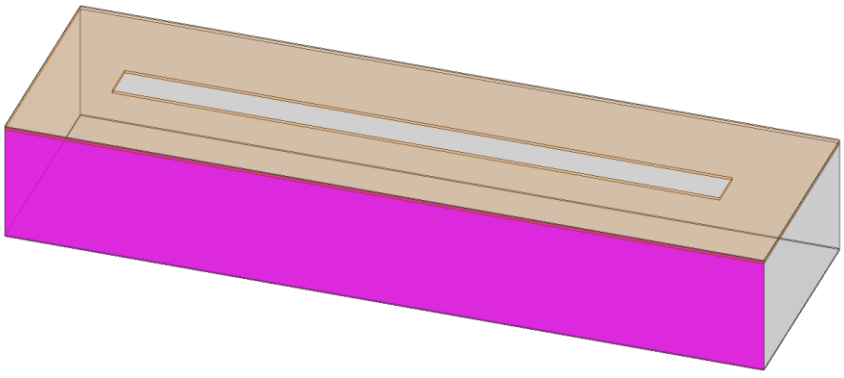

Fig. B.1. Face selection for Master1 boundary

2. Accept the default name as ‘Master1’.

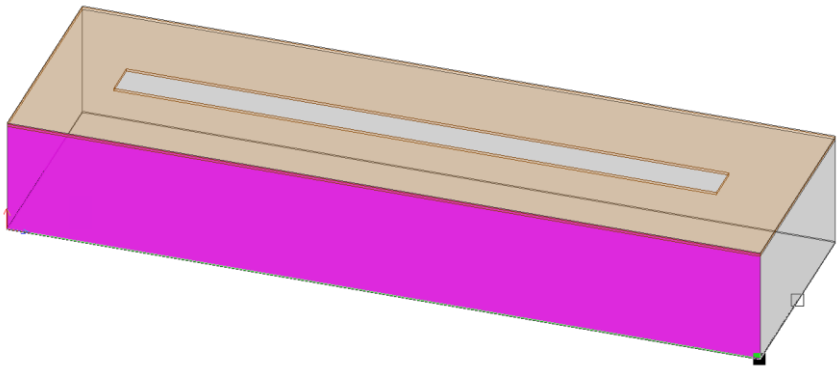

Fig. B.2. Draw ‘U vector’

3. Click the dropdown menu for the ‘U vector’ and select ‘New Vector’.

4. Draw the ‘U vector’ of the coordinate system on the selected face. Click on the lower left corners as the starting point and drag the cursor to the right corner and click as shown in Fig. B.2.

5. Check the ‘Reverse Direction’ of the ‘V vector’. The Master boundary is assigned as shown in Fig. B.3.

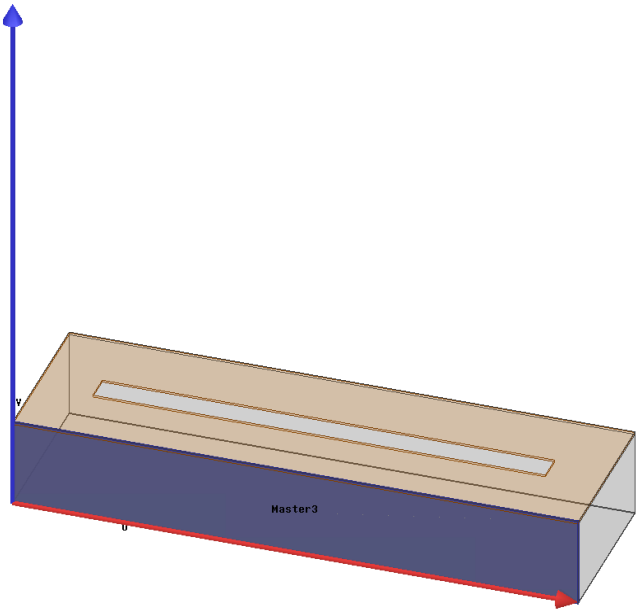

Fig. B.3. Master1 boundary assignment

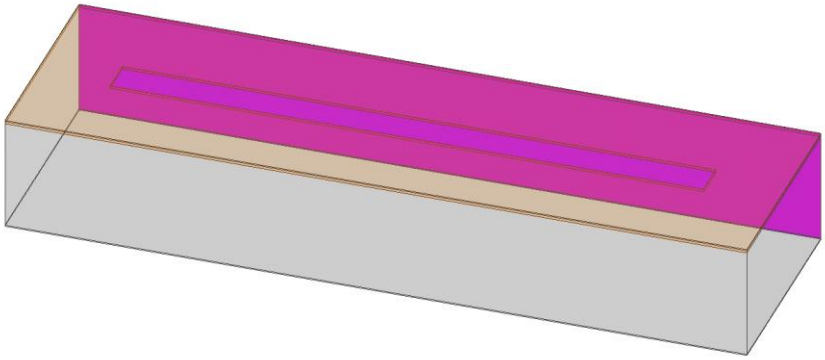

Fig. B.4. Face selection for Slave1 boundary

6. Select the opposite face and click HFSS>Boundaries>Assign>Slave as shown in Fig. B.4.

7. Select ‘Master1’ as the Master Boundary.

8. Draw the ‘U vector’. Click on the lower left corners as the starting point and drag the cursor to the right corner like Master1. Click ‘Next’ and ‘Finish’. The Slave boundary is assigned as shown in Fig. B.5.

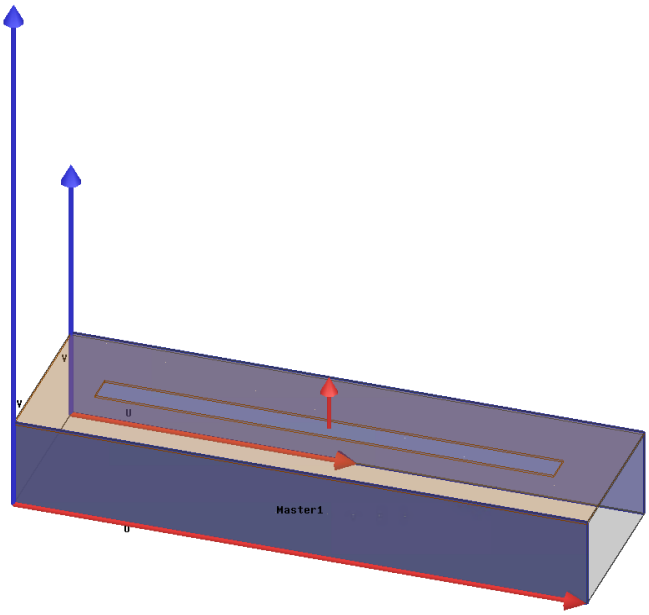

Fig. B.5. Slave1 boundary assignment

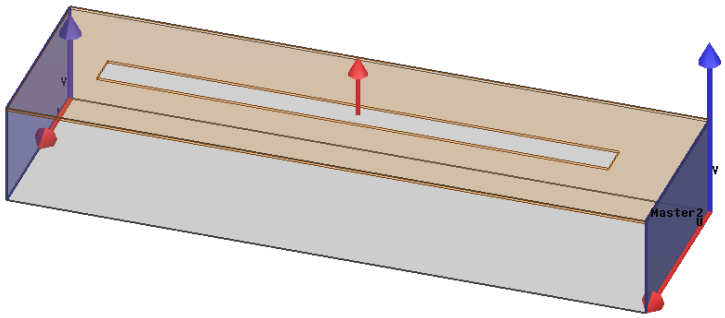

Fig. B.6. Master2 and Slave2 boundaries assignment

9. Repeat the step 1 – 8 for the Master2 and Slave2 boundaries shown in Fig. B.6. Note that 'Reverse Direction' of the 'V Vector' is checked for Slave2 boundary.

B.2. Assign the Perfect E Boundary

1. Select the aperture as shown in Fig. B.7.

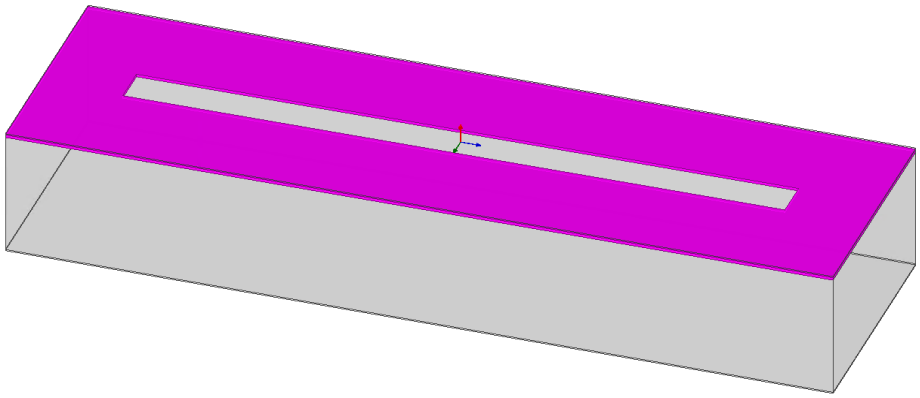

Fig. B.7. Face selection for Perfect E boundary

2. Select HFSS>Boundaries>Assign>Perfect E.

3. Accept the default name and click OK. The Perfect E boundary is assigned as shown in Fig. B.8.

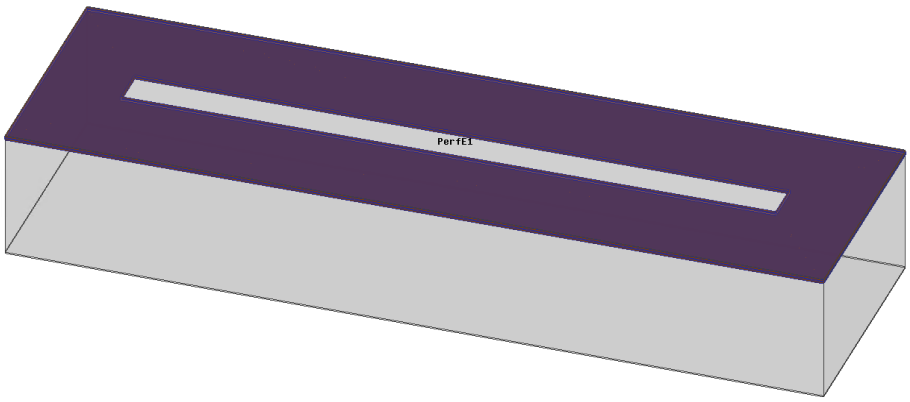

Fig. B.8. Perfect E boundary assignment

B.3. Assign the Floquet Ports

1. Select the top surface of the radiation boundary as shown in Fig. B.9 and click HFSS>Excitations>Assign>Floquet Ports.

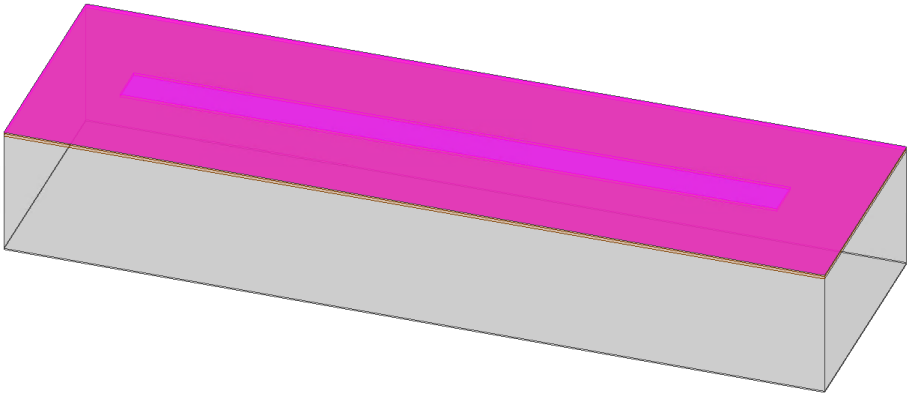

Fig. B.9. Face selection for Floquet Port1

2. For the Lattice Coordinate System, select ‘New Vector’ of the ‘A Direction’. Draw the ‘A vector’ as shown in Fig. B.10. Repeat the same for ‘B Direction’.

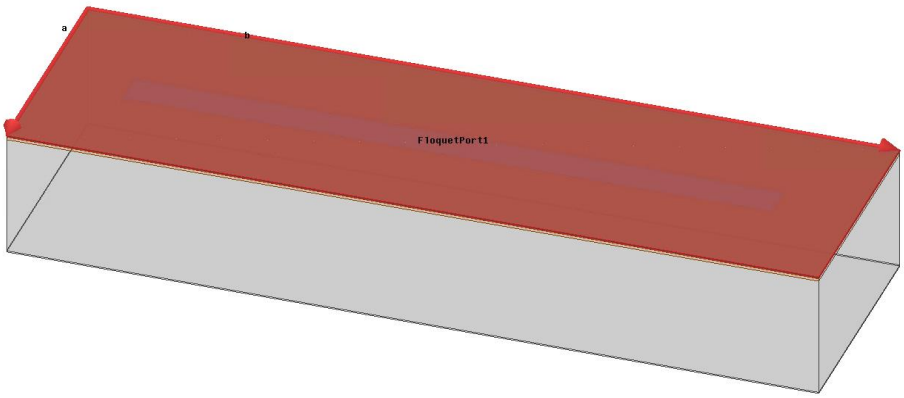

Fig. B.10. Draw the new vector in ‘A Direction’ and ‘B Direction’

3. On the Modes setup tab, enter 10 as the Number of Nodes.

4. Click the Modes Calculator and set up the frequency to 12 GHz, which is the design frequency.

5. Accept the values by clicking OK to close the Calculator as shown in Fig. B.11.

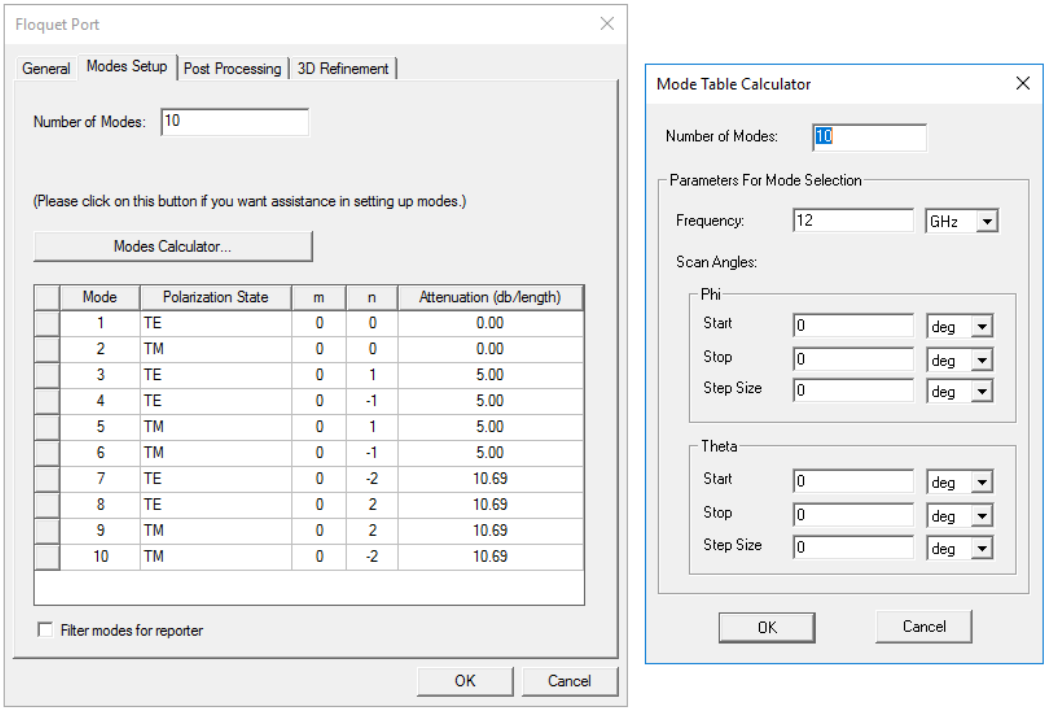

Fig. B.11. Set up the mode and design frequency

Fig. B.12. Set the 'Deembed' Distance

6. On the Post Processing tab, check the 'Deembed' and specify the Distance as 16.05 μm as shown in Fig. B.12. The distance corresponds to the spacing between top surface of radiation boundary and aperture.

7. On the 3D Refinement tab, check the Affects Refinement for Mode 1.

8. Click OK to close the dialog. Select the bottom surface of the radiation boundary and repeat the step 1 – 7 to set up the second Floquet Port.

B.4. Setup the Analysis

1. Right click on Analysis in the project tree and select Add Solution Setup as shown in Fig. B.13

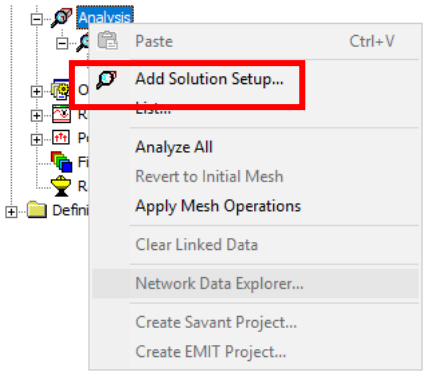

Fig. B.13. Add Solution Setup

2. On the General tab, set the Solution Frequency to 12 GHz. Set the Maximum Number of Passes 40 and the Maximum Delta S to 0.03 as shown in Fig. B.14.

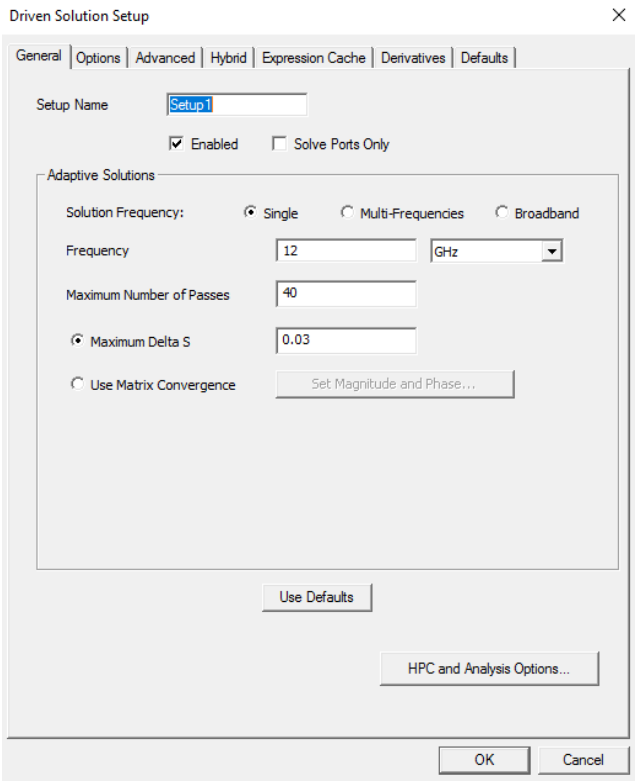

Fig. B.14. Set the Frequency and Maximum Number of Passes

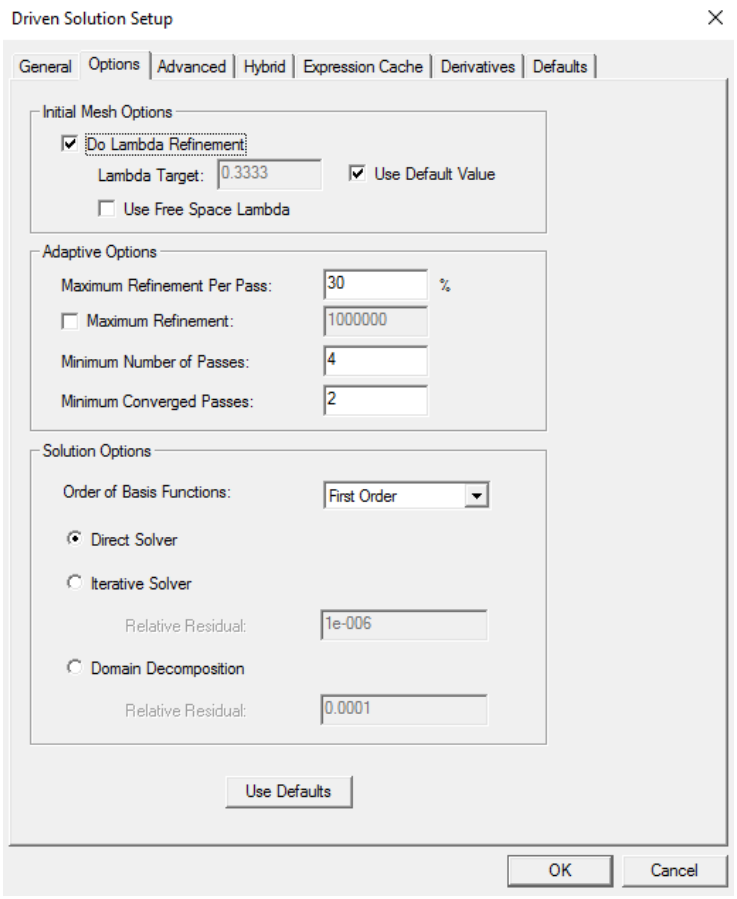

Fig. B.15. Set the Initial Mesh Options and Adaptive Options

3. On the Options tab, check the Do Lambda Refinement and set the Lambda as 0.3333. Set the Maximum Refinement Per Pass to 30%, the Minimum Number of Passes to 4 and the Minimum Converged Passes to 2.

4. Select First Order in Order of Basis Functions and click OK to accept the setup.

B.5. Setup the Sweep

1. Right click on Setup1 in the project tree, select Add Frequency Sweep as shown in Fig. B.16.

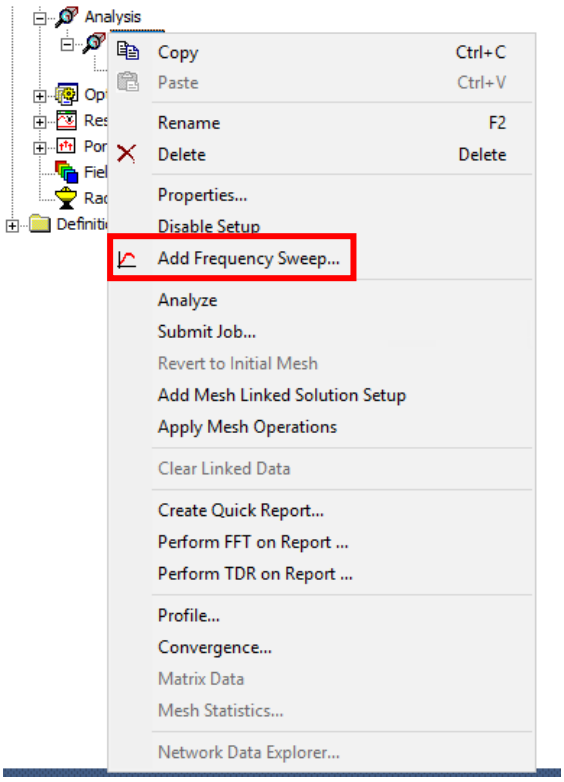

Fig. B.16. Add Frequency Sweep

2. For the Sweep Type, select Interpolating.

3. For the Frequency Sweeps, select Linear Step as Distribution. Then set the Start as 5 GHz, the Stop as 25 GHz and the Step Size as 0.1 GHz.

4. On the Interpolation tab, se the Max Solutions as 50, and Error Tolerance as 0.5%.

5. Click the Advanced Options and set the Minimum Solutions to 5 and the Minimum number of Sub Ranges to 1 as shown in Fig. B.17.

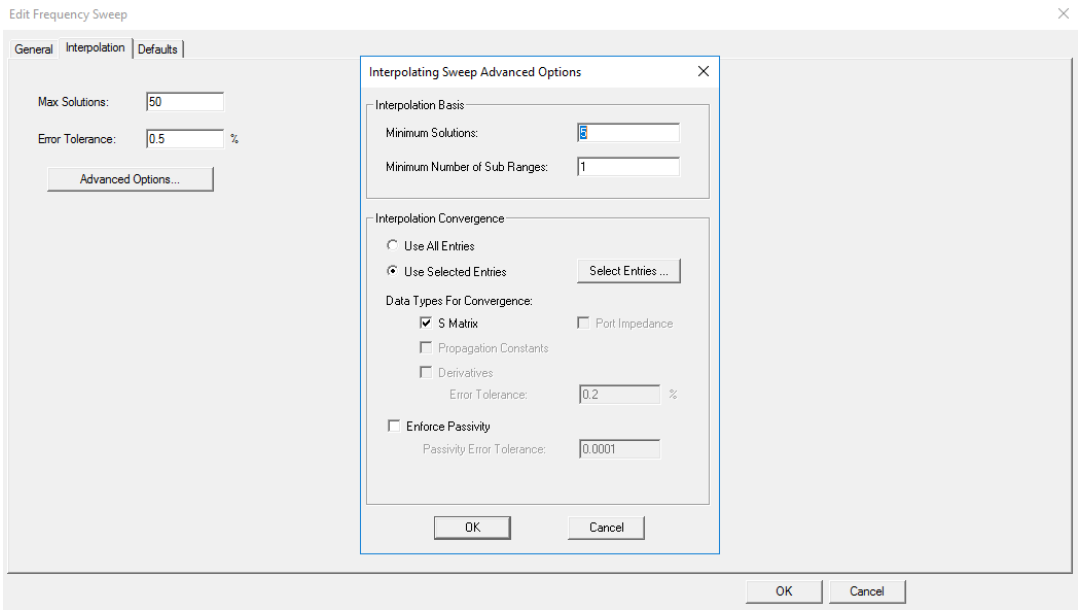

Fig. B.17. Set the Interpolating Sweep Advanced Options

6. For Interpolation Convergence, select the Use Selected Entries.

7. In the Interpolation Basis Convergence dialog, leave the Entry and Mode Selections as All. Then use the vertical scroll bar to find the FloquetPort2:1 row, and set the value in the FloquetPort1:1 column on that row to ON as shown in Fig. B.18

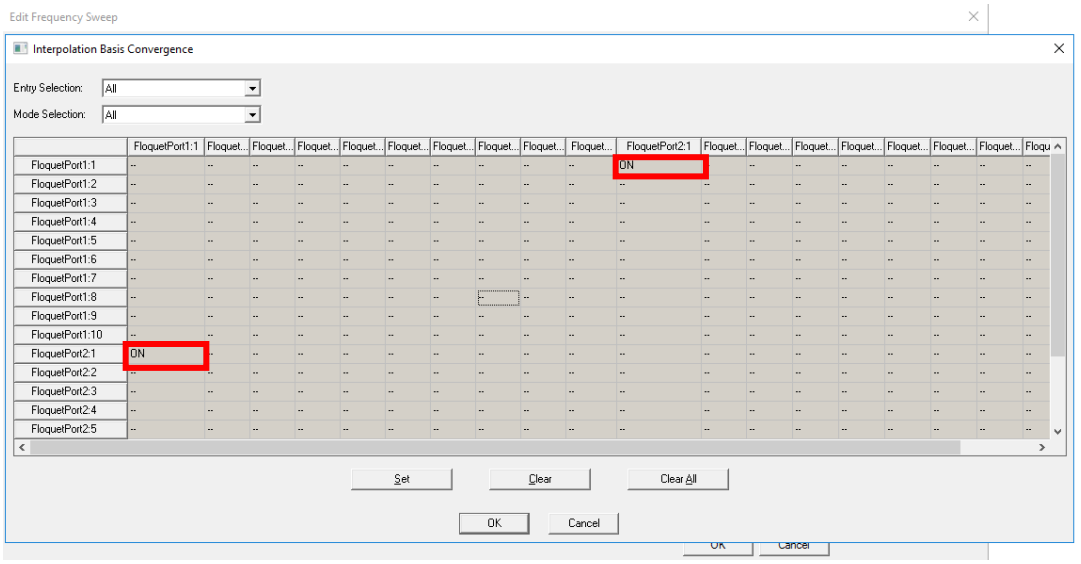

Fig. B.18. Set the Interpolating Basic Convergence

8. Use the horizontal and vertical scroll bars to find the row for FloquetPort1:1 and the column for FloquetPort2:1, and set that cell to ON as shown in Fig. B.18